UIB

Studying lipid interactions of specific myelin proteins using nanoscaled model membrane-mimics and nanoparticles

Author: Oda C. Krokengen
Supervisors: Petri Kursula and Arne Raasakka
Author address: oda.krokengen@student.uib.no

A thesis presented for the degree of Master in Nanoscience

The Department of Biomedicine
University of Bergen
Norway
20.11.2018

Acknowledgements

This thesis was carried out from January to October 2018 at the Department of Biomedicine, University of Bergen, at German Electron Synchrotron (DESY), Hamburg, Germany, and trough collaborators at the SCRD beamline at ASTRID 2. The work was supervised by Professor Petri Kursul, PhD and Arne Raasakka, MSc.

I would like to express my greatest gratitude towards my supervisors Dr. Petri Kursula and Arne Raasakka for helping throughout this project. Thanks to Arne who has guided me through new methods, giving tips and for answering every question I had. I would also like to thank Dr. Erik Hallin for helping me in the lab, Endy Spriet for assisting me with the transmission electron microscope and Professor Chaozhan Wang for providing different types of nanoparticles.

I also thank the Molecular Imaging Center (MIC) and Biophysics, Structural Biology and Screening (BiSS) core facilities at the Department of Biomedicine, University of Bergen, for providing access to various instrumentation. Additionally, the beamline staff at DESY and ASTRID2 are gratefully acknowledged.

Table of contents

List of abbreviations

AuNP	Gold nanoparticle
CMT	Charcot-Marie-Tooth disease
CNS	Central nervous system
DDS	Dejerine-Sottas syndrome
DMPA	1,2-dimyristoyl-*sn*-glycero-3-phosphatidic acid
DMPC	1,2-dimyristoyl-*sn*-glycero-3-phosphocholine
DMPG	1,2-dimyristoyl-*sn*-glycero-3-phosphoglycerol
DPC	Dodecylphosphocholine
DPPC	1,2-dipalmitoyl-*sn*-glycero-3-phosphocholine
DTT	Dithiothreitol
EDTA	Ethylenediaminetetraacetic acid
FABP	Fatty acid binding protein
HEPES	4-(2-hydroxyethyl)-1-piperazineethanesulfonic acid
His$_6$-tag	Hexahistidine tag
IPL	Intraperiod line
IPTG	Isopropyl-β-D-thiogalactopyranosid
LB	Lysogeny Broth
LUV	Large unilamellar vesicles
MaBP	Maltose-binding protein
MBP	Myelin basic protein
MDL	Major dense line
MRI	Magnetic resonance imaging
MS	Multiple sclerosis
Ni-NTA	Nickel nitrilotriacetic acid
NPs	Nanoparticles
OD	Optical density
ODS	Octadecyltrichlorosilane
P0	Myelin protein 0
P0ct	Cytoplasmic tail of P0
P2	Myelin protein 2
PLP	Proteolipid protein
PMP22	Peripheral myelin protein 22
PMSF	Phenylmethylsulphonyl fluoride
PNS	Peripheral nervous system
SDS-PAGE	sodium dodecyl sulphate polyacrylamide gel electrophoresis
SEM	Scanning electron microscopy

TEM	Transmission electron microscopy
TEV	Tobacco Etch virus
UV-Vis	Ultraviolet–visible spectroscopy
SAXD	Small-angle X-ray diffraction
SEC	Size exclusion chromatography
SRCD	Synchrotron radiation circular dichroism spectroscopy
SLI	Schmidt-Lantermann incisure
SUV	Small unilamellar vesicles

List of Figures

List of Tables

1 Abstract

The nervous system is a complex and highly specialized network, where rapid conduction of nerve impulses over large distances is required for correct functioning of vertebrate nervous system. Saltatory conduction of electrical signals from one neuron to another is enabled by the myelin sheath, which is a multi-layered proteolipid membrane with unique myelin proteins. Myelin in rich in lipids and proteins that are not common in normal cell membranes, and the proteins specific to the myelin structure is quite unique and differ between the CNS and PNS. Abnormalities in myelin-specific proteins are involved in neurological diseases, leading to demyelination and chronic disability, such as multiple sclerosis (MS) and Charcot-Marie-Tooth disease (CMT). Nanotechnology can be used to investigate protein-membrane interactions, introducing nano-sized model membranes that mimic the native lipid bilayers found in myelin, and also in approaching new treatments for neurological diseases. In this study, the interactions between three specific myelin proteins and lipid membranes were studied with the used of two model membranes; liposomes and bicelles, and at the same time comparing the model systems to see if one could be preferred over the other in future research. The myelin proteins myelin basic protein (MBP) and peripheral myelin protein 2 (P2) and cytoplasmic tail of myelin protein 0 (P0) were expressed and purified and used in this thesis together with a mutant form of the P2 protein. Turbidimetry and small-angle X-ray diffraction (SAXD) were used to investigate proteolipid aggregate stability and structural effects induced by the myelin proteins. Lipid ratio dependencies were examined with co-sedimentation assay while synchrotron radiation circular dichroism (SCRD) measurements of P2wt with the different model membranes were conducted to explore the structural changes of P2 induced by binding to lipids. Transmission electron microscopy (TEM) was used to visually look at how the different protein induced lipid aggregated. Finally, a pilot study with nanoparticles were conducted to gain knowledge about how they can be functionalized and used in studying protein-membrane interactions, and how they in the future can be used in applications targeting the nervous system. Co-sedimentation assays were carried out to analyze protein binding, while ultraviolet-visible spectrophotometry (UV-vis spectrophotometry) assessed together with TEM to get any confirmation of the lipid coating of the gold nanoparticles.

In this thesis, several interactions properties of the three myelin proteins MBP, P2 and P0 were found to differ between the model membranes, and highly ordered structures of bicelle aggregates induced by P2wt and P2 F57A were investigated. Examination of lipid coated gold nanoparticles revealed partial coating and that optimization of the protocols are highly needed.

2 Introduction

Correct functioning of the nervous system is required to cope in everyday life. Malfunction of this system can occur because of genetic defects, physical damage or simply by aging. The most common problem is failure of nerve conduction where one cause is neurological disorders like multiple sclerosis (MS) and Charcot-Marie-Tooth disease (CMT). Both disorders do not affect the nerve cell directly, but damage the insulating layer around them resulting in reduced or blocked signalling. MS is the most common autoimmune disorder of the central nervous (CNS) system with global prevalence of 30 per 100 000, while CMT is one of the most common inherited human neuropathies in the peripheral nervous system (PNS), affecting 40 per 100 000 (1-3). Epidemiology studies of MS show higher prevalence of MS in North America and Europe in difference to low levels in Eastern Asia and Africa, with more prevalence in Caucasians from Scandinavia and Scotland (4-6). The disease mechanisms it not fully understood and deeper knowledge about disease mechanisms is required to fully understand neurological diseases mentioned above. Basic understanding of these principles can in the future be used to develop a potential medicine to improve function of affected people.

2.1 Nervous system in general

The nervous system is made up of all nerve cells, called neurons, in our body and it is because of this system that we can communicate with the outside world and at the same time control many mechanisms in our body. When we sense a specific smell, touch or sound, the nervous system will process this information and trigger reactions like pain or muscle contractions. Each neuron has a cell body which receives signals from dendrites, which are branched projections of the neuron that propagate electrochemical stimulation. Signals are then passed on via the axon, the main conducting unit of the neuron, and through transmitters (7). A network of these cells makes up our nervous system, which can be divided into two main parts. The first part is the CNS and it includes the nerves in the brain and the spinal cord. It integrates all information received from the different parts of the body and then gives feedback to influence further activity. The second is the peripheral nervous system (PNS), which includes all other neurons in the body, and serves as a bridge between the CNS and the rest of the body like organs and limbs (8).

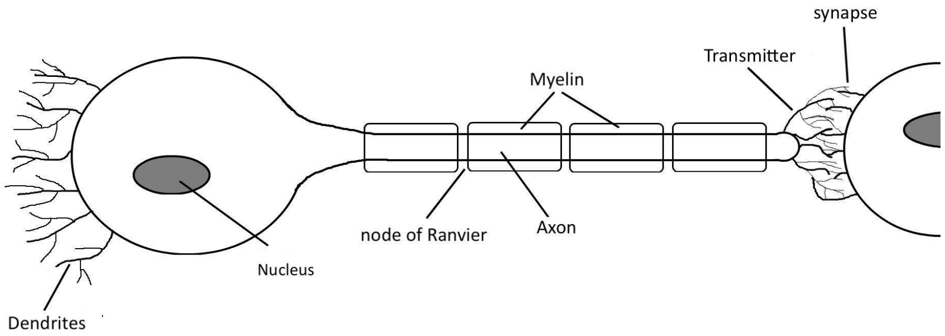

Figure 1: Nerve cell. The cell body (soma) receives signals from the dendrites and passes it along the axons and through the neurotransmitters. The myelin sheath works as an electric insulator and the axonal potential jumps from one node of Ranvier to the next, increasing the speed of the nerve impulse. Schwann cells are responsible for myelination in the PNS, whereas oligodendrocytes do it in the CNS.

The nervous system comprises of two main types of cells; neurons and glial cells. Neurons, as seen in Figure 1, transmit signals via the axon and communicate with other cell through synapses. The synapses convey the transmission of the electrical signal between one nerve cell to another nerve cell, muscle cell or a gland cell. Hundreds of different types of neurons exist in the human body, like sensory neurons and motor neurons, but they all have in common to give and receive information from the distant parts of the body. Glial cell are not neuronal cells and do not function in the signal transduction between cells. Instead, they keep the conditions surrounding the nerve cells at an optimal level. They maintain homeostasis, supply nutrients and oxygen, hold neurons in place, remove dead neurons and insulate axons (9).

2.2 Myelin sheath and its insulating properties

Rapid conduction of nerve impulses over large distances is required for correct functioning of the nervous system. This is enabled by a tightly packed multi-layered proteolipid membrane wrapped around selected axons, named the myelin sheath, and works as an electrical insulator (Figure 2). Myelination, also called myelinogenesis, is the production of the myelin sheath. Myelination in the CNS starts under the development by oligodendrocyte precursor cells that are generated from glial precursor cells, which can differentiate into astrocytes, neurons and oligodendrocytes (10). Myelin stems from and are a part of the Schwann cells in the PNS and the oligodendrocytes in the CNS (11). Myelination of axons differs between the CNS and PNS glial cells. Since the brain and spinal cord are encased in the skull and vertebrae, thus having limited space, oligodendrocytes can myelinate several axon segments at once, up to 50 segments, thereby reducing the number of glial cells needed (12). In the PNS, neurons have to pass organs, muscles and joints, and are therefore more exposed to trauma and damage. Thus, the PNS favours durability over space which causes one Schwann cell to myelinate a single axonal segment (13). Small axons (≤1 μm) will remain unmyelinated, but larger axons (≥1 μm) are enclosed with one cell per axon per internode (7). When myelination occurs, Schwann cells will organize into distinct membrane domains with a unique group of proteins and cytoplasmic compartments. The innermost membrane mediate interactions with the axonal ligands through adhesion molecules and receptors (14).

Axons can be either unmyelinated or myelinated, where small axons in vertebrates are often unmyelinated while large axons are insulated by myelin, like the sensory axons of the PNS. When unmyelinated axons are transmitting a signal, the generation of action potential is distributed along the entire axon because the ion channels (Na^+ and K^+), taking part in the generation, are distributed through the whole axon, involving the entire membrane (13). Local circuits of ion flow depolarize the adjacent piece of membrane in a continuous, sequential fashion. In myelinated axons, however, the ion channels are concentrated in periodic gaps between the myelinated regions of the axon, called nodes of Ranvier, and myelin is critical for their function. The excitable membrane surrounding the axon is exposed to the extracellular space only at these nodes where the sodium (Na^+) channels are localized. This means that the local circuits, which in unmyelinated axon depolarize the whole membrane, cannot flow through the myelin sheath and can only, depolarize the axon at the next node. The insulating function of the myelin sheath means that little energy is required to depolarize the membrane between the nodes which results in an increased speed and jumping of the action potential from node to node, called saltatory conduction (7, 15). Unmyelinated axons have conduction velocities from 0.5 to 10 m/s, while myelinated ones can have conduction velocities up to 150 m/s (9). The acceleration of nerve conduction is 20-100 fold in myelinated axons compared to unmyelinated ones. Myelin protects neurons and play a key role in signal transduction (16).

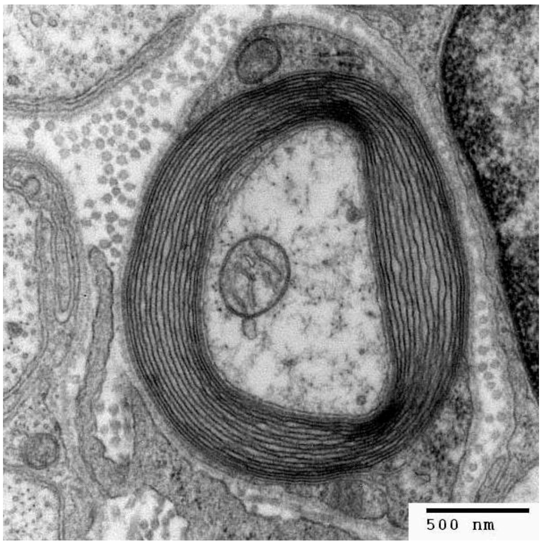

Figure 2: Transmission electron micrograph of myelinated axons. The multi-layered membrane encircles the axon of a neuron and gives an insulating effect. Reprinted from CC-BY-SA-3.0 (http://creativecommons.org/licenses/by-sa/3.0/), from Wikimedia Commons

The end result of myelination is two substructures called compact myelin and non-compact myelin. Compact myelin consists of tightly packed membrane sheets without much cytoplasm. No molecular entrance is possible keeping the insulative nature of the myelin sheath. In the CNS this tight compaction requires expression of structural proteins, such as proteolipid protein (PLP) and myelin basic protein (MBP) (17). The myelin sheath is periodically structured in compact myelin, with alternating electron-dense and electron-light layers, called the major dense line (MDL) and the intraperiod line (IPL) respectively. MDL, which is rich in electrons, is the condensed cytoplasmic face of the membrane (cytoplasmic compartment), while the IPL is the apposed extracellular surfaces of the corresponding multilayers (extracellular compartment). The tight compactions of these membranes results in cycle with length of 12 nm (18).

Non-compact myelin contains cytosol and consists of several compartments. On each end of a myelin sheath segment are so-called paranodal loops which are membrane loops containing cytoplasm and are adjacent to the nodes of Ranvier (19). Other segments are longitudal incisures in the CNS and Schmidt-Lantermann incisures (SLIs) in the PNS. These regions cross the compacted myelin like tunnels that contains cytoplasm, and connect the peripheral cytoplasm to the periaxonal cytoplasma, referred to as abaxonal and adaxonal cytoplasm. It is theorized that these regions are important for transport of metabolic substances that is required for myelination and for maintaining the myelin sheath (17, 20).

Paranodal junctions are a part of the myelin ultrastructure. They are localized adjacent to the nodes of Ranvier and form a special axon-glia contact zone, which links the paranodal loops in the non-compacted myelin to the axonal plasma membrane, called axolemma. Juxtaparanode is the adaxonal layer that comes right after the paranodal junctions, immediately followed by the internode which is the inner membrane of myelin and is separated from the axolemma by the periaxonal space. The inner leaflet of the myelin is in contact with the adaxonal layer while the outer leaflet is in contact with the abaxonal layer. These are collectively referred to as mesaxons marking the point of edge-to-edge contact (17, 21)

How does the myelin sheath organize itself into a highly stable structure? Myelin is composed of amphipathic lipids, with apparent hydrophobic heads, and highly hydrophobic proteins, where both exert repulsive forces towards the aqueous solution in between the myelin bilayers. There are also intramolecular attractive forces among the lipid molecules like hydrogen bonds formed close to the lipid-water interface and van der Waals dispersion forces between methylene groups on adjacent lipids (18). Electrostatic forces operating between the negatively charge lipid surfaces and the basic residues in myelin MBP and P0 cytoplasmic tail in MDL contribute to the tight packing of the myelin bilayers (22).

2.2.1 The main difference between the CNS and PNS lies in the protein composition

Myelin consist of dozens of layers of lipid bilayers that contain high concentrations of specific integral and peripheral membrane proteins that function in stacking of the membrane bilayers, forming so called multilayers. The compacted myelin sheath consists of specialized components of lipids and proteins that are not found in normal cell membranes, while the lipid composition in both CNS and PNS is quite similar; the protein content is quite different.

There are no lipids that are completely specific to myelin, but cerebroside (galactosylceramide) is the most typical. Other major lipids in myelin are cholesterol, ethanolamine-containing plasmalogens, phosphatidylcholine (PC) and glycosphingolipids (23, 24). 65% of the total lipid dry weight is comprised of cerebroside, cholesterol and ethanolamine plasmalogens. Both cholesterol and cerebroside provide stability to the myelin sheath, where cholesterol regulates fluidity and permeability of the membrane while cerebroside, with its long chain fatty acid parts, stabilizes with multiple interactions. Ethanolamine plasmalogens have been studied for increasing packing density and are shown to provide mediators for inflammatory reactions (25, 26). Membrane asymmetry is a distinct feature of the myelin sheath, which means that the lipid composition of the cytoplasmic leaflet is different to the extracellular sheet, thought to contribute to achieve the ordered structure. The cytoplasmic leaflet is concentrated with charged phospholipids whereas the extracellular leaflet has a lot of glycosylated lipids (27). One example of this is that cholesterol is on the extracellular surface together with cerebroside, while ethanolamine plasmalogens is on the cytoplasmic side of the lipid bilayer (18). Lipid bilayers have different phases depending on temperature and structural properties, such as length of the hydrocarbon tails, if the tails are saturated or unsaturated, tail conformation and the composition of the headgroup. There is a phase transition temperature where a lipid goes from a gel phase to disordered fluid phase, with some lipids having a rippled phase in between these. In the gel phase the lipid tails are highly ordered and are so to speak locked in place. Over a certain temperature the bilayer undergoes a transition to a fluid phase where the tails become more disordered (28). A study on native CNS myelin revealed that the bilayers show a structure typical of the fluid phase with coexistence of lipids in both gel and fluid phase, called mesophase coexistence (29). Cholesterol and galactosphingolipids decrease the fluidity and permeability of the membrane, whereas plasmalogens increase the fluidity by lowering the transition temperature from gel to fluid phase (30). Even though the lipid composition is similar, the greatest difference between CNS and PNS myelin composition lies in the protein components.

In CNS myelin, proteolipid protein (PLP) and myelin basic protein (MBP) make up 60-80% of the total protein mass, with other proteins and glycoproteins being present to lesser extents. PLPs contain several membrane-spanning domains which are conserved during evolution. MBP is located on the cytoplasmic face of the myelin membranes and PLP and MBP have major roles in myelin formation and stabilization, by which MBP interacts with the lipids in the myelin membrane (31). MBP is found in the MDL, whilst PLP is in the IPL which is less electron dense (32). Other well-known proteins in the CNS are 2',3'-cyclic nucleotide 3'-phosphodiesterase (CNP), myelin-associated glycoprotein (MAG), myelin/oligodendrocyte glycoprotein (MOG) and myelin/oligodendrocyte-specific protein (MOSP). CNP is in short localized in the cytoplasm of non-compacted myelin in the CNS and harbours a C-terminal isoprenylation motif that allows it to interact with the lipid bilayer, while MAG, a protein with a large (72 kDa) and a small (67 kDa) isoform, is present during myelination (L-MAG) and in mature myelin (S-MAG) (33). MAG is expressed on the outermost surface of the myelin sheath, is a member for the immunoglobulin superfamily and is an important marker for maturation of oligodendrocytes, while the 48-kDa MOSP protein is associated with cytoplasmic cytoskeleton and plays an important role in interaction between membrane and cytoskeleton during CNS myelination (34, 35).

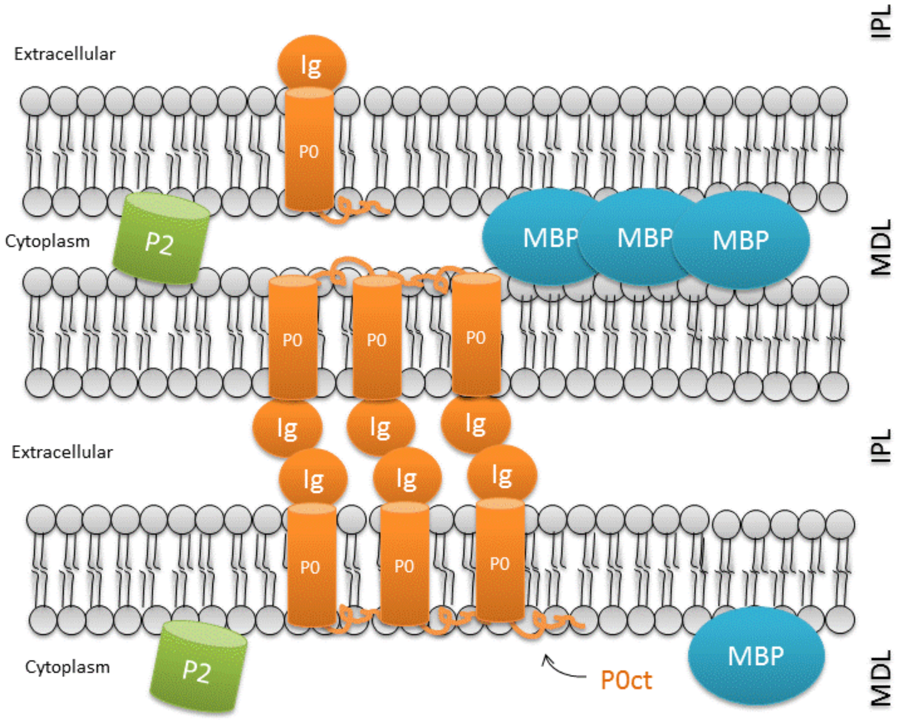

Figure 3: Illustration of CNS and PNS myelin sheath. Myelin basic protein (MBP) is found in the major dense line and drives compaction by binding to lipids in the myelin membrane. Peripheral myelin protein 2 (P2) have patches of positive charge on its surface and hydrophobic residues that are involved in membrane binding and interactions, and also resides in the MDL. Myelin protein P0 (P0) is a transmembrane protein with the immunoglobulin-like domain in the intraperiod line and the cytoplasmic tail in the MDL.

P0 is the major protein in PNS myelin and accounts for more than half of the PNS myelin protein. This protein in necessary for normal myelination and mediates adhesion between adjacent lipid bilayers and drives myelin compaction (see Figure 3) (36). In addition to P0, PNS myelin contains a glycoprotein called peripheral myelin protein 22 (PMP22), which is frequently mutated in inherited neuropathies (37), and the peripheral myelin protein 2 (P2) which is expressed by the Schwann cells and both are involved in stabilizing the assembly of the multilayered lipid membrane and lipid transport (33, 38). Connexin 32 (Cx32) is present in both PNS and CNS, contains four transmembrane domains those of PMP22 and has a molecular mass of 32 kDa (33).

The proteins mentioned above together with hundreds more are found to be present in CNS and PNS myelin (39). This thesis will focus on MBP, P0 and P2 since this project focus on their interaction with lipids and nanoparticles

Myelin Basic Protein

MBP is found to be one of the essential factors in myelin membrane stacking in the CNS and the formation of major period line, which is disturbed in demyelinating conditions such as MS and demyelinating neuropathies (40). MBP is the second most abundant protein in the CNS after PLP, where 30% of total protein is MBP, while only 5%-18% of the total protein in the PNS is MBP. It has been called the "executive molecule of myelin" since it is the only protein so far that is shown to be essential for myelination in the CNS (33). Due to proteins like P0, P2 and PMP22 in the PNS, presence of MBP is not vital for myelin compaction, but has been found to have an effect on the number of SLIs and the regulation of MAG and Cx32 proteins. Decreased expression of MBP in the PNS caused an upregulation of these proteins in the affected mouse (41). The high positive net charge of MBP allows it to interact with the phospholipid-rich cytoplasmic face of myelin membranes. This interaction results in a charge neutralization, folding and partial membrane insertion (22, 40). MBP is known for its autoantigenic properties (capable of inducing an immune response) in MS, and this feature may arise from the susceptibility of MBP to break down depending on lipid composition (22, 29). The structure and function of MBP is altered as well, promoting decreased compact myelin stability (42). A large gene complex, called Genes of Oligodendrocyte Lineage (Golli), have 10 exons in humans and 7 of these give rise to the classical MBP found in myelin. This large gene complex does not only express MBP found in myelin but also several other Golli proteins and Golli-MBP, which are found in neurons, oligodendrocytes and T-cells (43, 44). Several different isoforms of the classical MBP are formed, and the 18.5 kDa isoform is the most abundant in myelin. This isoform occurs, through post-transitional modifications, in several different charged forms, called C1, C2, C3, C4, C5, C6 and C8, with decreasing net positive charge reducing its interaction with lipid membranes. Post-transitional modifications like phosphorylation, deamination and methylation are responsible for producing these isoforms, with the C1 isoform being the least modified one and with highest positive charge (45). Almost every isoform of the 18.5 kDa MBP is phosphorylated at Arg9 and Arg54 which have been suggested to inhibit nuclear targeting and play a role in myelin structure and function under increased neuronal activity (46). Not only does MBP bind to negatively charged lipids, it also binds to actin filaments, Ca^{2+}-Calmodulin, clathrin and tropomyosin (47-49). MBP has not yet been crystallized in its lipid-bound state, but circular dichroism has shown that it gains a secondary structure content upon binding to negatively charged lipids showing an increased amount of α-helical structure (40). It has been suggested that MBP forms an ordered, self-assembled protein meshwork that stabilizes compact myelin, while other factors, such as P2 may be involved in the process (40, 50).

Peripheral myelin protein P2

In the PNS, peripheral myelin protein P2 is one of the most abundant proteins, making up to 15% of the total protein content, but it is also found in the CNS being in both spinal cord and brain stem (51, 52). In the major dense line, P2 is thought to stabilize the assembly of the multilayered lipid membrane thus stabilizing membrane stacking. It is a small protein consisting of 131 amino acids resulting the size of 15 kDa with a β-barrel structure covered by an α-helical lid as seen in Figure 4 A (52, 53). P2 belongs to a conserved family of fatty acid binding proteins (FABPs) and can transfer fatty acids from and to lipid membranes using a collision transfer mechanism, which indicates a functional role to maintain a stable environment for the lipids in myelin (54). The ligand binding pocket is inside the β-barrel, containing two arginine residues Arg106 and Arg126 that are essential in interacting with negatively charged lipid groups (55, 56). Studies have found a cholesterol recognition amino acid consensus sequence (CRAC) binding motif at its C-terminus which indicate that P2 might bind cholesterol – a fundamental lipid component in the myelin sheath (52).On the P2 surface there are patches of positive charge that are thought to be involved in binding and stacking of membranes. It also has hydrophobic residues in the helical lid that could help the binding with insertion deeper into the membrane. Studies further revealed that the main site for membrane-binding is the helical lid which could lead to lipid transfer in the cavity like a transfer mechanism seen with FABPs, while on the other side of the protein the binding is mostly based on electrostatic interactions (53). P2 has been detected with increased expression in thicker myelin sheaths compared to thinner sheaths, and is downregulated, but present after development (54). Three point mutations in the pmp2 gene have been linked to the neuropathy autosomal dominant Charcot-Marie-Tooth type 1 and a study of mutant P2 proteins have shown that their stability is remarkably reduced (38, 57). There is also a possibility that the P2 is one of the autoantigens in the Guillain-Barré syndrome together with P0 (58, 59).

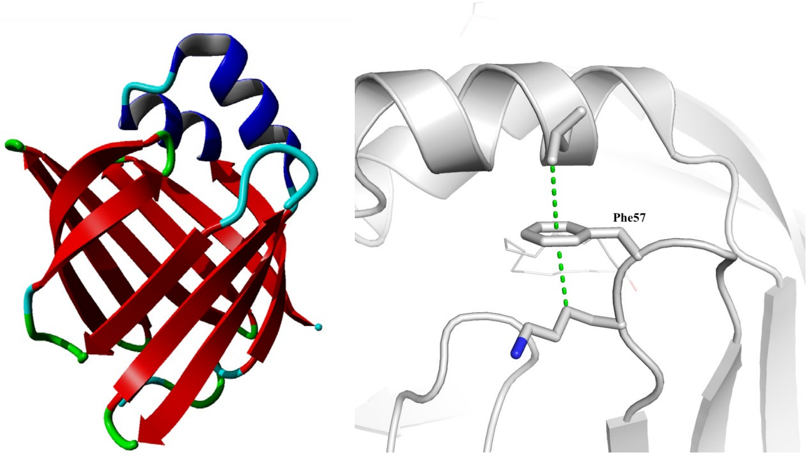

Figure 4: A) Crystal structure of peripheral myelin protein P2 and B) position of Phe57 in the structure. A) The 15 kDa protein contains 10 antiparallel β-strands where the first two strands are linked together by two α-helices forming an α-helical lid. B) Phe57 lies at the tip of the β3-β4 loop and forms a weak π-interaction between C-H groups in neighboring Lys58 and Leu32 residues. Adapted with permission from (60).

Phe57 is a conserved residue in the FABP family, which in human myelin protein P2 is located at the mouth of the ligand-binding cavity, having a role in opening the helical lid for ligand binding (Figure 4 B) (61). Phe57 lies at the tip of the β3-β4 loop forming a weak π-interaction between the C-H groups of Leu32 and Lys58. Previous study of the Phe57 mutation to alanine (F57A) has revealed that stability and membrane binding of P2 are affected by this point mutation (60). These effects are similar to the point mutation linkeds to CMT (38).

Myelin protein zero

The major protein in the peripheral nervous system is the P0 (also called MPZ), signifying 50% of total protein content, and is primarily expressed in Schwann cells (62). It is a 30-kDa transmembrane protein with its immunoglobulin (Ig)-like domain in the extracelluar IPL and its short cytoplasmic tail (P0ct) in the cytoplasmic MDL (56). Several point mutations in P0 have been found in neurological diseases like Charcot-Marie-Tooth disease type 1 B, Dejerine-Sottas syndrome (DDS), hereditary neuropathy with liability to pressure palsies (HNPP) and congential hypomyelination (CH) (63). P0 is a member of the immunoglobulin superfamily (IgSF), which is known for their ability to recognize specific molecules and stick to them. All proteins that consist of at least one Ig domain are in this family and the Ig domain is highly conserved through evolution (64). The structure of the domain complies with a broad range of amino acid sequences without changing the structure, making it perfect for ligand binding with high specificity, with the Ig domain of P0 having shown to be involved in homophilic adhesion stabilized by a intramolecular Cys^{21}-Cys^{98} disulfide bond (65, 66). The Ig domain most likely forms apposing dimers in the IPL, where one monomer links another monomer on the second membrane together and therefore has the ability to hold together adjacent membrane layers in the PNS (67). It is also shown that the 5 last residues on the C-terminus end of the Ig-domain is disordered which is thought to provide a flexible link to the membrane (68). The cytoplasmic domain of P0 (P0ct) consists of 69 amino residues and have the molecular mass of 7.9 kDa, where cytoplasmic tail has a basic charge and aggregates negatively charged lipids. Point mutations in P0ct are linked to CMT and it is shown that P0 must have an intact cytoplasmic tail to behave as an adhesive molecule (69, 70). P0ct folds only when it interacts with negatively charged lipids and gains a helical secondary structure with lipid interaction, and the association is mainly electrostatic, similarly to MBP (69).

Proteins outlined here and many others take part in the myelination of the axons in both CNS and PNS. They are under intense study to understand the etiology of myelinogenesis and the causes for neurological damage or diseases caused by abnormal myelin sheath. The next part explains briefly how the three proteins elucidated above are connected to MS and CMT.

2.2.2 Demyelinating diseases

Demyelination is the loss of the myelin sheath, and happens if the myelin gets worn or damaged. It disrupts the conduction of electric impulses in the nerves, and is often secondary to an infectious, ischemic, metabolic, toxic or hereditary disorder. Remyelination with regeneration, repair and complete recovery of neural function can occur, but extensive demyelination often leads to axonal degeneration and potentially nerve death (71).

Dysfunction in a part of the brain or the nervous system, structural, biochemical or other abnormalities, can result in a neurological disorder. Specific causes for neurological problems vary, but one subcategory is demyelinating diseases where the myelin sheath around the neurons is damaged and several myelin-specific proteins are involved. Breakdown of the protein-lipid interaction at the membrane surface is often involved in the disease mechanisms, leading to myelin degradation and chronic disability. Demyelinating diseases include both autoimmune and inherited diseases, such as MS and CMT (72).

Multiple sclerosis was first documented early in the 19th century by Robert Carswell and Jean Cruveilhier and is being studied until this day (73). MS is caused by autoimmune attacks on the myelin in the CNS, as well as the nerve fibers themselves, but the etiology of the disease is still not completely known. MS is not hereditary, but there is an increased risk for developing the disease if there is a first-degree relative (parent or sibling) with MS in the family (74). In 1994, four subtypes of MS were defined: relapsing-remitting, secondary-progressive, primary-progressive and progressive relapsing, and 85% of the diagnosed people have relapsing-remitting MS (75). MS is characterized by an active destruction of myelin, persistent demyelination of axons and axonal degeneration. Demyelinating activity is found in specific areas, called plaques, where macrophages, type of white blood cell of the immune system that digest cellular debris, have digested myelin degradation products. Degradation products of myelin proteins like CNP , MAG and MOG were found together with debris from PLP and MBP (76). This is an interesting finding because macrophages is normally separated from the CNS by the blood-brain barrier and should not be present in the CNS. The disease might cause a breakdown of the barrier which allows inflammatory cells to enter the CNS (77). Microglias, which have similar functions like macrophages, are already present in the CNS, and place a role in tissue repairs, clearing debris and infection control. Both macrophages and microglia have been found to contribute to the disease progression of MS (78)

The C8 charge isoform of the 18.5 kDa MBP isoform (MBP-C8) is the least cationic, and is shown to occur in increased amounts in MS patients (79). In this isomer, six arginines are replaced by citrullines in a process called deamidation. This results in a loss of six positive charges resulting in an alteration of the interaction of the proteins with lipids in the myelin membrane. Compared to the C1 isoform, which is least modified and has the highest positive charge, the C8 is shown to not stack bilayers as efficiently as C1 (80). MBP-specific T-cells, important cells in the immune system, are found in MS patients, but also in healthy controls. The findings of T-cells together with the elevated levels of C8 have made MBP the top target in multiple sclerosis research. It is shown that less compacted myelin had increased levels of MBP-C8 and lacked more or less the important C1 isoform, and it can be postulated that this leads to instability and promotes degradation through the immune system (81)

CMT is one of the most common neuropathies of the PNS and both motor and sensory nerve conduction is affected (38). Involvement of the myelin proteins P2 and P0, have been found in different types of CMT together with PMP22, Cx32 and periaxin (82). There are several types of CMT, but the most common form is CMT1, which influences both Schwann cells and myelin. Motor and sensory nerve conduction velocities are remarkably reduced, resulting in muscle weakness and atrophy in the feet. CMT1 is often caused by duplication of or a point mutation in the pmp22 gene and 70-80% of all CMT1 cases are associated with pmp22 mutations, and other CMT-associated genes have been described such as pmp2. Three point mutations in P2 are associated with CMT1 and have been shown to increase aggregation and reduce stability (38). Studies of mice lacking the PMP2 gene had a mild reduction in the motor nerve conduction velocity, but no differences in myelin thickness (83). One study of the mutation found in CMT patient (I43N) did reveal reduced length on the myelin sheath segments which corresponded to reduced conduction velocity (57). The length of myelin segments on the axons in the PNS is crucial for rapid conduction of nerve impulses. When the lengths are shortened the velocity will decrease. The aggregation of P2 and the shortening of myelin segments might be characteristic for CMT1 in patients with P2 mutations.

As mentioned above, mutations in P0 cause neuropathies like CMT, DSS and CH, and several mutation of P0 have been found across Europe (84). The cytoplasmic tail of P0 has been found to be important for the protein to function correctly (70). Mutation in the P0ct domain related to CH showed hypomyelination (low amount of myelination) in affected mice and readily misdirected protein to other plasma membranes than myelin (62). Others have found that a mutation that alters the charge of the intracellular domain can interfere with the formation and compaction of the major dense line and that cysteine substitution that causes DSS might cause aggregates resulting in abnormal P0 complexes (85). Analysis of clinical data from 64 patients with CMT1B neuropathy revealed that if the extracellular domain mutation either involved a charged amino acid or a cysteine substitution, it causes severe neuropathy, where early onset is caused by disruption of the tertiary structure of P0, while late onset is probably due to disruption in the interaction between Schwann cells and axons (86). Schwann cells in mice with an insertion of an inactivated P0 gene did associate with axons and myelination occurred, but the myelin sheath was very thin and badly compacted. There was also an increased Schwann cell expression of other proteins, like MAG and PLP, that is thought to compensate for the loss of P0 (87).

It is also important to note that there is not only variation or mutations in myelin proteins that affect myelination in demyelinating diseases. Lipid composition also varies with the different neuropathies. Plaques from MS patients were studied and compared to white matter from normal brain, which revealed 30% less lipid content in MS patients, with decreased amounts of cerebroside and increased percentage of saturated fatty acids (88). Studies involving CMT1A with duplication of PMP22 gene revealed that transcription of proteins involved in biosynthesis of lipid components in myelin was downregulated, with differences between mildly and severely affected CMT rats (89). Lipid analysis from patients with DDS and CMT showed major alterations in lipid composition. There was a decrease in free cholesterol, glycosphingolipid and phospholipids in the connective tissue surrounding the myelin sheath and decreasing size of the long chain fatty acids in sphingolipids (90). In the same study, cholesterol and cerebroside levels in the affected patients were reduced.

MS and CMT are two out of many demyelinating diseases, and of interest is what factors may affect the formation of multilayers in myelin. Although there are many studies revealing that mutations in specific myelin proteins cause different severities of neuropathies, little is still known about how myelination occurs. Interactions between the different myelin proteins and lipid bilayer are not yet fully understood. Before the diseases can be fully comprehended and targeted drug delivery can be developed, new knowledge is needed about the specific interactions that happen between myelin proteins and lipid membranes, and pilot studies on potential drug delivery systems should be done. Nanotechnology could be useful in achieving this.

2.3 Nanotechnology

Nanotechnology deals with processes and materials in the nanometer range, which is generally between 1-100 nm (10^{-9} m). To set this into an imaginable perspective, a human red blood cell is around 7000 nm in diameter while proteins have the size between 5-20 nm (91, 92). Nanoscience spans over a broad range of disciplines: physics, chemistry, electronic technology, biology and medicine, and the similarity among them are the usage and manipulation of nanoscale objects. Properties of a bulk material change when it reaches nanoscale. At this size the properties are caused by the high surface area compared to the small size and shape. Properties that changes can be magnetic, mechanical, electrical or optical; a strong visible UV-band is exhibited in nanoparticles of noble metals like silver, palladium and gold, which is not present when the same substances are in bulk state (93). Nanoparticles, because of their special traits, can be used in many different applications.

2.3.1 Liposomes and bicelles used as model membranes mimics

To get a further understanding about how myelin proteins interact with lipid membranes, the easiest way to do that is with model systems in vitro. A model system is frequently used in research and can either be an organism or a self-contained system, which we can use to study a specific biological activity or disease processes (94). The proteins are readily expressed in *Escherichia coli* (*E. coli*) cells and can be purified and stored in desired buffers. To investigate the interaction with lipid membranes, easily obtained membrane models like liposomes or bicelles are used.

Liposomes are small spherical vesicles that can be made for different types of lipids. Depending on the lipid composition, the properties of the liposomes may differ in charge, size, permeability, and lipid mixing and phase homogeneity. The main characteristics of liposomes are that they are amphipathic, containing both hydrophilic and hydrophobic traits. When lipids are hydrated they form closed spheres of bilayers, with the hydrophobic tails pointing towards each other and the hydrophilic heads pointing out in the medium (95). The developed vesicle closely resembles cell membranes or the multi-layered myelin sheath. Size of the liposomes can vary from 30 nm to several micrometers (95). Hydrated lipids first form multilamellar vesicles (MLV) with several layers of lipid bilayers inside each other separated by water. By extrusion or sonication of the MLVs they can be made into either large or small unilamellar vesicles, abbreviated LUV and SUV respectively(96).

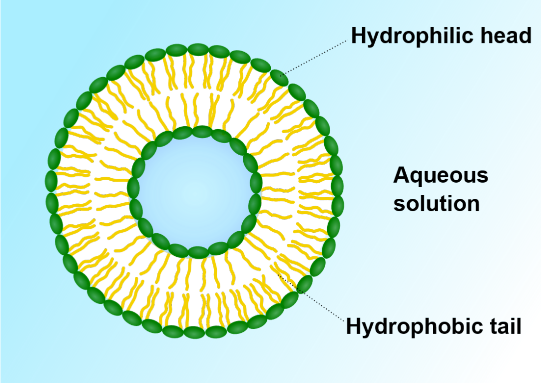

Figure 5: Illustration of a liposome formed when lipis are hydrated in water. The hydrophobic tails cluster together as they repel water with the hydrophilic heads point outwards, forming a closed vesicle of a lipid bilayer. It resembles the native bilayers found in organism and is frequently used as a model system. By SuperManu [GFDL (http://www.gnu.org/copyleft/fdl.html) or CC BY-SA 3.0 (https://creativecommons.org/licenses/by-sa/3.0)], from Wikimedia Commons

Bicelles have recently been used more and more in studying membrane proteins. They were originally developed for NMR studies, but have been adapted to other methods because they bridge the gap between liposomes and native flat bilayer found in organisms (97). When a detergent is added to a liposomes solution with a specific q-ratio, flat disk-like vesicles are formed, where the detergent enclose the exposed hydrophobic sides (98, 99). Q-ratio is the ratio between lipids and detergent. A higher q-ratio forms more elongated bilayers compare to lower ones that resembles the known liposomes. Proteins that have not crystallized with liposomes, could be crystallized in the presence of bicelles, and bicelles have been shown to stabilize membrane proteins (100).

The bilayers in the myelin sheath are as stated negatively charged and composed of many different types of lipids (18). In this project model membranes constitute of two composition of lipids, either a mix of 1,2-dimyristoyl-sn-glycero-3-phosphocholine (DMPC) and 1,2-dimyristoyl-sn-glycero-3-phosphorylglycerol (DMPG) or 1,2-dioleoyl-sn-glycero-3-phospho-L-serine (DOPS) and 1,2-dioleoyl-sn-glycero-3-phosphocholine (DOPC). DMPC is a phosphatidylcholine containing two myristoyl tails and its PC head group is zwitterionic, making it net neutrally charged, with tails being fully saturated. DMPG have also fully saturated tails but the head group is negatively charged, making the bilayers of DMPC:DMPG also net negatively charged. The phase transition temperatures of DMPC and DMPG from the gel phase to the liquid disordered phase are 24ºC and 23ºC respectively. Both DOPS and DOPC have carbon-carbon double bonds in their hydrophobic tails, making them unsaturated with cis conformation. DOPC has a head group similar to DMPC, making it zwitterionic and DOPS has a negatively charged head group, which makes the vesicles of DOPC:DOPS being negatively charged at their surface. The phase transition temperature of DOPC and DOPS are -11ºC and -17ºC, respectively (101). These simple lipid mixtures behave well as liposomes and bicelles in various analytical methods, are easy to prepare and stable over time at ambient temperatures, which makes them good model systems for studying myelin proteins.

2.3.2 Nanoparticles in medicine

In nanomedicine the research spans vaccines, imaging, implants, tissue engineering, diagnostic tools and drug delivery, using biological or nonbiological materials. In recent years, there has been a huge focus on drug delivery and how to use nanotechnology as a tool for targeted treating of diseases. To achieve the goal of using nanoparticles in drug delivery systems it is important to gain knowledge of how different nanomaterials interact with a biological environment, stability of the delivery system and the possibility of toxic effects (102). Nanoparticles like iron oxide, silicon dioxide and gold will be assessed more thoroughly here.

One of the first uses of iron oxide was as compass. In ancient China it was used by navigators to find the direction of the North Pole. Today it is used in many different scientific disciplines; biology, chemistry, geology and medicine (103). In nanomedicine, iron oxide particles are used in the diagnostic fields, drug delivery and biomedical. The iron oxide magnetite (Fe_3O_4) is a stable electrical conductor with low toxicity and nanoparticles of magnetite are used usually because of their superparamagnetic properties (104). Superparamagnetism happens in particles that have single magnetic domains; the magnetization of the particle does not vary across the particle and the magnetic moment becomes zero. But when an external magnetic field is applied the nanoparticles becomes strongly paramagnetic as they develop a strong internal magnetization (105). Iron oxide nanoparticles get superparamagnetic properties when the diameter of the core is between 10 nm and 100 nm. This property is very important, because a superparamagnetic particle can be coated and loaded with a drug which can with help from a magnet drag the particle to target tissue. When the magnetic field is stopped the nanoparticle will stay in place (106). The magnetic properties of iron oxide are also used in magnetic resonance imaging (MRI) where it is used as a contrast agent; it increases the sensitivity of MRI for depicting normal and abnormal vasculature. After intravenous administration and intracellular uptake the particles become metabolized by the lysosomes and becomes a part of the normal iron content in the body (107). Several in vitro studies have reported none or low toxicity for these nanoparticles at concentration below 50 µg/mL, but others have described DNA damage, oxidative stress, membrane dysfunction, cell death and alteration in cell motility even at low concentration (108-110). The level of toxicity seems to be dependent on cell type, size of the nanoparticles, dose, exposure time and type of coating, where citrate coated and lipid coated iron oxide nanoparticle being least toxic(111, 112)

Silicon dioxide (SiO_2), also called silica, is well suited for biomedical applications because it is presumed safe to humans as it used as a food additive, excipient for drugs and vitamins and is readily absorbed in tissues, bones, liver and kidney. Silicon dioxide deficiency has shown to cause bone deformities and poorly formed joints (113). Silica is hydrophilic and stable in a physiological environment and is under research as biosensors, drug delivery and cellular uptake (114-116). Amorphous silica nanoparticles with varying size (10-400 nm) have shown no effect on cell morphology with concentration up to 19 µg/mL, but fine crystalline silica particles did reduce cell viability up to 80% (116). Size-dependent toxicity of silica nanoparticle might be an important factor in using them in nanomedicine. Nanoparticles in the size range of 30-40 nm have induced damage to cell membranes, increased cell death and dysfunction of mitochondria (117). On the other hand it seems like adverse effects might be due to acute exposure, while chronic exposure do not cause significant toxicity (118). Toxicity studies of how silica affects biological system relative to size, concentration and exposure time is needed for safer use in biomedical applications.

Gold (Au), as a bulk material, is a natural element which is used in jewelry and in coins. As a metal it has good electrical and thermal conductivity without corrosion. This fine element have also been used in medicine since the 1st century BC in treating wounds, diarrhea, leprosy, plague and even metal diseases and syphilis (119, 120). Since then, the use of gold, particular gold nanoparticles (AuNPs), have been highly studied for usage in biosensors, clinical chemistry, detection, bioimaging, therapy, diagnostics, drug delivery and the list goes on. Gold is seen as very biocompatible and is considered as chemically inert, but some studies have revealed that toxicity and accumulation of gold is dependent on size and surface chemistry(121). It has been argued that gold can be used in almost any medical application and this is based on their unique physical and chemical properties (120). The physical properties of AuNPs are strongly influenced by their size and shape where two interesting properties being surface plasmon resonance and magnetism (122). Surface plasmon resonance (SPR) is the main optical feature of AuNPs with size of 2-100nm. Plasmons are oscillations of free electrons in metals and can be describes as a negatively charged cloud of electrons that are coherently displaced from its equilibrium position around positively charged ions (123). When light hits the nanoparticles the electron cloud gets excited and starts to oscillate resulting in a strong extinction of light. The plasmon extinction band can be detected using ultraviolet-visible spectroscopy and is strongly dependent on size and shape. When the size of the AuNP is much smaller than the light wavelength the distribution on the electric field in the particle is uniform; the electron cloud polarization is coherent over the particle. But when the size is larger (> 100nm) the electric field distribution is no longer uniform and both transversal and longitudinal surface plamons resonance occurs (122, 123). The wavelength of absorbed light increases with increasing nanoparticle size, which means that gold nanoparticles have different colour depending on size. Small nanoparticles that absorb visible light with wavelength of 430nm to 560nm, the blue-green part of the spectrum, will reflect reddish light (580-800 nm). As the size increases, the wavelength absorbed shifts to longer wavelength. If red light is absorbed the color will appear blue, beyond that the wavelength are in the infrared portion of the spectrum giving a clear color (124, 125). Shape of the AuNPs also has an effect on the SPR, where the absorption spectra are different from spheres, rods, cubes, triangles and stars. Spheres provide one peak in the spectra while rods yields two peaks, one transverse and one longitudinal (126).

Gold in bulk material is diamagnetic, it repels a magnetic field, but once the size is in the nano range it becomes magnetic. This odd property have been shown in small gold clusters (10-40 atoms) up to around 5 nm, but the results are rarely reproducible and often contradictory. But findings reveal that magnetism decreases with increased size and some temperature dependence, where a 2 nm wide particle showed stable magnetism at around 130 ºC, which is odd since traditional magnetic materials often become unstable at high temperatures (127)

SPR has become a key parameter in many applications like nanosensing, nanolabeling, while colloidal gold can be used in bioimaging due to the high electron density. Proteins or cells can be tagged with gold and visualized in transmission electron microscopy (TEM), scanning electron microscopy (SEM) or fluorescence microscopy. Effective use of AuNPs or any other as nanovectors for drug delivery is highly due to many possible surface modifications (120, 128).

The great promises of applications of nanoparticles in medicine are not just about their high surface to volume ratio, size, shape, optical and magnetic properties, but the use of these properties together with the ability to functionalize them, thus changing their surface. Surface modifications can effect nanoparticle stability, monodispersity and biocompatibility, and provide functional groups like $-COO^-$, $-NH_3^+$ and -CHO (129). To make nanoparticles more "cell"-like, mechanism for coating and functionalization of the surface have been more directed into using biomolecules like phospholipids to coat nanoparticle surfaces, where one of the most used approaches is self-assembled monolayers (SAM) by thiol functionalization (130). SAMs are assemblies of organic compounds formed by absorption from solution onto a solid surface, where the organic molecular constituents have a head group with specific affinity for the substrate. SAMs forms spontaneously, where particularly thiols on gold surfaces have shown to be easy to prepare and to gain a well-defined order (131). Thiol functionalization is often through ligand exchange, where citrate-stabilized gold nanoparticles are commonly used. Thiols contain a –SH group and the sulfur binds stronger to Au than citrate, so that in a ligand exchange process the thiol molecules will spontaneously displace the citrates resulting in a coating of thiols surrounding the AuNPs (132). Bilayers of lipids can then form onto the thiol coated AuNPs with the association between hydrophobic lipid tail and the hydrophobic thiol monolayer (1). The resulting lipid coated nanoparticles can be further used to study membrane-associated phenomena like protein-membrane interaction and investigate possibilities as therapeutic cargos (133, 134).

2.4 Modern research

2.4.1 Protein-membrane model systems

Biological membranes plays major role in regulating many different interaction such as cell-to-cell interaction, signalling pathways via receptors on the cell membrane or protein-membrane interactions in the myelin sheath, as described above. Membranes have major differences in composition depending if it is a cell membrane, surrounding organelles, or being the insulation around neurons. The complexity of biological membranes and their interaction with proteins drives the development of finding simpler model systems where size, composition and desired shape can be tailored with precision. Model systems are mainly used to simply complex systems so that the roles of individual components can be addressed (135). Since myelination is still not fully understood and how both the lipid bilayers and myelin protein contribute to demyelinating diseases, good model systems are necessary to obtain new information. Liposomes have for a long time been used for this purpose, forming lipid bilayered vesicles resembling the bilayers in the myelin sheath. Bicelles on the other hand forms bilayers in disk-form, which looks more like the "flat" native bilayers. Thus, bicelles might be more biological relevant as a model membrane for investigating protein-membrane interactions in the myelin sheath (136).

2.4.2 Nanotechnology in treating neurological diseases

Neurological diseases if one of the major health concerns worldwide with many disorders left untreated, with orthopaedic aids and training as the only means to reduce disease progression. For diseases involving the CNS, the main problem for drug administration is the blood-brain barrier which tightly regulates the movement of ions and molecules into the brain (137). Studies of getting drugs through the barrier have been positive with the use of nanoparticles such as liposomes loaded with a certain drug and gold with specific surface modifications (138). Nanoparticles of the rare earth metal cerium has shown to protect against cellular damage in neurological disorders, and a study proved that cerium oxide nanoparticles relieved clinical symptoms and motor deficits in mice with a murine model of MS (139, 140). Gold nanoparticles is studied for treatment of Alzheimers disease, where research have found that AuNPs have the potential to slow down disease progression without harmful effects in the brain (141, 142). Nanoparticles can also be used for diagnostic purposes, with different modifications and coatings, providing reliable detection system for neurological diseases like the lethal disease amyotrophic lateral sclerosis (143). Targeted drug delivery for peripheral neuropathies is also being studied with some promising results. One research group studied the use of nanoparticles in neuron targeted drug delivery in an animal model with peripheral nerve crush injury as a model for peripheral neuropathies. The nanoparticle carried the brain-derived neurotrophic factor (BNDF) that has a protective role in neural survival. Results displayed release and expression of BNDF which lead to enhanced recovery and higher density of myelinated axons (144).

Even though nanotechnology usage in neuroscience is rising and looks very promising, safety and toxicity concerns are yet to be determined together with increased knowledge of biocompatibility and biodegradability of nano-carriers.

2.5 Aims

2.5.1 Investigate protein-membrane interaction with the use of two model membranes

Many major myelin proteins have already been isolated and characterized, but little is still known about their 3D structure and their molecular mechanisms in myelin formation. The aim was to study the structure, function, and dynamics of the myelin proteins MBP, P2 and P0 with the employment of two major model systems for protein-membrane interactions: liposomes and bicelles. Gaining further insight into the molecular interactions of myelin proteins with lipid membranes is important for understanding nervous system development and demyelinating diseases. Increased knowledge about the differences between the model systems was also investigated to see if one could be preferred over the other, and maybe represent a better model for in vitro studies of the myelin membrane and myelin proteins associated with neurodegenerative neuropathies. The myelin protein MBP, P2 and P0ct was expressed and purified for the aims of this project, with the mutant P2 F57A already been purified. Further characterization of differences in protein-membrane interaction were carried out using a wide array of methods to determine concentration dependency, aggregation effects, thermal stability as well as uncover repeat distances within a myelin model system. Transmission electron microscopy (TEM) was used to get clear insight into the overall difference in how myelin proteins stack liposomes and bicelles.

2.5.2 Pilot study: using nanoparticles to understand protein-membrane interaction and for drug-delivery

Nanoparticles are currently under intense study for drug delivery approaches. Here, nanoparticles are used to observe protein-membrane interactions and how nanoparticles interact with myelin-like multilayered membranes. Several technologies have been developed for studying protein-membrane interactions: nanoparticle-embedded supported lipid bilayers, lipid-coated nanoparticles in solution, “nanoantennas”, vesicle systems for characterizing lipid domain formation upon protein binding and single-molecule kinetics of protein-membrane interactions (145-149).

The aim of this project was to gain insight in how lipid-coated nanoparticles could easily be made and to use them to investigate interactions between proteins and lipid membranes. The iron oxide and silica dioxide nanoparticles with lipid coatings were received from our collaborator Chaozhan Wang, while the citrate stabilized gold nanoparticles were purchased from NanoComposix to be coated with DMPC:DMPG lipids prior to further investigation. Protein binding to the nanoparticles was tested with co-sedimentation assay, and coating of gold nanoparticles was studied with UV-VIS spectroscopy and TEM.

3 Methods and materials

The following section describes the methods and materials used in this thesis. First is the protein expression and purification of the four different protein and vesicle preparation before it addressed the nanoparticles and analytical methods used to investigate the aims of this thesis. Theory behind the different methods is explained in Appendix 8.7.

Special reagents

- Gold nanoparticles 80nm (± 9 nm) (AuNPs 80 nm, Bare – citrate, NanoComposix, product nr: AUCB80-1M, Lot nr: BAM0117)
- Iron(II,III)oxide coated nanoparticles (10 nm and 150 nm, via collaborator Professor Chaozhan Wang (Ph.D. professor of chemistry, Collage of Chemistry and Materials Science)
- Silicon dioxide coated nanoparticles via collaborator Chaozhan Wang (Ph.D. professor of chemistry, Collage of Chemistry and Materials Science)
- 1-Octanethiol (≥ 98.5%, Sigma-Aldrich, Lot nr: 06017031)
- Nickel-nitrilotriacetic acid (Ni-NTA)-agarose resin (Thermo Scientific and Qiagen, Lot nr: 160028556)
- Amylose resin (BioLabs, Lot nr: 0191607)
- Lyzosyme from chicken egg white (Sigma-Aldrich, Lot nr: SLBJ4107V)
- cOmplete ethylenediaminetetraacetic acid (EDTA)-free protease inhibitor tablets (Roche, Lot nr: 31880700)
- 2% uranyl acetate (provided by the Molecular Imaging Center (MIC), Department of Biomedicine, University of Bergen)
- Phenylmethylsulphonyl fluoride (PMSF) (≥99.0% ,MBV International Corporation, Lot nr: 51148)
- LB broth (Sigma-Aldrich, Lot nr: BLBV6991)
- 4-(2-hydroxyethyl)-1-piperazineethanesulfonic acid (HEPES) (≥ 99.5%, Sigma-Aldrich, Lot nr: SLBS2995V)
- Imidazole (≥99.5%, Sigma-Aldrich, Lot nr:S2BF3550V)
- Urea (≥ 99.5%, Roth, article nr: 3941.2)
- Sodium Chloride (≥ 99.5%, Sigma-Aldrich, Lot nr: SLB2340V)
- isopropyl-β-D-thiogalactopyranoside (IPTG) (≥ 99%, Apollo Scientific, Lot nr: AS469178)
- Chloramphenicol (Sigma-Aldrich, Batch nr: 123K0588)
- Ampicillin (Apollo Scientific, Lot nr: AS454596)
- Methanol (99%, Sigma-Aldrich)
- Chlorofom (99%, Sigma-Aldrich)
- 1,2-dimyristoyl-sn-glycero-3- phosphoglycerol (DMPG) (Larodan AB, Lot nr: E056:2)
- 1,2-dimyristoyl-sn-glycero-3-phosphocholine (DMPC) (Larodan AB, Lot nr: M032:1)

- 1,2-dioleoyl-sn-glycero-3-phospho-L-serine (sodium salt) (DOPS) (Avanti polar lipids, Lot nr: 181PS-345)
- 1,2-dioleoyl-sn-glycero-3-phosphocholine (DOPC) (Avanti Polar lipids, Lot nr: 850375-01-321)

3.1 Protein expression and purification

The purification process of MBP, P2wt and P0ct is based on optimized protocols (40, 60, 69).

3.1.1 Myelin basic protein (MBP)

MBP starting culture was made by mixing LB medium with 100 µg/mL ampicillin and 35 µg/mL chloramphenicol. The strain of *E. coli* (BL21(DE3)pLysS RARE pTH27 MBP) was added from a frozen stock. The *E. coli* strain is transformed with a pTH27 vector including an N-terminally hexahistidine (His_6) tag, Tobacco Etch Virus (TEV) protease cleavage site (ENLYFQG) and finally the protein (His-rMBP). The MBP start cultures were then incubated over night at 37 °C and 180 rpm constantly shaking.

After growth of the start culture, start culture was added to autoclaved LB medium (10 g/L tryptone, 5 g/L yeast extract, 5 g/L NaCl in water) to every liter of Milli-Q water) together with 100 µg/mL ampicillin. The batches were then cultured at 37 °C and 180 rpm. The optical density (OD) was checked regularly every 60-90 min to confirm growth and to verify that the cultures had an OD (at wavelength 600nm) near 0.3 before adding isopropyl-β-D-thiogalactopyranoside (IPTG), to induce the expression of MBP. IPGT were added to 0.4 mM when optical density was reached. The cells were then allowed to express for two hours at 37 °C and 180 rpm constant shaking.

After expression, the cultures were centrifuged at 6000 G for 20 minutes at 4 °C and the supernatant was removed. The harvested cells were then resuspended in lysis buffer (50 mM 4-(2-hydroxyethyl)-1-piperazineethanesulfonic acid (HEPES) pH 7.5, 500 mM NaCl, 6 M urea, 20 mM imidazole) in a final volume of 40 mL. 400 µL of 100 mM phenylmethylsulphonyl fluoride (PMSF; solution prepared in isopropanol) and 1.6 mL of EDTA-free protease inhibitor (Roche, 25x) was added to the mixture before sonicating with 1 s. pulse and 1 s. wait for a total of 5 min, with an output power of 24 W. Cell debris was then removed by centrifugation using SS-34 rotor at 30 000 G, 4 °C for 40 minutes.

Further purification of the protein was done using Ni-NTA affinity chromatography where Ni-NTA agarose matrix (Qiagen) was used to bind His_6-proteins. Ni^{2+} cations have a high affinity for the N-terminal polyhistidines which is used to separate wanted protein from cell debris. The Ni-NTA agarose matrix was washed with Milli-Q water and equilibrated with 10 matrix volumes of lysis buffer before the supernatant was added at 4 °C. 10 matrix volumes of lysis buffer were added after collecting the unbound fraction. The columns were incubated with 2.5 matrix volumes elution buffer

(4.8 M urea, 40 mM HEPES, 400 mM NaCl, 500 mM imidazole, pH 7.5) divided into two; first fraction was allowed to incubate for 10 min before adding a second volume of elution. All fractions were collected separately. The elution fractions were subjected to sequential dialysis to lower the urea content from 4.8 M to 2 M. First the fraction was dialyzed against 4 M urea, 40 mM HEPES and 400 mM NaCl for 2.5 h before changing buffer to 2 M urea, 40 mM HEPES, 400 mM NaCl for 3.5 hours. To digest the N-terminal His_6-tag of His-rMBP 4.5 μM recombinant TEV protease was added. Cleavage was done overnight at 4 °C with a dialyzing buffer containing 1 M urea, 40 mM HEPES and 400 mM NaCl. Dialysis was performed using dialysis membrane with a molecular weight cut off between 12-14 kDa (Spectrum Labs Secptra/Por 4 Dialysis Tubing, 12-14 kD MWCO, 45 mm Flat-width, part nr: 132706).

After dialyzing the digested protein back into 6 M urea, 50 mM HEPES, 500 mM NaCl and 20 mM imidazole for 3.5 h, another Ni-NTA chromatography was performed to remove cleaved His_6-tags and His-tagged TEV protease. The matrix was equilibrated with 10 matrix volumes before adding the dialyzed protein. The unbound fraction was collected before adding 3 matrix volumes of lysis buffer. The matrix was then incubated for 10 minutes with elution buffer before collecting the fraction. The unbound and washing fraction was then dialyzed against 20 mM HEPES, 400 mM NaCl with pH 7.5 overnight to reduce urea content.

Before gel filtration the dialyzed fraction was filtered through a 0.45-μm filter (Filtropur, Sarstedt, Lot nr: 51503103) before concentrating the sample using an Amicon Ultra-15 10K centrifugal filter device (Millipore). The protein was concentrated down to 2 mL before running gel filtration chromatography on a Superdex 75 10/300 GL column (GE Healthcare) using a 500 μL loop with a BioRad DuoFlow system. Before running the protein the column was washed with filtered and degassed Milli-Q and then equilibrated with filtered and degassed buffer containing 20 mM HEPES, 150 mM NaCl with pH 7.5. Protein fractions around the major elution peak were collected. The fractions were then checked with NanoDrop 2000 spectrophotometer (Thermo scientific) and SDS-PAGE to determine concentration and purity of the protein. The fractions were then aliquoted and stored at -80 °C until usage.

3.1.2 P0ct wild type

P0ct starting culture was by mixing LB medium and 100 μg/mL ampicillin. The strain of *E. coli* (BL21(DE3) pHMGWA P0ct) was added from a frozen stock. The *E. coli* cells contain a pHMGWA vector which contains an N-terminal His_6-tag, maltose binding protein (MaBP), TEV protease cleavage site followed by the P0ct gene (His-MaBP-P0ct). The P0ct start culture was then incubated over night at 37 °C, 180 rpm constant shaking.

100 µg/mL of ampicillin was added to autoclaved LB-medium batches before P0ct start culture was included. The batches were then cultured at 37 °C and 180 rpm. OD was checked to verify that the cultures had an OD between 0.4 and 0.8 before adding IPTG, to induce expression of P0ct. IPGT were added to 0.4 mM when optical density was reached. The cultures were then allowed to express for 3 h at 37 °C and 180 rpm constantly shaking.

After expression, the cultures were centrifuged at 6000 G for 20 minutes at 4 °C and the supernatant was removed. The harvested cells were resuspended into lysis buffer (40 mM Tris-HCl, 400 mM NaCl, 20 mM Imidazole, pH 8.5) in a final volume of 20 mL. 1 mL of protease inhibitor (Roche 25x) was added to the mixture. P0ct was then lysed with 1 s. pulse with 1 s. wait for a total of 5 min with an output power of 24 W. The lysate was then centrifuge for 30 minutes at approximately 35 000 G before purification with Ni-NTA chromatography.

The Ni-NTA agarose matrix (Qiagen) was washed with of Milli-Q water before equilibrated with 10 matrix volumes of wash buffer (40 mM HEPES, 400 mM NaCl, 20 mM imidazole, pH 7.5). At 4 °C, the protein supernatant was added to the column and collected. The matrix was washed with 10 matrix volumes of wash buffer before the his$_6$-tagged protein was eluted using 2 matrix volumes elution buffer (40 mL wash buffer + 10 mL2.5 M imidazole) and 1 matrix volume of 1M Imidazole. The elution fractions was then dialyzed at 4 °C against 20 mM Tris-HCl, 400 mM NaCl and 1 mM DTT for 1 h before adding 4.5 µM TEV protease and continued dialyzing overnight. Dialysis was preformed using dialysis membrane with a molecular weight cut off between 6-8 kDa (Spectrum Labs Secptra/Por 4 Dialysis Tubing, 6-8 kD MWCO, 45 mm Flat-width, Lot nr: 9200204).

Amylose resin chromatography was applied to remove the cleaved His-maltose binding protein (His-MaBP). Amylose-resin was washed with of Milli-Q and equilibrated with 10 matrix volumes of wash buffer (20 mM Trish-HCl, 400 mM NaCl, pH 8.0). The dialyzed fraction was added and collected. The column was incubated for 10 minutes with elution buffer (20 mM Tris-HCl, 400 mM NaCl, 10 mM maltose, pH 8.0) before adding elution buffer once more. The matrix was washed with 10 matrix volumes of milli-Q water and re-equilibrated before the collected unbound fraction was subjected to another amylose resin chromatography, performed in an identical fashion.

Before gel filtration, the protein fraction was filtered through 0.22-µm (Sterile syringe filter, VWR international, Batch nr: 13298298) and concentrated down to 2 mL using Amicon 3K MWCO centrifugal filter device (Millipore) at 6000 rpm, 4 °C with 2-15 min intervals. Gel filtration chromatography was done using a Hiload Superdex 75 16/60 (GE healthcare) column with a BioRad DuoFlow system. The buffer used for equilibrating the column contained 20 mM HEPES pH 7.5 and 150 mM NaCl. Fractions were collected around the major peak in the chromatogram. The fractions were pooled and concentrated, using the same type of centrifugal filter device as earlier, down to 1 mL. The concentration was checked with NanoDrop 2000 spectrophotometer before the concentrated fraction was aliquoted and stored at -80°C until usage.

3.1.3 P2 wild type and P2 F57A

Start cultures was made in LB medium, 100 µg/mL ampicillin and 35 µg/mL chloramphenicol. Two types of strains (both based on *E. coli* Rosetta(DE3)) were added from a frozen stock. Both strains contain a pTH27 vector containing N-terminal His_6-tag followed by a TEV protease cleavage site and the gene coding for the p2wt or the mutant F57A. The start culture mixtures were incubated over night at 37 °C and 180 rpm constantly shaking.

To make two batches of ZYM-5052 autoinduction media (F. William Studier) for each protein, ZY-medium (1% NZ-Amine AS, 0.5% yeast extract (Sigma & Aldrich)) was autoclaved. The ZY media was supplemented with 10 mL of 50xM (25 mM Na_2HPO_4, 25 mM KH_2PO_4, 50 mM NH_4Cl, 5 mM Na_2SO_4), 1 mL of 2 mM $MgSO_4$ and 100 µL 1000x Trace Metals (50 mM $FeCl_3$, 20 mM $CaCl_2$(x2 H_2O), 10 mM $MnCl_2$(x4 H_2O), 10 mM $ZnSO_4$(x7 H_2O), 2 mM $CoCl_2$(x6 H_2O), 2 mM $CuCl_2$, 2 mM $NiCl_2$, 2 mM Na_2MoO_4, 2 mM Na_2SeO_3 and 2 mM H_3BO_3) before 0.5% glycerol, 0.05% glucose, 0,2% Alfa-D-lactose was included to each batch. 100 µg/mL ampicillin, 34 µg/mL chloramphenicol and starting culture were added to the ZYM-5052 medium. The batches were then incubated at 18 °C for 72 h at 180 rpm constant shaking.

The supernatant was removed by centrifugation at 6000 G at 4°C for 30 minutes. The harvested cells were resuspended in lysis buffer (50mM Na-phosphate pH 8.0, 300 mM NaCl, 10 mM imidazole) to a total of 45 mL before adding 2 mL of dissolved protease inhibitor (Roche 25x). 10 mg/mL of lysozyme (Sigma-Aldrich, Lot nr: SLBJ4107V) was added to each suspension. The batches were then sonicated at 25 watts for 10 s with 30 s intervals (7 repetitions) before centrifuging at 20 000 G for 45 minutes at 4 °C. The supernatant was filtered with a 0.45-µm pore size (Filtropur, Sarstedt, PFTE membrane, Lot nr: 51503103) filter.

Ni-NTA chromatography was performed for further purification. Ni-NTA agarose matrix (Qiagen) was washed it with 10 matrix volumes of Milli-Q, equilibrated with 10 matrix volumes of lysis buffer before adding the filtered supernatant. The flow-through was collected and re-added 2 times. 10 matrix volumes of wash buffer (50 mM Na-phosphate pH 8.0, 300 mM NaCl, 20 mM imidazole) was added and collected. The matrix was eluted with 4 volumes elution buffer (50 mM Na-phosphate, 300 mM NaCl, 400 mM Imidazole, pH 7.5) where the first fraction was incubated for 10 minutes. Matrix was finally eluted with 1 M imidazole. The elution fractions were pooled and 4.5 µM TEV protease was added before dialyzing against 50 mM Na-phosphate pH 8.0, 300 mM NaCl and 1 mM DTT overnight. Dialysis was performed using dialysis membrane with a molecular weight cut off between 6-8 kDa (Spectrum Labs Secptra/Por 4 Dialysis Tubing, 12-14 kD MWCO, 45 mm Flat-width, part nr, 132706)

Before the overnight dialyzed solution was subjected to a second Ni-NTA chromatography the matrix was washed and equilibrated with 3 volumes of buffer (50 mM Na-phosphate pH 8.0, 300 mM NaCl). The dialyzed fraction was added and re-added 2 times. The flow-through was collected in one tube. 3 volumes of wash buffer were added before lysis buffer. Matrix was eluted with elution buffer and 1 M imidazole.

Before the final step, flow-through and wash fractions was pooled and concentrated down using an Amicon ultra-15 3 kDa molecular weight but off centrifugal filter device (Millipore) at 4°C, 4000 G with 2-15 minutes intervals. The concentrated protein was filtered through a 0.22 μm pore size filter (Sterile syringe filter, VWR international, Batch nr: 13298298). Gel filtration chromatography was carried out using a Hiload Superdex 75 16/60 gel filtration column using a BioRad DuoFlow system. The column was equilibrated with degassed and filtered buffer (20 mM HEPES pH 7.5, 150 mM NaCl). Fractions were collected around the major peak in the chromatogram. Fractions from the gel filtration were pooled and concentrated with Amicon 3K MWCO centrifugal filter device (3000 G, 4°C, 5-10 minutes intervals). Final volume was 1 mL and the concentration was determined using NanoDrop 2000 spectrophotometer. The protein was aliquoted and stored at -80°C until usage.

Expression and purification of P2 F57A was done during the course BMED325 Cellular biochemistry and nanobiochemistry and not during this master project.

3.2 Sodium dodecyl sulphate polyacrylamide gel electrophoresis (SDS-PAGE)

Sodium dodecyl sulfate polyacrylamide gel electrophoresis (SDS-PAGE) was used to monitor all purification steps. Samples from different fractions and purifying steps were taken and mixed with 5x loading dye (300 mM Tris-HCl pH 6.8, 10% (w/v) SDS, 50% (v/v) glycerol, 0.05% (w/v) bromphenol blue, 10% (v/v) β-merceptoethanol) followed by denaturation at 95ºC over minimum 3 min (150). The samples were then loaded onto a 4-20% precast SDS-PAGE gels (Bio-Rad 456-1096, MiniProtean TGX 4-20%) together with 2 μL of pre-stained protein molecular weight standard (Thermo Fisher PageRuler pre-stained protein ladder, either #26616 or #26619). Electrophoresis was performed with a constant voltage of 200 V in room temperature with a SDS-PAGE buffer (25 mM Tris pH 8.3, 192 mM Glycine, 0.1% (w/v) SDS) using a Bio-Rad Power Pac 300. Gels were stained with InstantBlue (Expedeon, Lot nr: 170823330) and distained with distilled water. Imaging of the gels was taken with a Bio-Rad (ChemiDoc XRS+) with Image Lab software (coomassie stained gel settings and automatic exposure time).

Same principles were used for co-sedimentation assays and checking protein binding; Identical loading buffer, gel, and buffer and staining solution was used each time.

3.3 Preparation of vesicles and bicelles

3.3.1 Preparation of liposomes and bicelles

Liposomes with different ratios of 1,2-dimyristoyl-sn-glycero-3-phosphocholine (DMPC) and 1,2-dimyristoyl-sn-glycero-3- phosphoglycerol (DMPG) or 1,2-dioleoyl-sn-glycero-3-phospho-L-serine (sodium salt) (DOPS) and 1,2-dioleoyl-sn-glycero-3-phosphocholine (DOPC) were prepared depending on the experiments. The lipids was dissolved in chloroform (99%, Sigma Aldrich**)** and methanol (99.9%, Sigma Aldrich) and then divided into batches with ratios of 1:0, 1:1, 1:4 and 1:9 relative to methods used, before the batches were dried with liquid nitrogen and frozen at -20°C until usage. Buffer containing 20 mM HEPES, 150 mM NaCl, pH 7,5 or Milli-Q water was used as hydration medium depending on the experiment. A freeze-thaw cycle was done after the liposomes had hydrated overnight. The liposomes were flash frozen in liquid nitrogen, thawed in a warm water bath before heavily vortexed for 30 sec. The cycle was done seven times to decrease multilamellarity. Extrusion was done with a 100 nm filter to create large unimellar vesicles (LUV). Small unimellar vesicles (SUV) are made by sonicating (Sonics & Materials Inc. Vibra-Cell VC-130) at 4 watts with 10 seconds intervals to a clear solution.

To prepare bicelles, 10% dodecylphosphocholine (DPC) was diluted to the same concentration as the liposomes before adding it to a mixture of hydrated DMPC:DMPG (independent of DMPC:DMPG ratio) with a q-ratio of 2.85 (76% lipids and 26% DPC) by pipetting the suspension up and down until a clear suspension formed. The q-ratio is:

$$\mathrm{q} = \frac{lipid\ molarity}{detergent\ molarity}$$

Lipids and bicelles were always prepared fresh for each experiment and used immediately after.

3.4 Nanoparticles

3.4.1 Gold nanoparticles

Gold nanoparticles (AuNPs) with the diameter of 80 nm (± 9 nm) were purchased from NanoComposix. 1-octanethiol (98.5%) was ordered from Sigma-Aldrich, while DMPC and DMPG were acquired from Avanti Polar lipids.

3.4.1.1 80 nm gold nanoparticles (bare – citrate) coated with 1-octanethiol and DMPC:DMPG

Monodisperse coated Au nanoparticles were prepared by modified protocols from two different articles (1, 151). The modified version from "Strong resistance of citrate anions on metal nanoparticles to desorption under thiol functionalization" (132) is in short; 100 µL of 80 nm AuNPs was centrifuged at 4000 rpm for 10 minutes and the resulting supernatant was discarded. 100 µL of 1 mM ethanolic thiol solution (1 mM 1-octanethiol in ethanol) was added to the AuNP pellet and quickly transferred to a glass vial and left at room temperature overnight. The functionalized AuNPs were then centrifuged and dispersed in ethanol 2 times to removed excess citrates and thiols, before adding 100 µL of DMPC:DMPG (1:1, 2 mg/mL, hydrated in Milli-Q) to the AuNPs. The solution was left for 48 h before sonicated until the AuNPs was dispersed. A dark red/magenta color appeared after sonication.

The protocol from "Evidence for patchy lipid layers on gold nanoparticle" (1) was modified as follows; 100 µL of AuNPs was centrifuged to remove excess citrates and redispersed in 50 µL 20 mM HEPES buffer. 50 µL of lipid solution (2 mg/mL, 1:1 DMPC:DMPG) was added to the AuNP mixture. The solution was transferred to a glass vial before adding 100 µL of 1-octanethiol (5 µg/mL ethanol) and incubating overnight at room temperature. The next day the solution was centrifuged (4000 rpm, 10 min at 22 ºC) and the AuNP pellet was washed and resuspended in 20 mM HEPES buffer.

3.4.2 Iron(II,III)oxide and silicon dioxide

Modified Iron(II,III)oxide (Fe_3O_4) and silicon dioxide (SiO_2) nanospheres were prepared and made via collaborator Ph.D Professor Chaozhan Wang at Northwest University, College of Chemistry and Materials Science.

10 nm and 150 nm Fe_3O_4 NPs was coated with SiO_2 and then modified with octadecyltrichlorosilane (ODS). Further coating was done with 1,2-dipalmitoyl-sn-glycero-3-phosphocholine (DPPC) or 1,2-dimyristoyl-sn-glycero-3-phosphatidic acid (sodium salt) (DMPA). SiO_2 nanospheres were modified with ODS before coating with DPPC or DMPA. See overview in Table 1.

The procedure for coating nanospheres with DPPC/DMPA is in short: DPPC or DMPA was fully dissolved in methanol/trichloromethane 1:1 solution before the organic solvent was removed by a nitrogen (N_2) stream, leaving a lipid film in the vials. The lipids were re-suspended into water via vortex-freeze-thaw cycles with a final concentration of 0.15 mM. With a concentration of 0.15 mg the ODS modified nanospheres were dispersed into 10 mL of 0.15 mM DPPC or DMPA solution and shaken for 1 hour. To collect the nanoparticles, either magnetic separation or centrifuge was used. The finished nanoparticles were washed with water 3 times before dried in vacuum at 50 ºC. The particles were characterized by SEM, excluded the Fe_3O_4@ODS-DDPC and the Fe_3O_4@ODS-DMPA which was too small to be imaged clearly with SEM. SEM images forwarded from Professor Chaozhan Wang can be seen in Appendix 8.2.

Table 1: Overview of the different iron(II,III)oxide and silicon dioxide nanoparticles made via collaborator Chaozhan wang (Ph.D Professor of Chemistry). All nanoparticles are coated with octadecyltrichlorosilane (ODS) before further coating with either 1,2-dipalmitoyl-*sn*-glycero-3-phosphocholine (DPPC) or 1,2-ditetradecanoyl-*sn*-glycero-3-phosphate (DMPA).

Nanoparticles	**Modification**
Fe_3O_4@ODS (10 nm)	Fe_3O_4 was coated with SiO_2 and then modified with octadecyltrichlorosilane
Fe_3O_4@ODS-DPPC (10 nm)	Fe_3O_4@ODS (10 nm) modified with 1,2-dipalmitoyl-*sn*-glycero-3-phosphocholine.
Fe_3O_4@ODS-DMPA (10 nm)	Fe_3O_4@ODS (10 nm) modified with 1,2-dimyristoyl-*sn*-glycero-3-phosphatidic acid, sodium salt.
Fe_3O_4@ODS (150 nm)	Fe_3O_4 was coated with SiO_2 and then modified with octadecyltrichlorosilane.
Fe_3O_4@ODS-DPPC (150 nm)	Fe_3O_4@ODS (150 nm) modified with 1,2-dipalmitoyl-*sn*-glycero-3-phosphocholine.
Fe_3O_4@ODS-DMPA (150 nm)	Fe_3O_4@ODS (150 nm) was modified with 1,2-dimyristoyl-*sn*-glycero-3-phosphatidic acid, sodium salt.
SiO_2@ODS	The SiO_2 was modified with octadecyltrichlorosilane.
SiO_2@ODS-DPPC	SiO_2@ODS modified with 1,2-dipalmitoyl-*sn*-glycero-3-phosphocholine.
SiO_2@ODS-DMPA	SiO_2@ODS modified with 1,2-dimyristoyl-*sn*-glycero-3-phosphatidic acid, sodium salt.

3.4.3 Coating of Iron(II,III)oxide with DMPC:DMPG

To verify successful coating of Fe_3O_4@ODS (150 nm) with DMPC:DMPG (1:1) with the instructions from professor Chaozhan Wang; 5 mg of DMPC:DMPG was hydrated with Milli-Q water to reach 0.15 mM concentration followed by 7 freeze-thaw cycles. 0.15 mg of Fe_3O_4@ODS were weighed and dispersed in 10 mL of 0.15 mM DMPC:DMPG solution and shaken for 1 h. The NPs were collected with magnetic separation and washed three times with Milli-Q. Same procedure was repeated with 1.5 mM concentration of DMPC:DMPG and 1.6 mg of Fe_3O_4@ODS to check any differences. Coated nanoparticles were tested with the MBP and 5 mM 1:1 DMPC:DMPG and DOPS:DOPC used as positive controls. Completed mixtures were left in water instead of dried in vacuum. Co-sedimentation assay was done to check protein binding.

3.5 Analytical methods

3.5.1 Co-sedimentation assays

3.5.1.1 Protein binding to lipid coated AuNPs

To assess binding between protein and nanoparticles, protein co-sedimentation was done. 0.5 mg/mL of protein (MPB, P2wt and P0ct) was mixed with 1.09 mg/mL of NPs, to a total volume resulting in a protein concentration of 0.2 mg/mL in final sample. The samples were left to incubate in ambient conditions for at least 15 min before centrifuging for 15 min, 20817 G at 22 ºC, to separate protein bound to NPs from soluble protein. Pellets were resuspended in 1% SDS before the protein content in supernatant and pellet were analysed using SDS-PAGE. Same method was used with 5.0 mM liposomes (DMPC:DMPG 1:1) as a control. Protocol for SDS-PAGE analysing is the same as described in paragraph 2.1.

3.5.1.2 Protein binding to Fe_3O_4 and SiO_2 coated nanoparticles

Nanoparticles (NPs) of iron(II,III)oxide (Fe_3O_4) and silicon dioxide (SiO_2) were ordered from collaborator Chaozhan Wang (Ph.D. Professor of Chemistry). The nanoparticles were coated with either DMPA or DPPC. The NPs were received as dried powder, to be hydrated with desired buffer before usage. Testing of the NPs was done with co-sedimentation assay to check protein binding. All NPs were weighed and a buffer containing 20 mM HEPES pH 7.5, 150 mM NaCl was added to the powder to give a final concentration of 2 mg/mL. The NPs were sonicated in water bath for 60 minutes before testing. Liposomes of 0.5 mg/mL 1:1 DMPC:DMPG and DOPS:DOPC were also prepared and used as positive controls as they are known to bind the proteins of interest. MBP, P0ct and P2wt were prepared with a concentration of 0.5 mg/mL in same buffer. MBP, P2wt or P0ct was mixed with NPs, to a total volume resulting in a protein concentration of 0.2 mg/mL. The samples were incubated for approximately 15 minutes in ambient temperatures before centrifugation (15 min, 21ºC at 20817 G). Samples were collected from supernatant before and after centrifugation and the pellet (dissolved in 1% SDS) and analysed with SDS-PAGE.

3.5.1.3 Concentration dependency of P0ct

To investigate the concentration dependency of P0ct to liposomes of DMPC:DMPG and DOPC:DOPS, 0.5 mg/mL P0ct was mixed with 0.5 mg/mL liposomes in different protein to lipid ratios (P/L ratios). The different ratios were 1:0.5, 1:1, 1:2, 1:3, 1:4, 1:5 and 1:6. Proteins were mixed with liposomes to a final concentration of 0.2 mg/mL of P0ct. The samples were incubated for approximately 15 min in ambient temperatures before centrifugation (15 min, 21 ºC at 20817 G). Samples were collected from supernatant before and after centrifugation and the pellet (dissolved in 1% SDS) and analysed with SDS-PAGE.

3.5.2 Turbidimetry

To measure differences in turbidity between varying ratios of SUV liposomes and bicelles, different ratios of DMPC:DMPG (1:0, 9:1, 4:1 and 1:1) SUV liposomes, sonicated (SUV) and unsonicated bicelles were prepared. 5 mM bicelles and 0.5 mM SUV liposomes were mixed with 0.5 mg/mL protein (MBP, P2wt and P0ct) in a Greiner 96-well plate flat transparent right before measuring. The temperature was set to 30°C with 30 kinetic cycles with 1 min interval time measuring wavelength at 450 nm and 660 nm. Total kinetic run time was 29 min.

To check for protein concentration variation, different concentrations of protein (MBP, P2wt and P0ct) were mixed with unsonicated bicelles SUV bicelles or SUV liposomes (DMPC:DMPG (1:1)), 5 mM and 0.5 mM respectively. Total volume in each well was 100 µL, and the proteins were diluted with

20 mM HEPES pH 7.5, 150 mM NaCl to the following concentrations: 1.0 µM, 2.5 µM, 5 µM, 7.5 µM and 10 µM. The temperature was set to 30°C and the wavelength to 450 nm and 660 nm. 15 kinetic cycles were done every 1-min. A VersaMax microplate reader (Molecular Devices) was used to measure vesicle aggregation using a Greiner 96-well flat transparent plate. Data was processed using Microsoft Excel and a blank was subtracted from the data. The measurements were done using a Tecan Spark multimode microplate reader.

3.5.3 Ultraviolet-visible spectrophotometry scan (UV-Vis scan)

To see if there was a shift in the optical properties of the coated gold nanoparticles (AuNPs), a UV-VIS scan was done with approximately 1.0 mg/mL uncoated AuNPs and coated AuNPs (modified protocol from (1)). Liposomes (DMPC:DMPG 1:1) were used as a control. 100 µL of each was pipetted onto a Grainer 96-well plate flat transparent in duplicate and the wavelength was measured between 300-900 nm. Wavelength step size was 2 nm, with number of flashes of 25 at room temperature. The lipid measurement was subtracted and the data was normalized to either peak maxima or 300 nm using Microsoft Excel. The measurements were done using a Tecan Spark multimode microplate reader.

3.5.4 Small-angle X-ray diffraction (SAXD)

To examine any repetitive structures in turbid samples, 2 µM, 10 µM and 20 µM protein (P2wt, P2 F57A, MBP and P0ct) were mixed with different concentrations of bicelles and liposomes (DMPC:DMPG 1:1) with concentrations of 1 mM, 2 mM and 3 mM in a HBS buffer (20 mM HEPES and 150 mM NaCl). Samples were prepared at ambient temperature right before measurements and measured at 25°C. The synchrotron SAXD data were collected at PETRA III storage ring, DESY, Hamburg, Germany on beamline P12. Data were analysed using the ATSAS program package (152), GraphPad Prism7 and Microsoft ExCel.

To calculate the mean real-space repeat distance, d, this equation was used:

$$1)\quad d = \frac{2\pi}{s}$$

Where s is the position of the peak of momentum transfer:

$$2)\quad s = \frac{4\pi \sin(\theta)}{\lambda}$$

s was found by zooming in on each individual peak from the diffraction spectra of the different samples. The value from each peak maxima was used as s. Repeat distance was then calculated by plotting the value of s into equation 1.

3.5.5 Transmission electron microscopy (TEM)

3.5.5.1 TEM imaging of 80 nm gold nanoparticles

4 μL of each sample was placed on a glow-discharged carbon coated copper grid and was left to incubate for 1 minutes before excess solution was removed. Samples were left to air-dry before imaging. No stain was needed, but the newly coated AuNPs were tested with and without 2% uranyl acetate staining for 2x12 seconds to check for any differences. TEM imaging was preformed using a Jeol JEM-1230 (MedWOW) instrument.

3.5.5.2 TEM imaging of protein with bicelles and liposomes

0.5 mg/mL protein (P2, MBP or P0ct) was mixed with 0.5 mg/mL bicelles or liposomes (DMPC:DMPG (1:1)) and incubated for 1 h at room temperature. 4 μL samples were then pipetted onto glow-discharged carbon-coated copper grids before incubating for 1 min. Excess solution was removed with filter paper (Whatman) before the samples were washed with 4 drops of Milli-Q water. Samples were stained with two drops of 2% uranyl acetate for 12 s in each drop and air-dried. For the AuNPs 4 μL of solution were pipetted onto same type of grids and left to incubate for 1 min before excess solution was removed. The samples were left to air-dry. TEM imaging was preformed using a Jeol JEM-1230 (MedWOW) instrument.

3.5.6 Synchrotron radiation circular dichroism spectroscopy (SCRD)

P2wt were dialyzed over night to Milli-Q from buffer (20 mM HEPES pH 7.5, 150 mM NaCl) using Slide-A-Lyser Mini Dialysis 3.5K MWCO (Thermo Scientific), with change of Milli-Q at least twice. Bicelles and liposomes were prepared with the ratios of DMPC:DMPG 1:0, 9:1, 4:1 and 1:1 in Milli-Q. 0.4 mg/mL P2wt were then mixed with different ratios of 5 mM bicelles and 1:100 protein to lipids ratio for the vesicles (approximately 2.65 mM vesicles) right before measurement. Spectra were recorded at 30°C from 170 to 280 nm with a cuvette pathlenght of 100 μm. The cuvette used was a closed cylindrical cell (Suprasil, Hellma Analytics). CD units were converted to Δε ($M^{-1}cm^{-1}$)) after baseline subtraction.

$$\Delta\varepsilon = \theta \times \frac{(0.1 \times \mathrm{MRW})}{(\mathrm{P} \times \mathrm{CONC}) \times 3298}$$

Where MRW = Mean residue molecular weight (atomic mass units/daltons), P = cuvette path length and CONC = protein concentration (mg/mL).

SCRD measurements of P2wt with bicelles or liposomes were measured and processes via collaboration at CD1 beamline, ASTRID storage ring, Institute for storage ring facilities in Aarhus (ISA), Aarhus, Denmark.

4 Results

The results are divided into three main parts. First, all myelin proteins were expressed and purified for characterization and to investigate interactions between the proteins with lipids, bicelles and nanoparticles, using methods stated above in paragraph 3 Methods and materials. Each protein is purified differently so the results from each individual expression and purification are given in the sections below, 4.1.1, 4.1.2 and 4.1.3 respectively. Second, the protein-nanoparticle binding are studied in 4.2 and 4.3, before results from protein-membrane interactions is displayed in 4.4-4.8.

4.1 Protein expression and purification

4.1.1 Myelin basic protein

With the use of the chosen *E. coli* expression system, MBP, was easily expressed and harvested over two days. Optical density (OD) was checked regularly to induce expression of MBP by adding IPTG when OD_{600} reached 0.3. After lysis the solution was subjected to two Ni-NTA purifications with different dialysis steps and TEV protease digestion to remove the cleaved his_6-tags. From the two Ni-NTA purifications, and the overnight TEV protease digestion, it becomes clear that the cleaved protein (Figure 6 sample P, indicated with an arrow) contains mainly MBP and degradation products. Only from these two purification steps are the protein relatively pure.

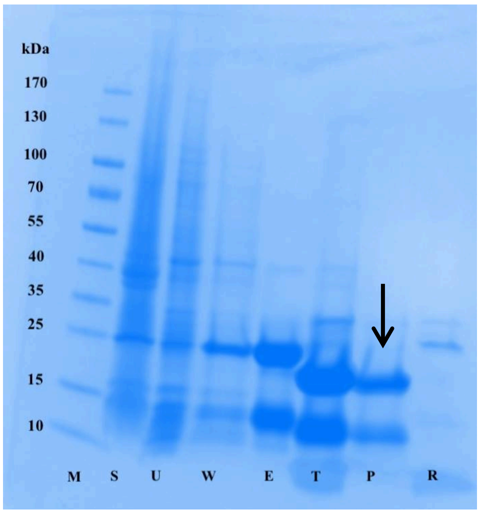

Figure 6: SDS-PAGE analysis of the first and second Ni-NTA affinity chromatography of MBP purification. The figure shows SDS-PAGE samples from both Ni-NTA purification and the TEV protease digestion, to get a pure MBP protein without his_6-tags.Sample P (indicated with an arrow) was further subjected to SEC. Sample legend: M; marker, S; soluble fraction (before Ni-NTA), U; unbound fraction, W; wash fraction and E; elution fraction, all from 1st Ni-NTA, T; TEV protease treated elution fraction, P; cleaved protein and R; remaining fraction, both from the 2nd Ni-NTA. The known molecular weight (kDa) of the marker is specified in the figure.

To get a pure protein without degradation products, size exclusion chromatography (SEC) was performed. A peak in the chromatogram was expected between 10-20 mL, as seen in Figure 7 A. 250 µL fractions were collected around this peak and were checked on SDS-PAGE for purity before measuring concentrations with a NanoDrop 2000 spectrophotometer. Most of the fractions, as viewed in Figure 7 B), were very pure and could be pooled and concentrated down to get some aliquots with high concentration of MBP. The 2-3 last fractions were frozen as is because of the impurities in the solution and second SEC was done on these fractions before usage. The bands in Figure 7 B displays a pure protein that corresponds well to the 18.5 kDa isoform of mouse MBP. The yield and concentration of the combined fractions is listed in Table 2.

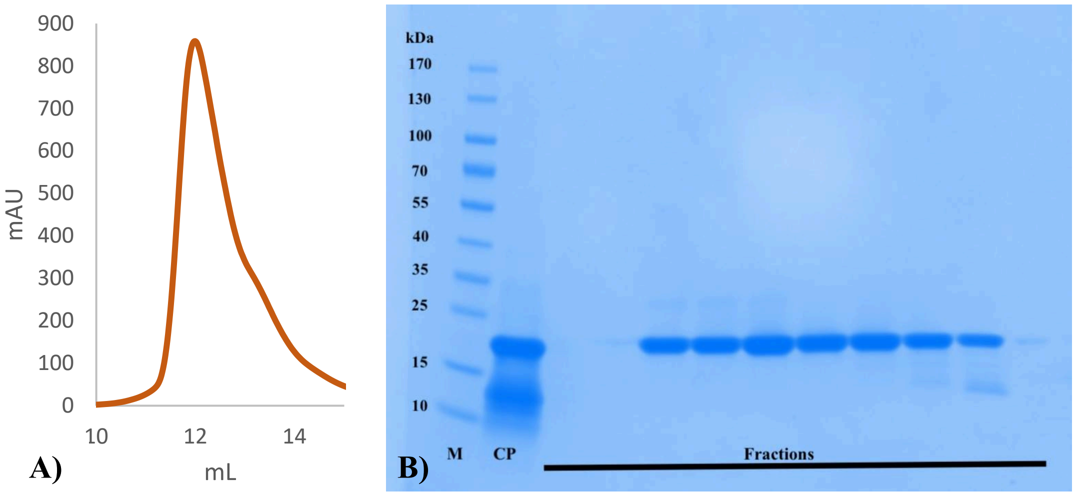

Figure 7: A) Size exclusion chromatogram of MBP. B) SDS-PAGE analysis of the collected fractions. Typical chromatogram from purification of MBP, where the peak appears at 10-15 mL as expected. Fractions collected from SEC appeared at the SDS-PAGE gel with only one ban indicated a pure protein. 250 µL fractions were collected by using a Superdex 75 10/300 GL column (GE Healthcare) with a 500 µL loop. B) Fractions collected were checked for purity and concentration by using SDS-PAGE and NanoDrop 2000 spectrophotometer. The 250 µL fractions corresponding to the SEC peak were checked on SDS-PAGE for purity. Sample legend: M; marker, CP; concentrated protein (before running SEC), Fractions; the fractions corresponding to the peak around 10-15 mL.The known molecular weight (kDa) of the marker is specified in the figure

4.1.2 P0ct

P0ct was expressed and purified several times and each time the protein expressed well in the E. coli expression system. The protein remained soluble after lysis and could be purified with Ni-NTA chromatography. From the Ni-NTA purification the elution fraction (sample E in Figure 8) contained the protein of interest and was subjected to further purification. Overnight dialysis with added TEV protease was done to cleave of the His-MaBP tag before the same fraction was exposed to amylose-resin affinity chromatography to remove the digested His-MaBP, which can be seen in Figure 8 sample P, where three clear bands appear on the SDS-PAGE, which are the His-MaBP tag and P0ct. The 55 kDa band in sample P is uncleaved MaBP-P0ct, while 40 kDa is the His-MaBP tag and 10 kDa is the wanted P0ct (indicated by an arrow in Figure 8). Figure 8 clearly shows that the protein of interest becomes more and more pure with the Ni-NTA and amylose-resin affinity chromatography.

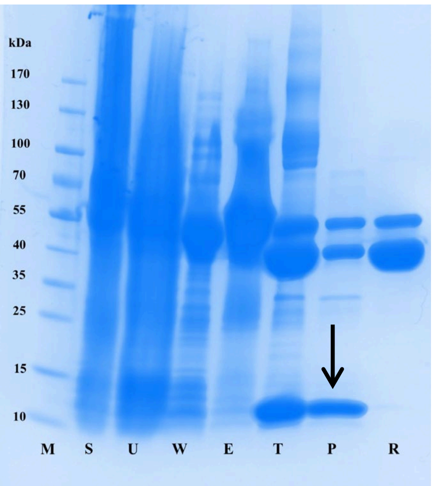

Figure 8: SDS-PAGE analysis from P0ct Ni-NTA chromatography, TEV proteolysis and amylose-resin purification. SDS-PAGE analysis of the first purification steps for P0ct purification. The figure show samples from before and after Ni-NTA purification, TEV protease treatment and after amylose-resin purification to yield P0ct without His_6- and MaBP tag. Sample legend: M; marker, S; soluble fraction (before Ni-NTA), U; unbound fraction (from Ni-NTA), W; wash fraction (from Ni-NTA), E; elution fraction (from Ni-NTA), T; TEV protease treated elution fraction (overnight dialysis), P; cleaved protein (unbound and washing fractions from amylose-resin purification) and R; remaining fraction (elution fraction from amylose-resin purification). The known molecular weight (kDa) of the marker is specified in the figure.

1 mL fractions were collected at 80-100 mL in SEC, where the peak in the chromatogram is expected. As seen in Figure 9 a peak appeared at 85-95 mL. Fractions from the SEC were checked on SDS-PAGE for purity (Figure 9 B) and the concentration was measured with NanoDrop 2000 spectrophotometer. All fractions checked on SDS-PAGE revealed a pure protein without any impurities. The concentrations were determined using known extinction coefficient (ProtParam), see Table 2. P0ct is reasonable easy to express and purify, with good yields every time.

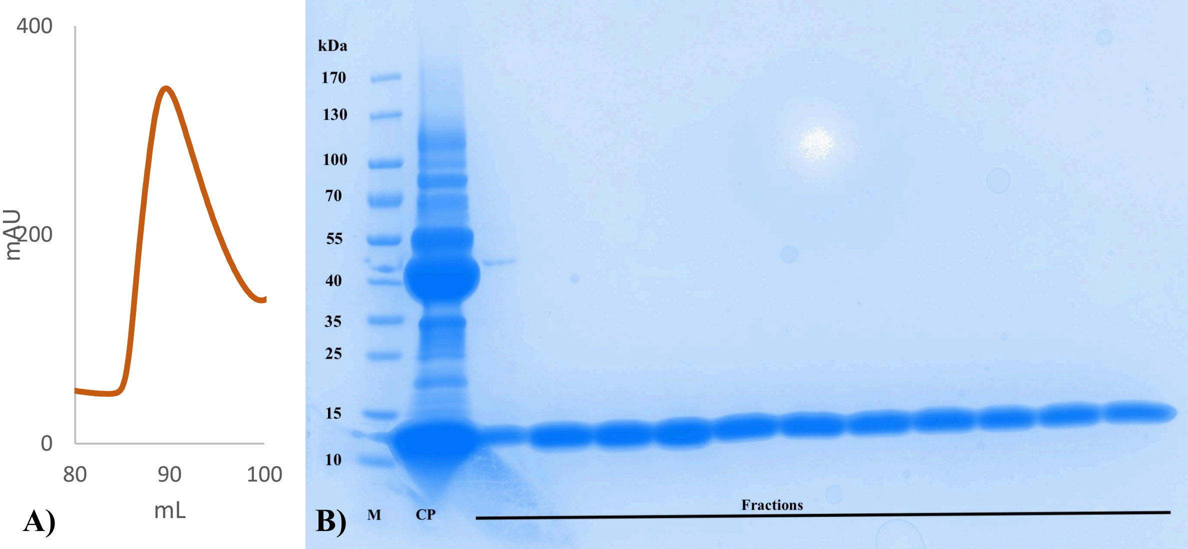

Figure 9: A) Size exclusion chromatogram of P0ct. B) SDS-PAGE analysis of the collected fractions from SEC. A) Characteristic chromatogram from the purification of P0ct. A peak in the chromatogram is expected at around 80-120 mL so 1 mL fractions were collected from around 85-95 mL and checked for purity on SDS-PAGE before concentration was measured on NanoDrop 200 spectrophotometer. SEC was completed with a Hiload Superdex 75 16/60 (GE healthcare) column and a 2 mL loop. B) Fractions of p0ct collected from the size exclusion chromatography were checked on SDS-PAGE for purity. Sample legend: M; marker, CP; concentrated protein and Fractions collected from the SEC. The known molecular weight (kDa) of the marker is specified in the figure.

4.1.3 P2wt and P2 F57A

Expression of P2wt and the mutant F57A is done the same way using different strains of (*E. coli* Rosetta(DE3)) and was expressed in auto induction media over 72 hours, which means that there is no need for measuring of optical density or adding IPTG to induce expression. The purification process after lysis consisted of two Ni-NTA affinity chromatographs with dialysis and TEV protease digestion overnight. P2wt is a protein with a molecular weight of 14.9 kDa, and Figure 10 shows that a clear band at around 15 kDa does not appear until the overnight TEV protease digestion have happened (Figure 10 B samples T). Fractions P1 and P2 in same figure, was protein samples collected after the 2nd Ni-NTA affinity chromatography (indicated with arrows), which was further concentrated before SEC to achieve high purity.

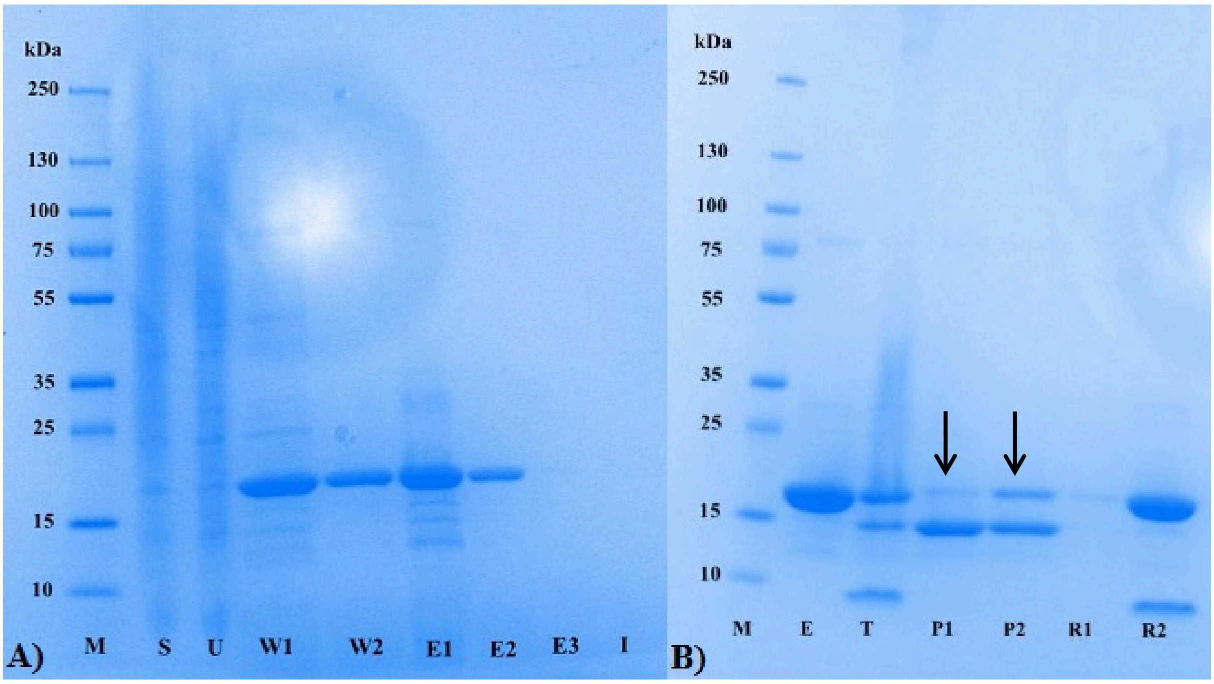

Figure 10: SDS-PAGE analysis of A) 1st and B) 2nd Ni-NTA affinity chromatography of P2wt. The figure shows samples monitoring the purification of P2wt during the 1st and 2nd Ni-NTA purifications with TEV protease digestion overnight and in between the chromatographs. The His-tag is cleaved of the protein with overnight TEV protease digestion (sample T) and fraction is purified with a 2nd Ni-NTA where sample P1-P1 contains the P2wt protein. Sample legend: A) 1st Ni-NTA: M; marker, S; soluble fraction (before 1st Ni-NTA), U; Unbound fraction, W1-W2; wash fractions, E1-E3; elution fractions and I; Imidazole (1 M) fraction. B) 2nd Ni-NTA: M; Marker, E; elution fraction (from 1st Ni-NTA with added TEV protease), T; TEV protease treated elution fraction (overnight dialysis), P1-P2; cleaved protein (unbound and washing fractions) and R1-R2; remaining protein (elution fractions). The known molecular weight (kDa) of the marker is specified in the figure.

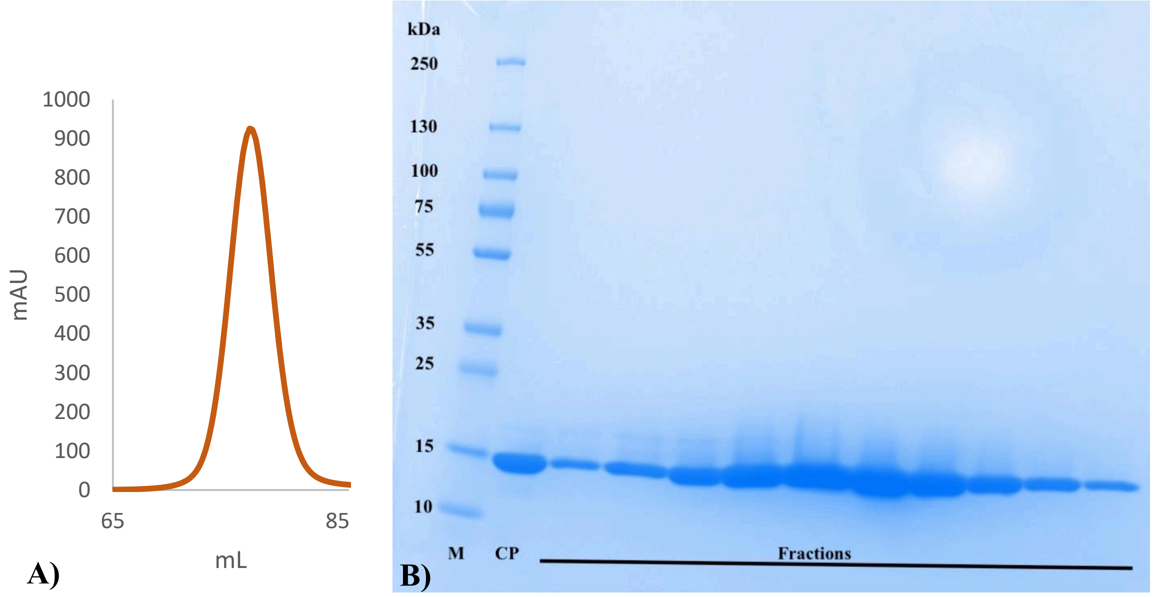

Figure 11: A) Size exclusion chromatogram of P2wt. B) SDS-PAGE analysis of the fractions collected from SEC. A) Characteristic chromatogram from the purification of P2wt. A peak in the chromatogram was expected at around 60-80 mL. 1 mL fractions were collected from around 70-85 mL and were checked for purity on SDS-PAGE before concentration was measured on NanoDrop 200 spectrophotometer. SEC was completed with a Hiload Superdex 75 16/60 (GE healthcare) column and a 1 mL loop. SEC was done with a BioRad DuoFlow system. B) The fractions collected at 70-85 mL during SEC were checked on SDS-PAGE for purity before measuring concentration with NanoDrop 2000 spectrophotometer. Sample legend: M; marker, CP; concentrated protein; Fractions; fractions collected during SEC. The known molecular weight (kDa) of the marker is specified in the figure.

The SDS-PAGE analysis from running SEC (Figure 11 B) revealed high purity of the protein with right molecular weight at around 15 kDa. The concentration of 3.42 mg/mL was relatively good. Concentration of purified protein were measured with NanoDrop 2000 spectrophotometer and calculated with known extinction coefficients (ProtParam). Yield, concentration and extinction coefficients are listed in Table 2.

The mutant P2 F57A was not purified during this master project but during the course BMED325 cellular biochemistry and nanobiochemistry. The yield, concentration, extinction coefficients and analysis during the purification process are listed in Appendix 8.1. In short; the concentration of P2 F57A mutant was 3.29 mg/mL corresponding to a 221 µM, which is a good yield for the P2 mutant. Both proteins are the easiest to express and purify of the proteins used in this study, and are known to give good yields. The purity of the proteins is high and the purification process is straightforward.

Table 2: Protein yields for the proteins MBP, P2wt and P0ct. All proteins were expressed in different strains of *E. coli* and purified using Ni-NTA affinity chromatography and size exclusion chromatography (SEC), with some variation in purification steps. Concentration and yield of every protein was calculated using NanoDrop 2000 spectrophotometer and extinction coefficients found on ProtParam. The yields of the proteins are shown together with their known extinction coefficients and molecular weights.

	Yield (mg)	**Concentration (µM)**	**Abs 0.1 % (AU)**	**ε ($M^{-1}cm^{-1}$)**	**Molecular weight (MW) (Da)**
P0ct	2.02	253.4	1.061	8480	7990.35
MBP	1.01	60	0.698	12950	18544.70
P2wt	3.42	229	0.934	13908	14966.44

4.2 Fe_3O_4 and SiO_2 nanoparticles

4.2.1 No binding of protein to Fe_3O_4 and SiO_2 nanoparticles

Fe_3O_4 with size of 10 nm was first tested for protein binding, which include Fe_3O_4@ODS, Fe_3O_4@ODS-DPPC and Fe_3O_4@ODS-DMPA. Samples were taken from samples containing MBP and P2wt after 15 minutes of incubation to confirm protein content in each sample. As seen in Figure 12, a strong band was visible in each individual sample which indicates a protein content of either MBP at around 18 kDa or P2wt at around 15 kDa that corresponds to known molecular weight of each protein.

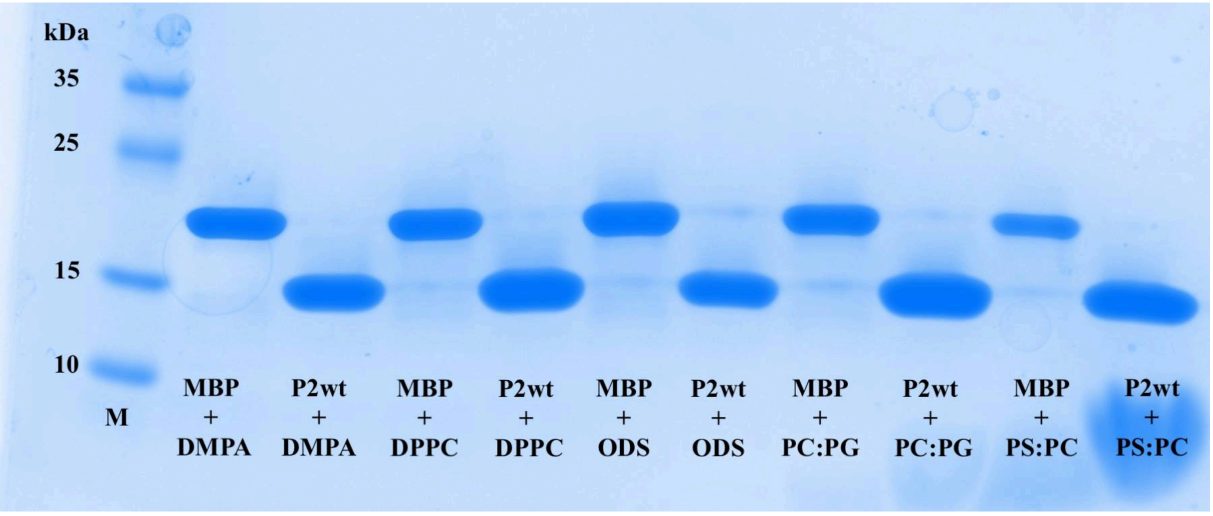

Figure 12: SDS-PAGE analysis of MBP and P2wt with Fe_3O_4 coated nanoparticles (10 nm) and liposomes. 20 µL of 0.5 mg/mL protein were mixed with 30 µL of either 2 mg/mL nanoparticles or 0.5 mg/mL liposomes. The liposomes (DMPC:DMPG and DOPS:DOPC (1:1)were used as positive controls). After 15 minutes of incubation at room temperature samples were taken to confirm protein content. Sample legend: M; marker, MBP + DMPA (DMPA = Fe_3O_4@ODS-DMPA), P2wt + DMPA (DMPA = Fe_3O_4@ODS-DMPA), MBP + DPPC (DPPC = Fe_3O_4@ODS-DPPC), P2wt + DPPC (DPPC = Fe_3O_4@ODS-DPPC), MBP + ODS (ODS = Fe_3O_4@ODS), P2wt + ODS (ODS = Fe_3O_4@ODS), MBP + PC:PG (PC:PG = DMPC:DMPG), P2wt + PC:PG (PC:PG = DMPC:DMPG), MBP + PS:PC (PS:PC = DOPS:DOPC) and P2wt + PS:PC (PS:PC = DOPS:DOPC). The known molecular weight (kDa) of the marker is specified in the figure.

After incubating for 15 minutes, the samples were centrifuged to separate a supernatant and pellet. The evolved pellets were dissolved in 1% SDS before SDS-samples were made.

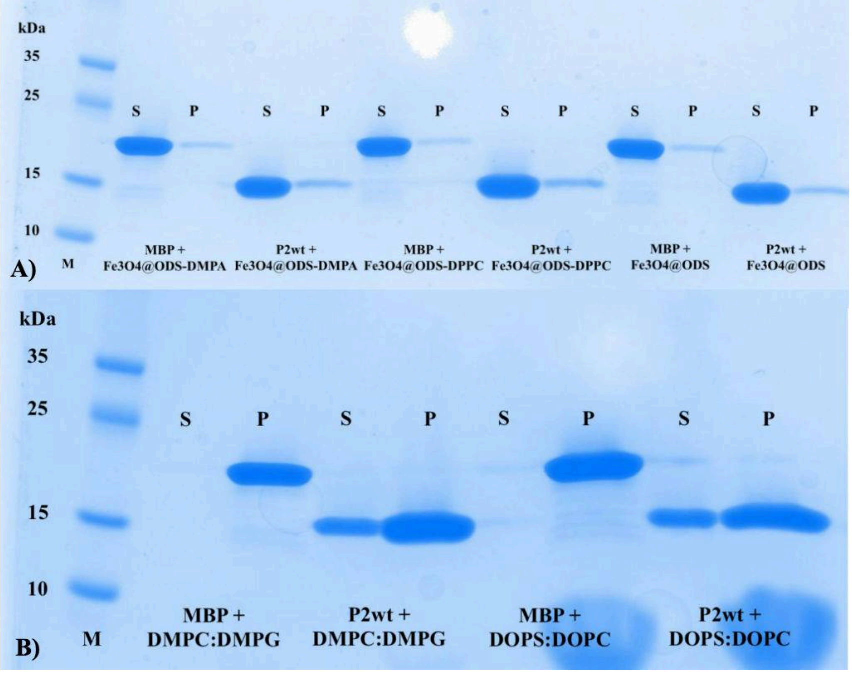

Figure 13: Co-sedimentation analysis of MBP or P2wt A) with Fe_3O_4 nanoparticles (10 nm) B) and liposomes (1:1 ratio). SDS-PAGE analysis of supernatant and pellet of each sample. The weak bands in the nanoparticle pellets (A) is probably due to small amount of supernatant. Sample legend: **A)** M; marker, S; supernatant, P; pellet, MBP + Fe_3O_4@ODS-DMPA, P2wt + Fe_3O_4@ODS-DMPA, MBP + Fe_3O_4@ODS-DPPC, P2wt + Fe_3O_4@ODS-DPPC, MBP + Fe_3O_4@ODS, P2wt + Fe_3O_4@ODS. **B)** M; marker, S; supernatant, P; pellet, MBP + DMPC:DMPG, P2wt + DMPC:DMPG, MBP + DOPS:DOPC and P2wt DOPS:DOPC. The known molecular weight (kDa) of the marker is specified in the figure.

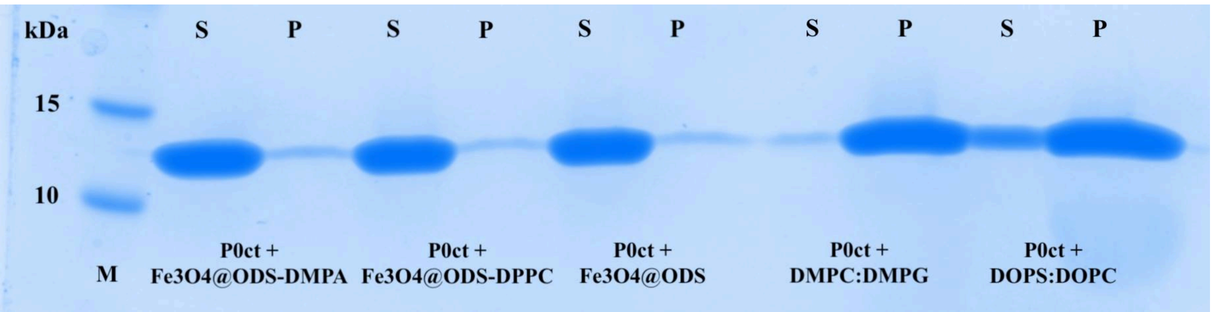

Figure 14: Co-sedimentation analysis of P0ct with Fe_3O_4 nanoparticles (10 nm) and liposomes. SDS-PAGE analysis of supernatant and pellet of each sample. Sample legend: M; marker, S; supernatant, P; pellet, P0ct + Fe_3O_4@ODS-DMPA, P0ct Fe_3O_4@ODS-DPPC, P0ct + Fe_3O_4@ODS, P0ct + DMPC:DMPG and P0ct + DOPS:DOPC. The known molecular weight (kDa) of the marker is specified in the figure.

Co-sedimentation analysis was done with the proteins MBP, P2wt and P0ct. From Figure 13 and Figure 14 the results showed that little or no protein binds to the coated Fe_3O_4 nanoparticles with the size of 10 nm. The positive controls revealed binding as expected as seen for MBP and P2wt in Figure 13 and for P0ct in Figure 14, with strong bands in all pellets.

Fe_3O_4 coated nanoparticles, 150 nm in size, was also tested for protein binding with co-sedimentation assay. Same procedure as above was followed as seen in Figure 15. Same results as with Fe_3O_4 coated NPs with 150 nm size. Little or no binding to the nanoparticles is indicated in A), B) and C). The controls were positive with broad bands in pellets for both types of liposomes.

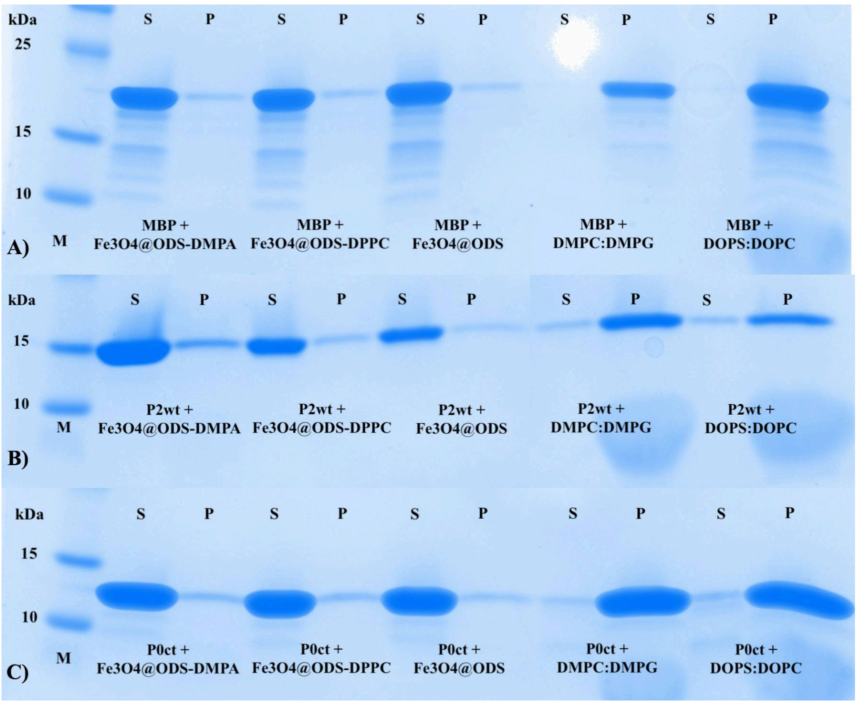

Figure 15: Co-sedimentation analysis of A) MBP, B) P2wt and C) P0ct with Fe_3O_4 nanoparticles (150 nm) and liposomes. Fe_3O_4 coated nanoparticles were mixed with protein before incubating and centrifugation. Samples were taken from both supernatant and pellet before checking protein binding on SDS-PAGE. Sample legend: M: marker, S; supernatant, P; pellet, **A)** MBP + Fe_3O_4@ODS-DMPA, MBP + Fe_3O_4@ODS-DPPC, MBP + Fe_3O_4@ODS, MBP + DMPC:DMPG and MBP + DOPS:DOPC. **B)** P2wt + Fe_3O_4@ODS-DMPA, P2wt + Fe_3O_4@ODS-DPPC, P2wt + Fe_3O_4@ODS, P2wt + DMPC:DMPG and P2wt + DOPS:DOPC. **C)** P0ct + Fe_3O_4@ODS-DMPA, P0ct Fe_3O_4@ODS-DPPC, P0ct + Fe_3O_4@ODS, P0ct + DMPC:DMPG and P0ct + DOPS:DOPC. The known molecular weight (kDa) of the marker is specified in the figure.

Protein binding to silicon dioxide (SiO_2) was similarly tested with same procedure as described and tested with the three proteins MBP, P2wt and P0ct. The results from co-sedimentation analysis are viewed in Figure 16 and weak band can be seen in the pellets, but does not show the strong indication that the positive controls do.

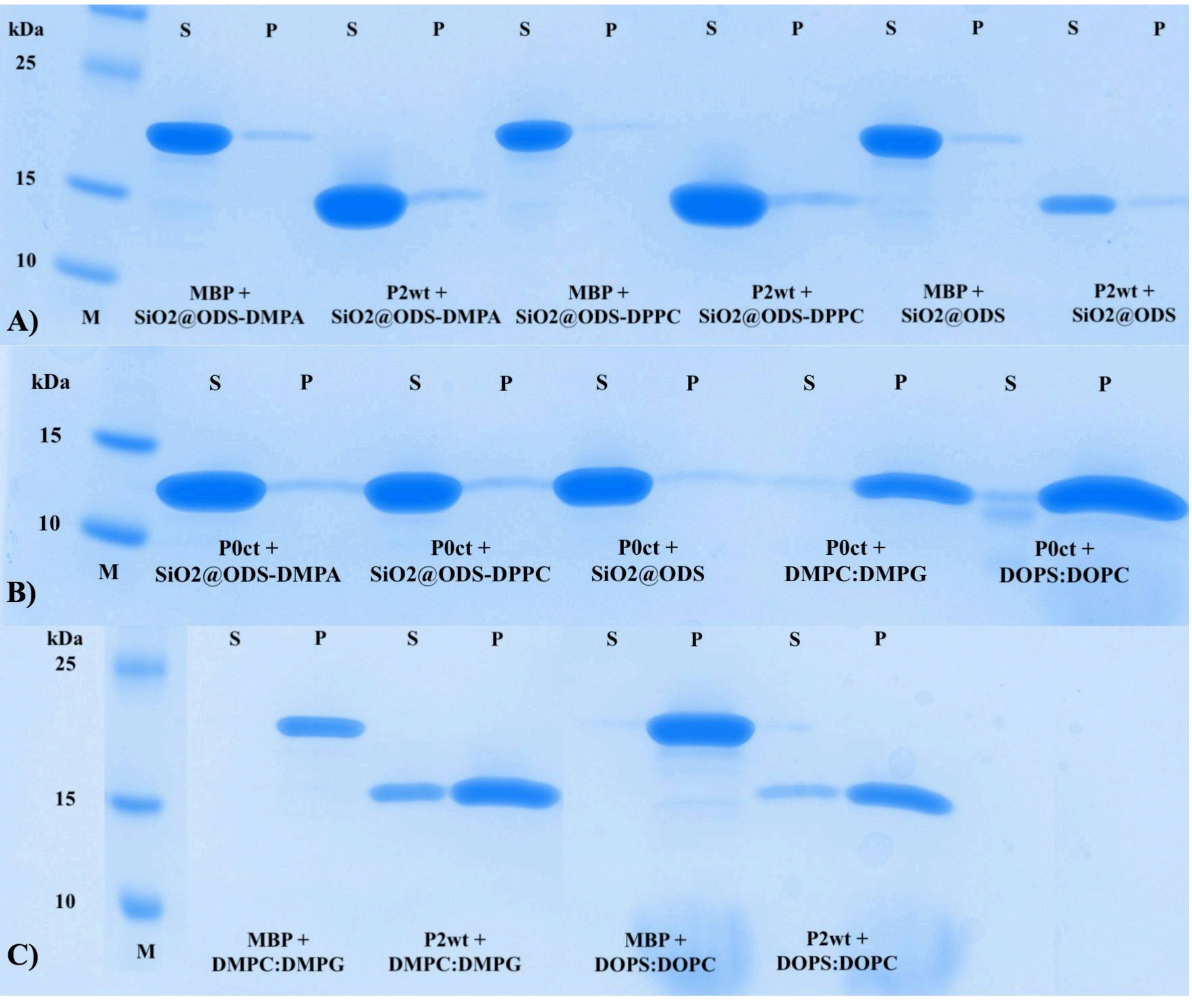

Figure 16: Co-sedimentation analysis of A) MBP and P2wt, B) with P0ct with SiO_2 coated nanoparticles and C) MBP and P2wt with liposomes. Different proteins were mixed with the coated SiO_2 nanoparticles, incubated and centrifuged before samples for SDS-PAGE were collected. 1:1 DMPC:DMPG and DOPS:DOPC were used as positive controls. A) Shows the supernatant and pellet from MBP and P2wt mixed with the NPs, while B) is the analysis of P0ct with same NPs and the controls. C) Positive control for MBP and P2wt. Sample legend: M; marker, S; supernatant, P; pellet, **A)** MBP + SiO_2@ODS-DMPA, P2wt + SiO_2@ODS-DMPA, MBP + SiO_2@ODS-DPPC, P2wt + SiO_2@ODS-DPPC, MBP + SiO_2@ODS, P2wt + SiO_2@ODS, **B)** P0ct + SiO_2@ODS-DMPA, P0ct + SiO_2@ODS-DPPC, P0ct + SiO_2@ODS, P0ct + DMPC:DMPG and P0ct + DOPS:DOPC. **C)** MBP + DMPC:DMPG, P2wt + DMPC:DMPG, MBP + DOPS:DOPC and P2wt + DOPS:DOPC. The known molecular weight (kDa) of the marker is specified in the figure.

SEM images from collaborator Chaozhan Wang (Ph.D. Professor of Chemistry) can be viewed in Appendix 8.2.

4.2.2 Coating of Fe_3O_4@ODS (150 nm)

Since the co-sedimentation analysis of the Fe_3O_4@ODS-DMPA, Fe_3O_4@ODS-DPPC, SiO_2@ODS-DMPA and SiO_2@ODS-DPPC did not confirm any good binding to the proteins, coating of the Fe_3O_4@ODS (150 nm) was done with DMPC:DMPG (1:1) following the procedure explained in Methods and materials 2.4.3 and checked for protein binding with MBP and same principles described in previous paragraph.

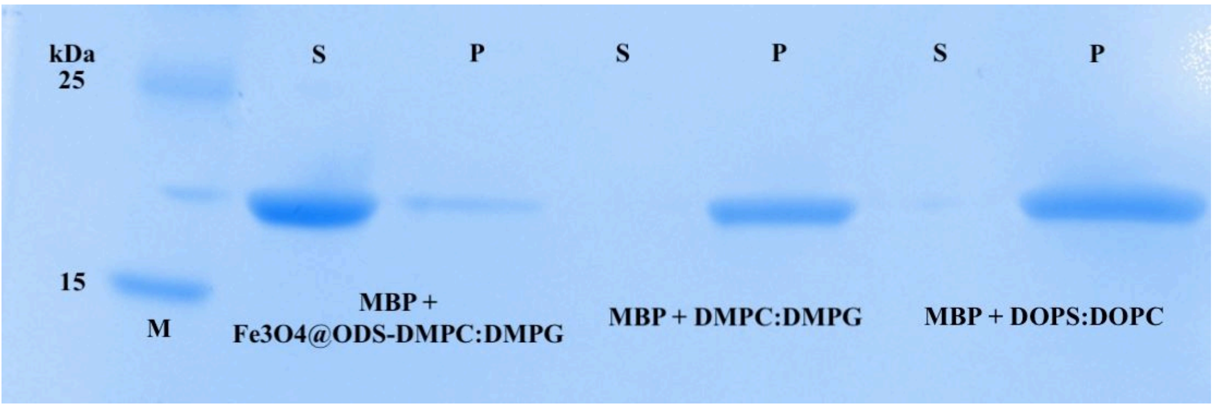

Figure 17: Co-sedimentation assay of Fe_3O_4@ODS coated with 1:1 DMPC:DMPG. MBP were mixed with samples of coated Fe_3O_4@ODS with DMPC:DMPG following the procedure described from collaborator Chaozhan Wang (Ph.D. Professor of Chemistry). SDS-PAGE samples were taken from both supernatant and pellet after incubating for 15 minutes and then centrifuged. DMPC:DMPG and DOPS:DOPC were used as positive controls. The weak band in the nanoparticles pellet was probably due to residues from the supernatant. Sample legend: M; arker, S: supernatant, P; pellet, MBP + Fe_3O_4@ODS-DMPC:DMPG, MBP + DMPC:DMPG and MBP + DOPS:DOPC. The known molecular weight (kDa) of the marker is specified in the figure.

Coating of the Fe_3O_4@ODS with liposomes did not show any progress in protein binding, as viewed in Figure 17. The weak band in the nanoparticle pellet was probably supernatant residues and not binding. No further trials were made with these nanoparticles.

4.3 Gold nanoparticles

4.3.1 Coating of AuNPs indicated binding

Since the nanoparticles from collaborator Chaozhan Wang did not seem to work, 80 nm gold nanoparticles (AuNPs) were ordered from NanoComposix together with 1-octanethiol to try to functionalize them with 1-octanethiol and further coat with DMPC:DMPG (1:1). 3 protocols were tested from different articles; denoted protocol 1-3, respectively (1, 132, 153). Protocol 1 did not work and was not further tried in this project (153).To coat the AuNPs, two protocols were modified and used (1, 132) as described in Methods and materials 2.4.1. Both protocols gave solution with a dark red/purple solution which indicated nanoparticles at around 80 nm. Aggregation and disappearing colour of the protocol 3 (1) coated AuNPs when MBP was added indicated protein binding (Figure 18). Co-sedimentation assay was done to easily check protein binding with MBP with the coated AuNPs. Bare AuNPs and DMPC:DMPG (1:1) were used as negative and positive control, respectively.

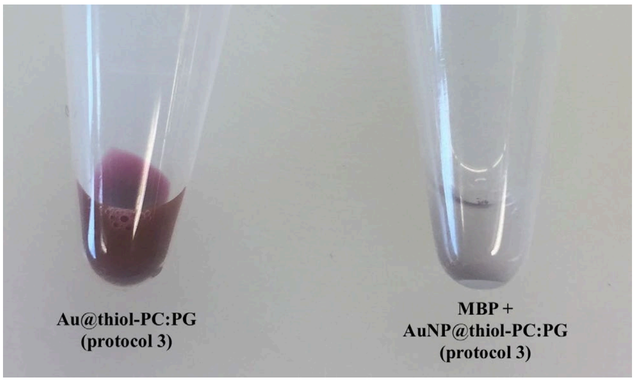

Figure 18: Image of AuNPs coated with 1-octanethiol and DMPC:DMPG (1:1) following protocol 3 (1) without and with added MBP. Coated AuNPs alone have a dark red/purple color which indicates particles at around 80nm. With added MBP the color disappear and the solution turns murky colorless indicating an aggregated state and possible binding of MBP.

Co-sedimentation analysis of the coated AuNPs did not show any absolute binding to either for the coating protocols, but a weak band can be seen in the pellet from coated AuNPs from protocol 2 (151), see Figure 19. The different bands in the supernatants indicated degradation products from the protein. No binding to the uncoated AuNPs which is expected and binding to the DMPC:DMPG signifies that the assay is working.

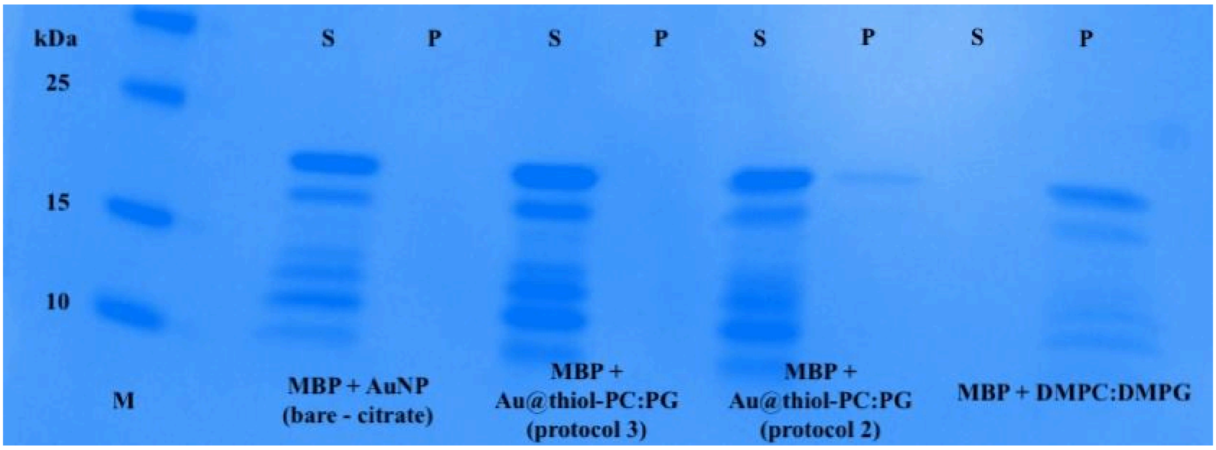

Figure 19: Co-sedimentation assay for AuNPs coated with 1-octanethiol using two different protocols (1, 151). 0.5 mg/mL MBP were mixed with the coated AuNPs to a final concentration of 0.2 mg/mL and incubated for 15 minutes before centrifuging. SDS-PAGE samples were collected from both supernatant and pellet and checked for protein binding. The co-sedimentation assay indicated that MBP did not bind to the coated AuNPs. Sample legend: M; marker, S; supernatant, P; pellet, MBP + AuNP (bare-citrate, uncoated), MBP + AuNP@thiol-PC:PG (AuNPs coated with 1-octanethiol and DMPC:DMPG using protocol 3 (1)), MBP + AuNP@thiol-PC:PG (AuNPs coated with 1-octanethiol and DMPC:DMPG using protocol 2 (151)) and MBP + DMPC:DMPG (positive control) The known molecular weight (kDa) of the marker is specified in the figure. Lower bands in the S fractions are degradation products of MBP.

4.3.2 UV-Vis scan of gold nanoparticles

Since the coated AuNPs (protocol 3, (1)) showed colour difference when MBP was added (Figure 18) indicating protein binding, ultraviolet-visible spectroscopy (UV-vis) was done to investigate any coating of the AuNPs. Duplicates of bare AuNPs, AuNP@thiol-PC:PG and DMPC:DMPG (1:1) was done with a wavelength ranging from 300 nm to 900 nm. No big shift in optical properties was found, but the spectra showed a small shift of the peak maxima for the coated AuNPs. The bare AuNPs had a peak a 544 nm while the coated AuNPs had a peak at 548 nm (Table 3). At the same time, a shoulder is seen at around 360 nm for both coated AuNPs and liposomes DMPC:DMPG (1:1), which is absent in the bare AuNPs (Figure 20). The same shoulder was seen in the raw data (not shown) and in the data normalized to 300 nm (Figure 49 in Appendix 8.3).

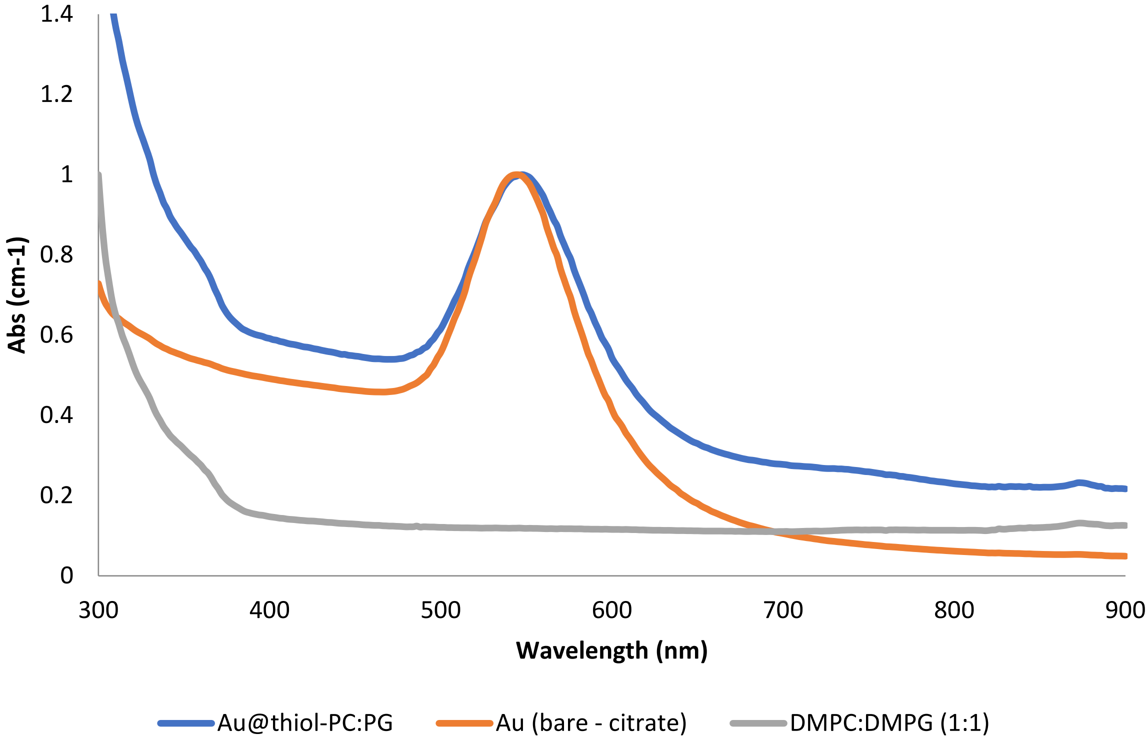

Figure 20: UV-VIS spectra of bare AuNPs and coated AuNP (Au@thiol-PC:PG) normalized to peak maxima. To check a possible coating of the coated AuNPs the UV-VIS spectra were measured with a wavelength range of 300 nm to 900 nm, with step size = 2 and number of flashes was 25. The AuNPs are coated with 1-octanethiol and DMPC:DMPG (1:1) and liposomes with same lipid ratio was used as a control. A shoulder at around 360 nm was seen for the coated AuNPs and liposomes, and a red shift of 4 nm was found between the gold nanoparticles. The data is normalized to peak maxima.

Table 3: Peak maxima from UV-VIS spectra of bare and coated AuNPs,and liposomes. Peak maxima of the different samples seen in Figure 20 given in nanometers.

	Au (bare – citrate)	**Au@thiol-PC:PG**	**DMPC:DMPG (1:1)**
λ_{max} (nm)	544	548	300

4.3.3 TEM images of AuNP

Transmission electron microscopy (TEM) was executed to further confirm any coating of the AuNPs, and to confirm the size ordered from NanoComposix. A new batch of coated AuNP (protocol 3 (1)) was made to see a possible difference between newly made and old coating.

The membrane of the grid to the old coated AuNPs (2 month old) moved too much to get a good image of any coating, but Figure 21 revealed AuNPs on the grids that were clustered together. No identification of the DMPC:DMPG (1:1) coating could be made.

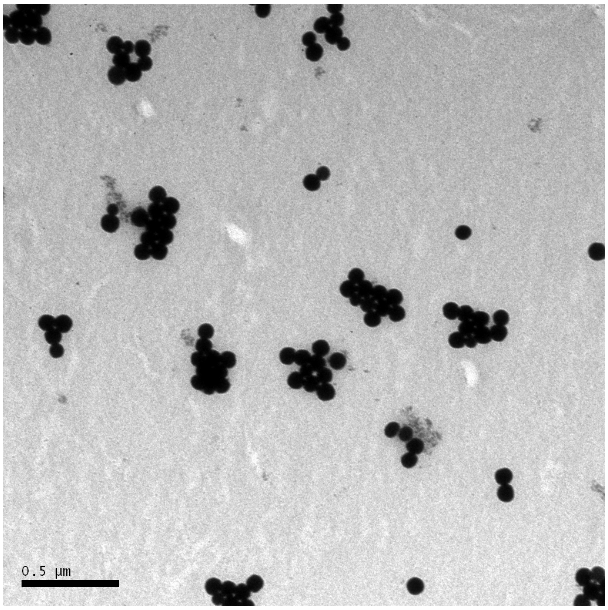

Figure 21: Transmission electron micrograph of AuNPs coated with thiol and DMPC:DMPG (1:1). The solution with coated AuNPs had been in room temperature for 2 month. The thin membrane film was damaged and high resolution images were impossible. TEM imaging was preformed using a Jeol JEM-1230 (MedWOW) instrument at the molecular imaging center (MIC), Department of Biomedicine, University of Bergen.

The newly coated AuNPs (Au@thiol-PC:PG) with thiol and DMPC:DMPG (1:1) was imaged with and without staining, viewed in Figure 22. Left image of the non-stained Au@thiol-PC:PG nanoparticles revealed no coating and they looked the same as the bare AuNPs (Figure 23). The stained sample of the same AuNPs, as viewed in Figure 22 (right), indicated bright rings around numerous particles (indicated by black arrows) which might uncover the wanted coating. The micrographs also implied that the coated AuNPs were more aggregated than the bare ones.

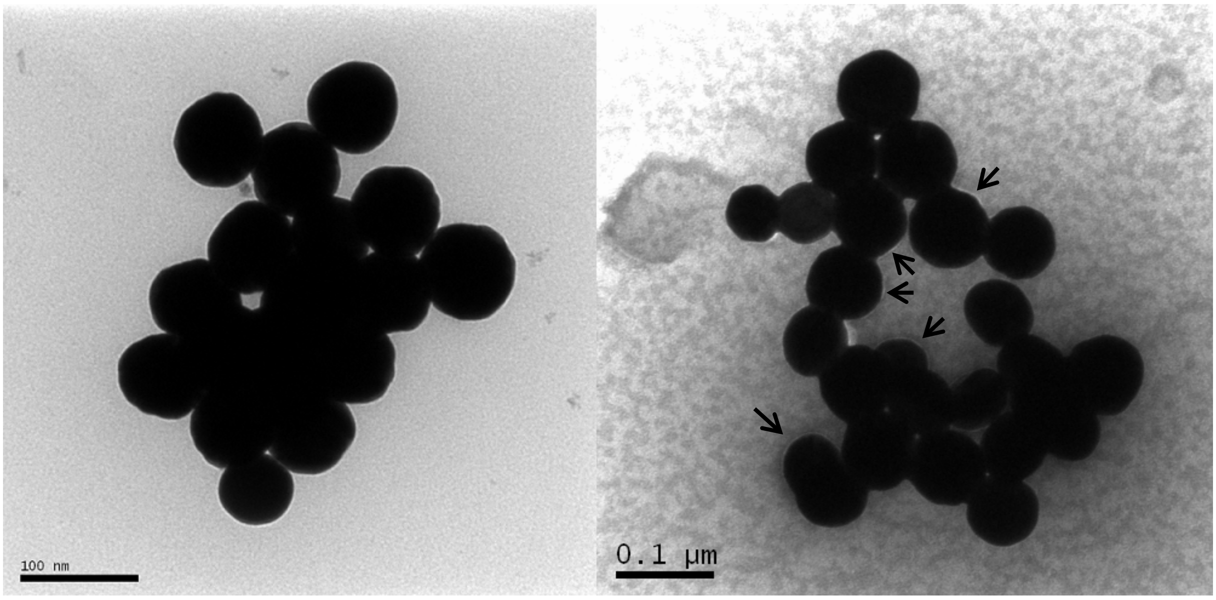

Figure 22: Transmission electron micrograph of coated AuNPs without (left) and with (right) staining. Au@thiol-PC:PG with 2x12 s. staining with 2% uranyl acetate. A few bright circles can be seen around some of the coated AuNPs (right images, indicated with black arrows). The circles might indicate a DMPC:DMPG (1:1) coating around the nanoparticles. TEM imaging was preformed using a Jeol JEM-1230 (MedWOW) instrument at the molecular imaging center (MIC), Department of Biomedicine, University of Bergen.

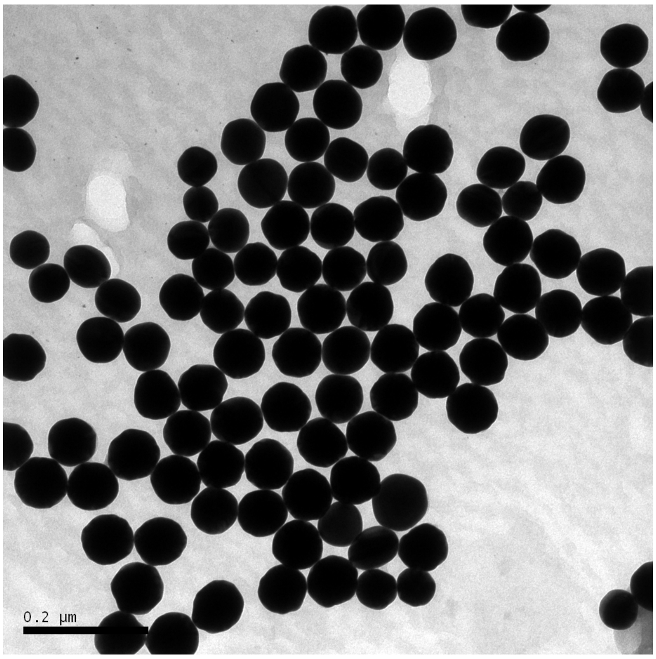

Figure 23: Transmission electron micrograph of bare AuNPs without staining. Micrograph of bare AuNPs were taken to have control for the coated ones and also confirm size and shape that was ordered from NanoComposix. TEM imaging was preformed using a Jeol JEM-1230 (MedWOW) instrument at the molecular imaging center (MIC), Department of Biomedicine, University of Bergen.

From TEM the diameter of one nanoparticle was measured to verify the size distribution given by NanoComposix, diameter of one of the nanoparticles was measured to 75 nm, which corresponds well to the size given from the company. Figure 23 reveals good distribution of the gold nanoparticles with the concentration of 1.09 mg/mL without aggregates.

4.4 Concentration dependency of P0ct

To investigate if binding of P0ct to liposomes are dependent on lipid concentration, different protein to lipid ratios were tested with liposomes of DMPC:DMPG and DOPC:DOPS (1:1) and with constant concentration of P0ct (0.2 mg/mL). Protein to lipid ratios was in the range of 1:0.5 – 1:6. The analysis revealed (Figure 24) that binding of P0ct to liposomes of either DMPC:DMPG or DOPC:DOPS increases with increased P/L ratio to a point where saturation occurs. It also revealed less protein in supernatant for samples containing liposomes of DOPC:DOPS, as seen in Figure 24, comparing A to B. Smaller concentrations of DMPC:DMPG is needed for P0ct binding than for the DOPC:DOPS, which reaches as saturation level later than DMPC:DMPG.

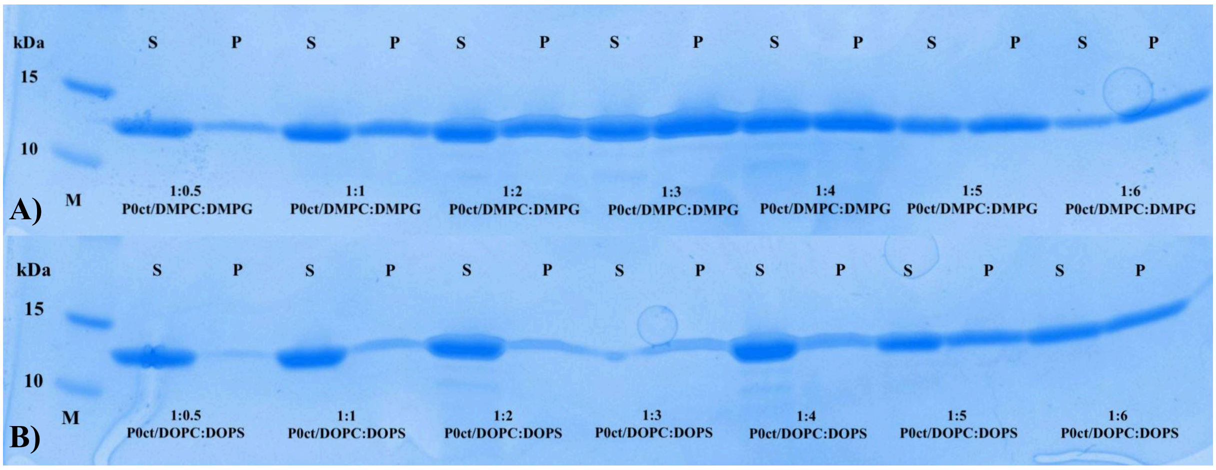

Figure 24: SDS-PAGE analysis of different protein to lipd ratios A) DMPC:DMPG (1:1) and B) DOPC:DOPS (1:1). 20 µL of 0.5 mg/mL of P0ct was mixed with 30 µL of 0.5 mg/mL DMPC:DMPG or DOPS:DOPC in ratios ranging from 1:0.5 to 1:6. A) SDS-PAGE analysis of different P0ct/DMPC:DMPG ratios. Sample legend: M; marker, S; supernatant, P; pellet, 1:0.5 P0ct/DMPC:DMPG, 1:1 P0ct/DMPC:DMPG, 1:2 P0ct/DMPC:DMPG, 1:3 P0ct/DMPC:DMPG, 1:4 P0ct/DMPC:DMPG, 1:5 P0ct/DMPC:DMPG and 1:6 P0ct/DMPC:DMPG. B) SDS-PAGE analysis of different protein to lipid ratios of P0ct/DOPC:DOPS. Sample legend; M; marker, S; supernatant, P; pellet, 1.05 P0ct/DOPC:DOPS, 1:1 P0ct/DOPC:DOPS, 1:2 P0ct/DOPC:DOPS, 1:3 P0ct/DOPC:DOPS, 1:4 P0ct/DOPC:DOPS, 1:5 P0ct/DOPC:DOPS and 1:6 P0ct/DOPC:DOPS. The known molecular weight (kDa) of the marker is specified in the figure.

4.5 Vesicle aggregation

4.5.1 Lipid composition dependent vesicle aggregation

To measure variation in vesicle aggregation between different ratios of liposomes and bicelles combined with varying concentration of protein (MBP, P2wt and P0ct), turbidity assays was conducted. Only the 450 nm measurements are presented here, the 660 nm measurements are listed in Appendix 8.4. By varying the ratios between DMPC:DMPG in both liposomes and bicelles, and keeping protein concentration constants, differences in vesicle aggregation dependent on ratios could be examined. Protein to lipid ratio was 1:1 for the liposomes and 1:10 for the bicelles.

MBP was measured with unsonicated bicelles and liposomes and showed some variance between the different ratios, as seen in Figure 25, with a similarity in flattening out at the end of the 30 min kinetic cycles. With ratio 9:1, Figure 25 A, there was a big jump in absorbance for the bicelles to 0.647 at 6 min before dropping below 0.1, reaching a steady state. MBP binding to ratio 4:1 of DMPC:DMPG bicelles starts with high absorbance at 1.03 before decreasing continuously to 0.2, as viewed in Figure 25 B. For the 1:1 ratio, Figure 25 C, the bicelles kept a more stable absorbance around 0.6. For all ratios the liposome, samples was stable and is relatively straight as seen for the control (1:0) which do not bind to the protein and have a low absorbance at 0.06 (Figure 25 D).

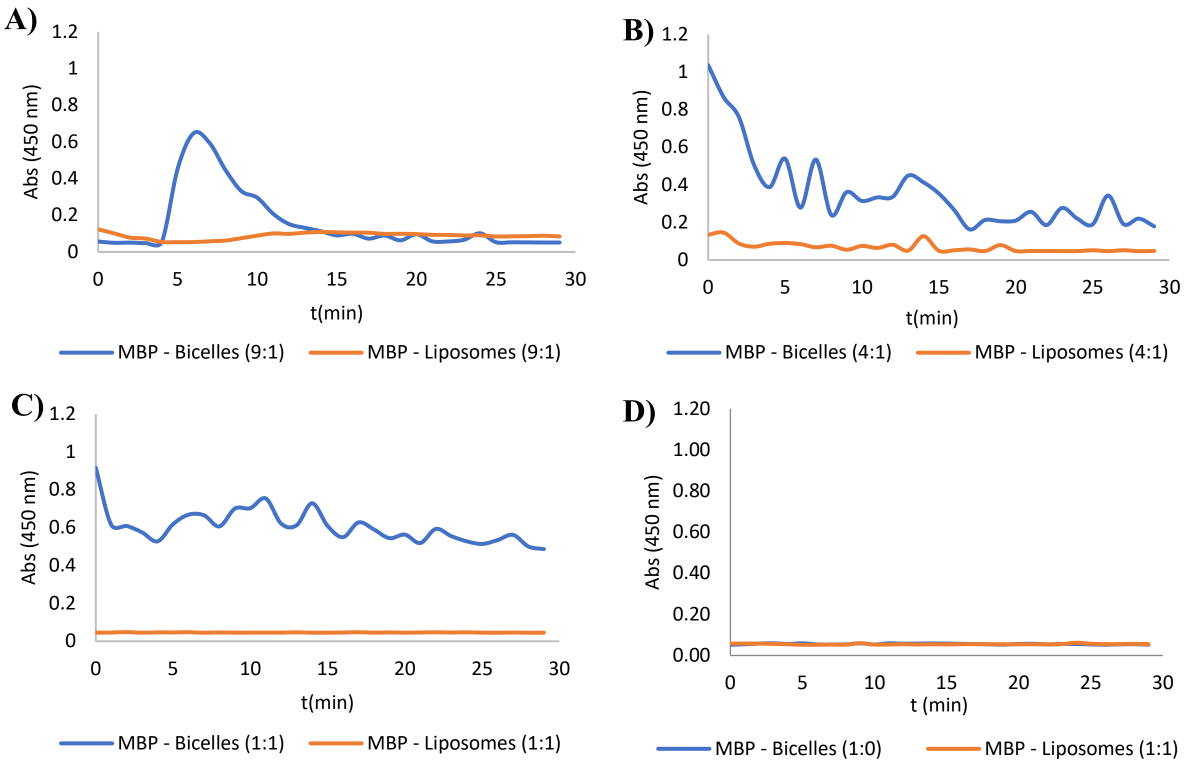

Figure 25: Vesicle aggregation with different ratios of DMPC:DMPG with MBP. Measured absorbance over 30 min with constant concentration of P2wt and different ratios of DMPC:DMPG in liposomes and bicelles. The ratios of DMPC:DMPG in the liposomes and bicelles were 1:0: 1:1: 1.4 and 1:9. A) 9:1 ratio: increased absorbance at 6 min for bicelles which decreased rapidly over the next 5 min. Over time the absorbance decreases more for the 4:1 ratio (B) than for the 1:1 ratio (C). D) 1:0 ratio as negative control. Absorbance measured at wavelength 450 nm at 30 ºC. Protein concentration was held constant at 0.5 mg/mL mixed with 5 mM bicelles and 0.5 mM liposomes. Protein to lipid ratio was 1:1 and 1:10, for liposomes and bicelles respectively.

The turbidity measurements with P2wt investigated the differences between bicelles, SUV bicelles and the liposomes. In ratios 9:1 and 4:1 there was no big difference between the two types of bicelles (Figure 26 A-B) except for a big jump in absorbance for bicelles 9:1 at 1.23 when reaching 9 min. Binding of P2wt to bicelles and SUV bicelles with the ratio 4:1 keeps a higher absorbance over the 30 min than the 9:1 ratio, which might imply that the 4:1 ratio have more stability over time than the 9:1 ratio. 1:1 ratio of bicelles and SUV bicelles is decreasing slowly from 0.49 and 0.58, (Figure 26 C), while the negative control gave increased absorbance to 0.29 for the bicelles mixed with P2wt, as viewed in Figure 26 D, likely an error not aggregates.

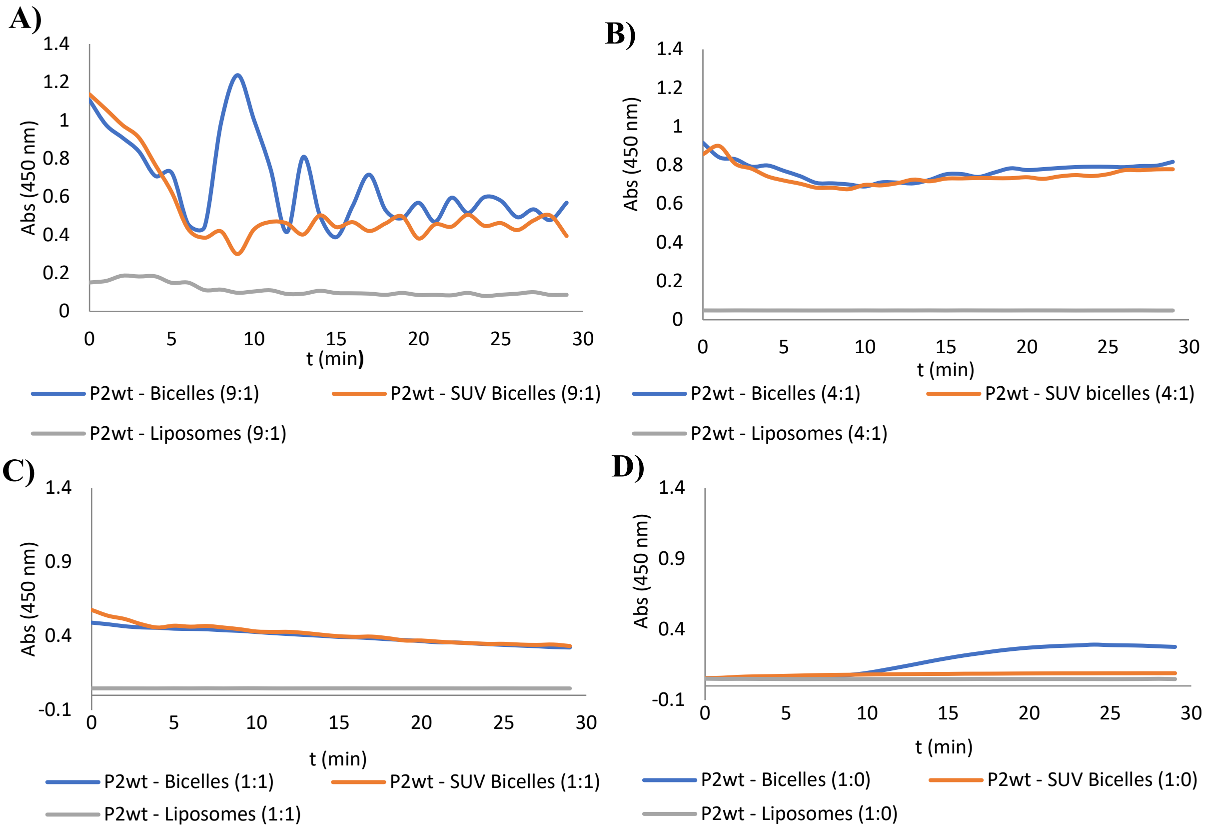

Figure 26: Vesicle aggregation with different ratios of DMPC:DMPG with P2wt. Measurement of absorbance over 30 min with constant concentration of P2wt with bicelles, SUV bicelles and liposomes with different ratios of DMPC:DMPG. The ratios of DMPC:DMPG was 1:0, 1:1, 1:4 and 1:9. A) P2wt induces a delayed aggregation of the 9:1 ratio of lipids, while the 4:1 ratio seems to stabilize quickly (B). C) Steady decrease in absorbance for the 1:1 ratio, C) 1:0 ratio as negative control. Absorbance measured at wavelength 450 nm at 30ºC. Protein concentration was held constant at 0.5 mg/mL mixed with 5 mM bicelles and 0.5 mM liposomes. Protein to lipid ratio was 1:1 and 1:10, for liposomes and bicelles respectively.

The same type of measurements were done with P0ct. Protein binding with the ratio 9:1 of bicelles and SUV bicelles indicated a lower absorbance for both bicelles compared to the liposomes (Figure 27 A) with a small increase for the SUV bicelles reaching stable state, Abs_{450} equal to 1.0 after 15 min. For both ratios 4:1 and 1:1of DMPC:DMPG the absorbance decreases with time and no big difference was seen between the bicelles, as viewed in Figure 27 B-C. With time both bicelles, bound to P0ct, achieved a more permanent absorbance at around 0.5 and under. The negative control, Figure 27 D, displayed an increase in absorbance for the SUV bicelles 1:0, but the absorbance is low and the increase is negligible.

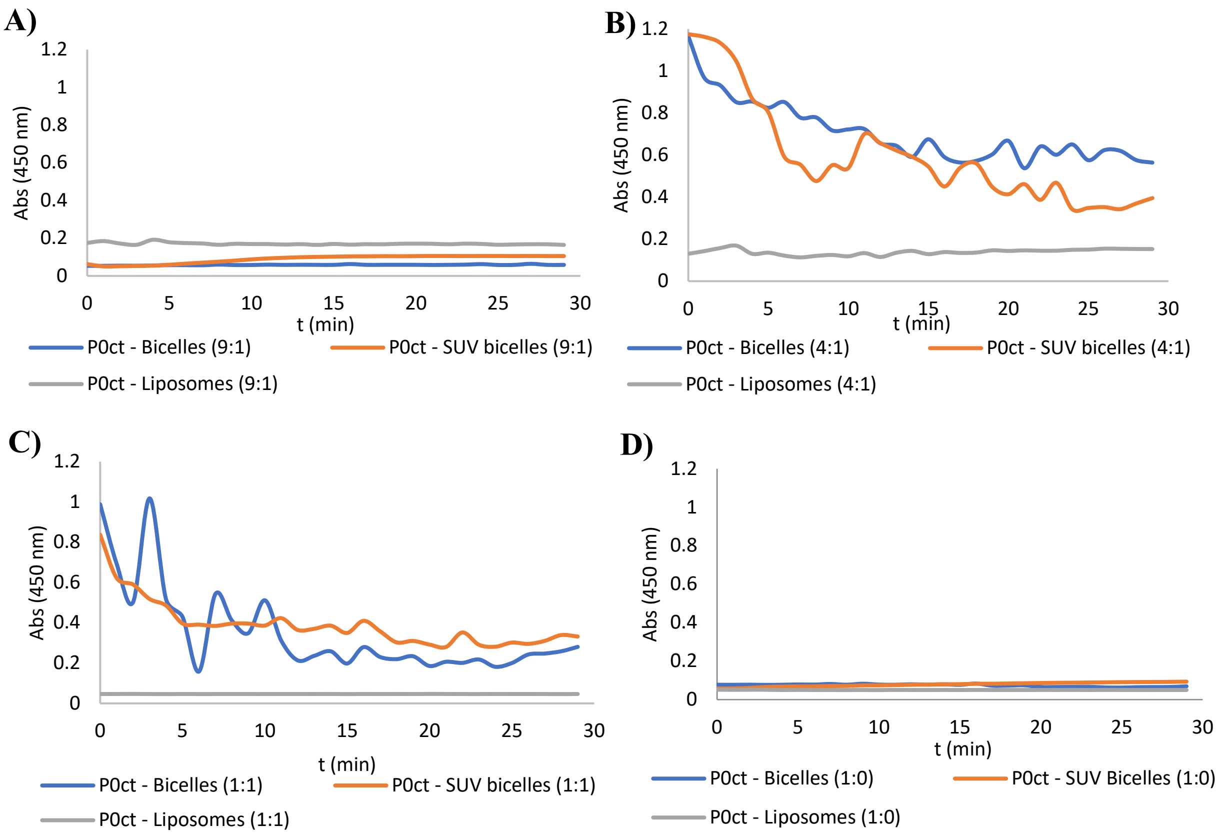

Figure 27: Vesicle aggregation with different ratios of DMPC:DMPG with P0ct. Absorbance measured over 30 minutes with constant concentration of P0ct with different ratios of DMPC:DMPG in bicelles, SUV bicelles and liposomes. The ratio of DMPC:DMPG was 1:0, 1:1, 1:4 and 1:9. A) 9:1 ratio, B) 4:1 ratio, C) 1:1 ratio and D) 1:0 ratio as negative control. Absorbance measured at wavelength 450 nm at 30ºC. Protein concentration was held constant at 0.5 mg/mL mixed with 5 mM bicelles and 0.5 mM liposomes. Protein to lipid ratio was 1:1 and 1:10, for liposomes and bicelles respectivel

4.5.2 Concentration dependent vesicle aggregation

Vesicle aggregation was also tested by keeping concentration of DMPC:DMPG (1:1) bicelles and liposomes constant and by varying the concentration of the protein (MBP, P2wt and P0ct). Concentration of the proteins was ranging from 1.0 - 10 µM. The proteins to lipid ratio for the bicelles were; 1:5000, 1:2000, 1:1000, 1:666 and 1:500 and for the liposomes the protein to lipid ratio was 1:500, 1:200, 1:100, 1:66 and 1:50, from 1.0 to 10 µM respectively.

For every protein, the turbidity assays indicated over all that the 10 µM concentration gave the highest absorbance with 7.5 µM giving the second highest absorbance (Figure 28), except for the measurements with DMPC:DMPG liposomes and P0ct where 2.5 µM having absorbance at 0.11 and decreasing with time (Figure 28 C). Binding of MBP to bicelles gave the highest absorbance at 0.38 5 min into the measurements, with 7.5 µM at 0.14 when reaching 9 min (Figure 28 A). Bicelle aggregates induced by MBP gave a more rapid decrease in absorbance than the liposome aggregates, which had a higher absorbance also for the 5.0 µM concentration of protein. A more steady decrease is visible for the same concentration of liposomes, 10 µM and 7.5 µM respectively. P2wt with bicelles

(Figure 28 B) indicated a more stable absorbance over time, than for any of the other protein. 10 µM and 7.5 µM concentration gave the highest absorbance from the beginning, starting at 0.31 and 0.22 that stabilized around 0.25 over the 30 min. 10 µM, 7.5 µM and 5 µM P2wt mixed with liposomes all disclosed similar absorbance curves starting around 0.06 and decreasing with time (Figure 28 B). The absorbance is very low compared to the MBP samples. The highest concentration of P0ct, 10 µM, was the only concentration showing some vesicle aggregation for this protein with bicelles (Figure 28 C), whereas 2.5 µM induced aggregation of the liposome sample with absorbance around 0.1.

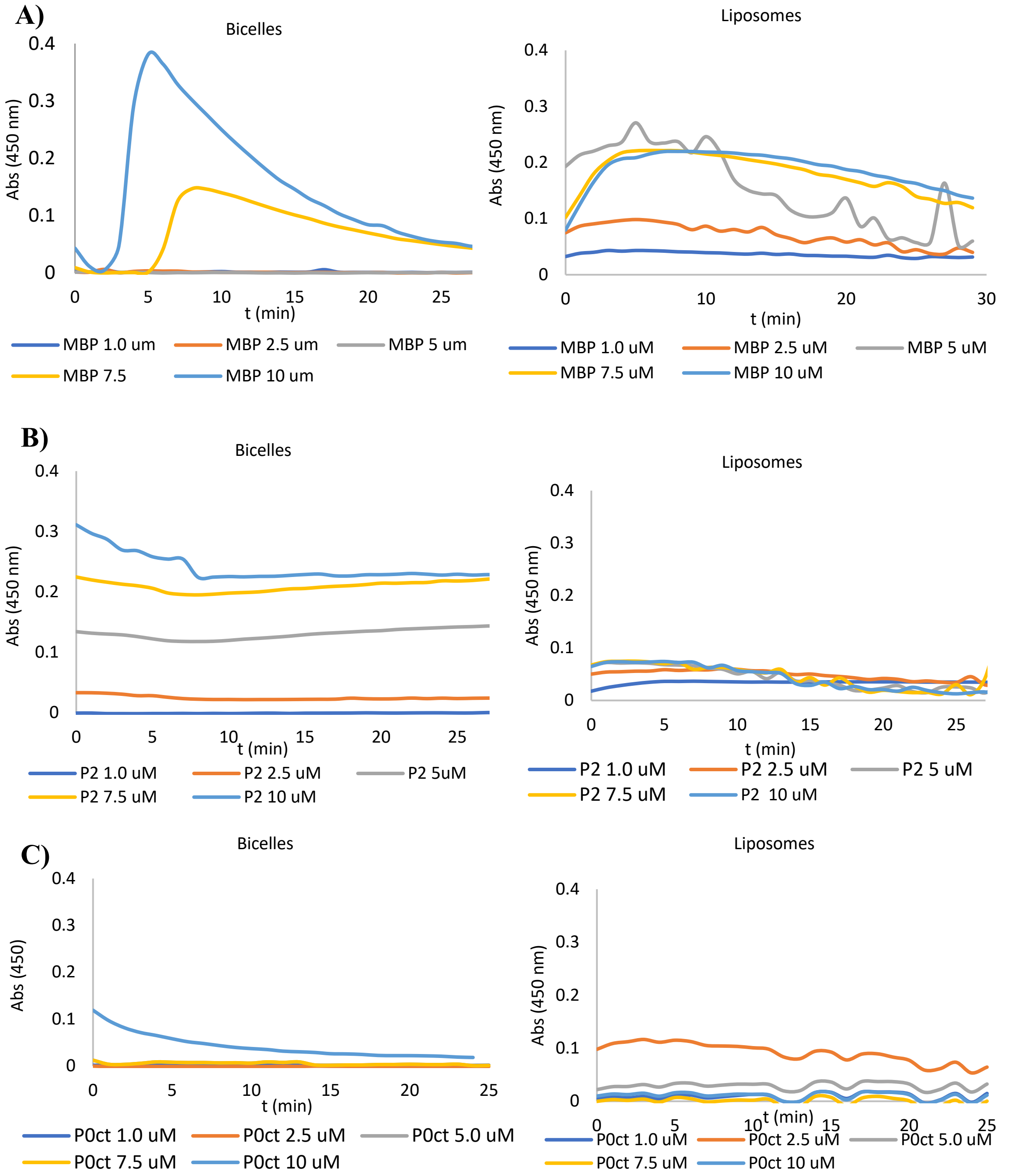

Figure 28: Concentration dependent vesicle aggregation of bicelles and liposomes with A) MBP, B) P2wt and C) P0ct. Different concentration of protein were mixed with either bicelles or liposomes (DMPC:DMPG (1:1)) and absorbance was measured with a wavelength of 450 nm over 30 minutes. The samples were measured in duplicates and a blank was subtracted from the data. The proteins to lipid ratio for the bicelles were; 1:5000, 1:2000, 1:1000, 1:666 and 1:500 and for the liposomes the protein to lipid ratio was 1:500, 1:200, 1:100, 1:66 and 1:50, from 1.0 to 10 µM respectively.

4.6 Synchrotron radiation circular dichroism measurements

SRCD measurements were performed to analyse the difference in folding of P2wt with bicelles compared to liposomes. SCRD spectra for both bicelles and liposomes are presented in Figure 29. The spectra revealed a positive peak at around 195 nm and a negative peak around 218 nm, which is consistent with an anti-parallel β-sheet structure with some variation to the different ratios of DMPC:DMPG. 9:1 lipid ratio in bicelles seems to cause less change than the 9:1 ratio of liposomes. P2wt bound to lipids do change the secondary structure as revealed by changes of the 195 nm peaks, shifting more to the right with different lipid ratio. SCRD spectra of P2wt in water and with the neutral bicelles is almost identical revealing that the DMPC bicelles do not induce any changes to the P2wt structure. P2wt with the lipid ratios of 1:1 and 4:1 overlay reasonably well on one another in the bicelle samples, while 1:1 and 0:1 liposomes do the same, indicating that the overall secondary structure do not change much between these ratios. The difference was increased between the 1:1 and 9:1 lipid ratio in bicelles, which was expected due to the increasing ratio of negatively charged lipids.

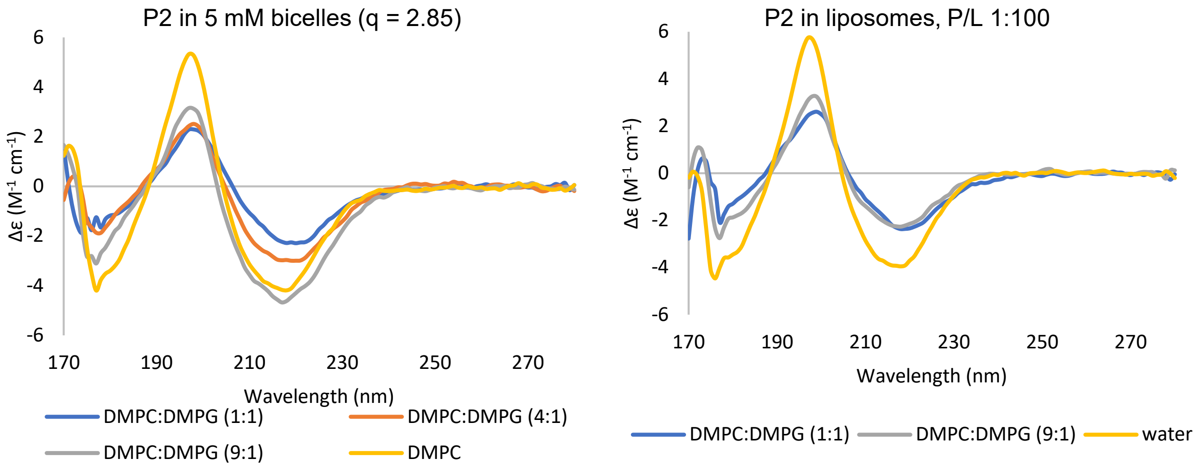

Figure 29: synchrotron radiation circular dichroism measurements of P2wt with different ratios of bicelles and liposomes (DMPC:DMPG). Difference in folding dependent on variation in DMPC:DMPG ratios for bicelles (left) and liposomes (right). The 9:1 ratio of bicelles causes less change to the secondary structure of P2wt than the same ratio in liposomes. The cuvette used was a closed cylindrical cell (Suprasil, Hellma Analytics). CD units were converted to Δε $(\mathrm{M}^{-1}\mathrm{cm}^{-1})$ after baseline subtraction.

4.7 Small-angle X-ray diffraction measurements

SAXD measurements were conducted to study the repetitive structures in turbid samples of protein (MBP, P0ct, P2wt and P2 F57A) and to investigate any differences between bicelles and liposomes.

4.7.1 MBP induce the 7.5 nm repeat distance

10 µM and 20µM MBP mixed with 1 mM and 2 mM bicelles, and 20 µM MBP added to 3 mM bicelles, gave all Bragg peaks in the X-ray diffraction spectra, while the 2 µM samples and the 10 µM mixed with 3 mM bicelles did not (not shown). All samples that induced a Bragg peak can be viewed in Figure 30, and the repeat distance was calculated to around 7-8 nm, listed in Table 4. The repeat

distance seems to be independent on the P/L ratio as long as the ratio does not exceed 1:200. Increasing ratios of protein to bicelles did not induce any Bragg peaks (not shown).

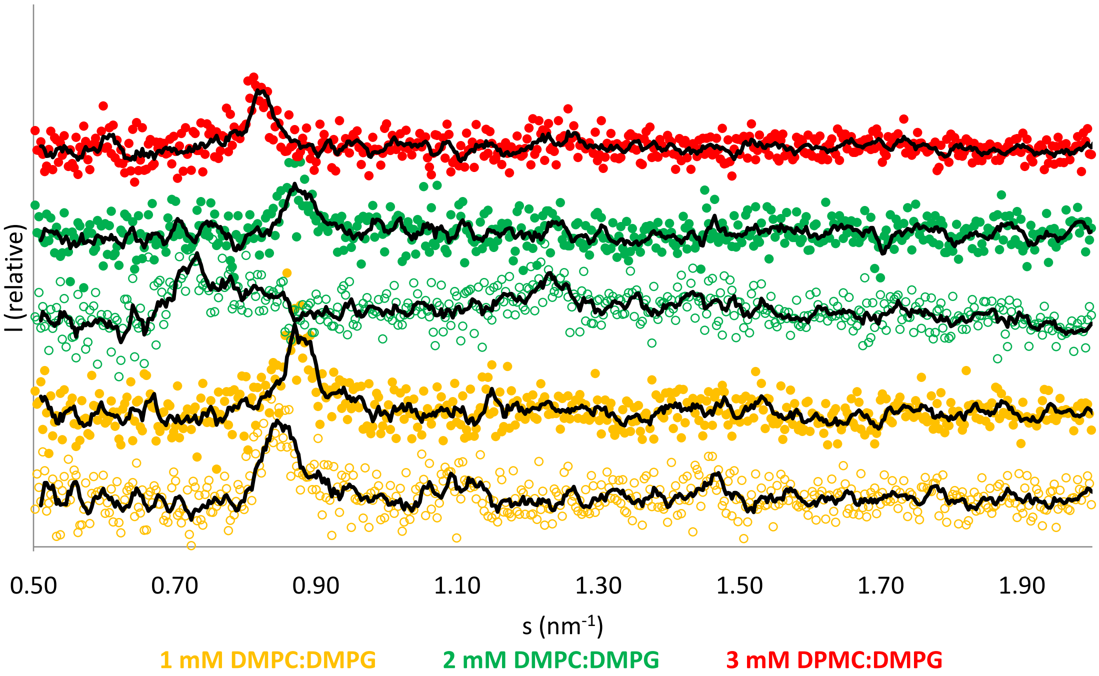

Figure 30: X-ray diffraction spectra of 10 µM and 20 µM MBP with bicelles (DMPC:DMPG (1:1)). Mixing MBP with 1-3 mM bicelles gave several major Bragg peaks in the X-ray diffraction patterns. 10 µm and 20 µM concentrations of MBP are added as open and filled markers with DMPC:DMPG ratio of the bicelles being 1:1 (10 µM with 3 mM bicelles gave no Bragg peaks). Calculated repeat distances can be viewed in Table 4. A moving average, black line, has been plotted over each dataset. For clarity all dataset are offset and are not scaled to each other. The synchrotron SAXD data were collected at PETRA III storage ring, DESY, Hamburg, Germany on beamline P12.

Table 4: Calculated repeat distances for MBP with bicelles. Mean repeat distances for induced Braggs peaks of mixing MBP with bicelles with given P/L ratio and concentration of bicelles. The s-values corresponding to the intensity summit of each Bragg peak were used to calculate the repeat distances. Graphs of each P/L ratio is viewed in Figure 30.

P/L ratio	**mM bicelles**	**µM protein**	**Repeat distance (nm)**
1:50	1	20	7.2
1:100	1	10	7.4
1:100	2	20	7.2
1:150	3	20	7.7
1:200	2	10	7.3

Not all of the liposome samples gave Bragg peaks in the X-ray scattering spectra, and no sharp peaks were observed. Presented in Figure 31 are vague peaks of 20 µM MBP mixed with 1-3 mM liposomes (filled marker) and one of 10 µM sample mixed with 3 mM bicelles (red open marker). For 20 µM MBP mixed with 1 mM and 2 mM bicelles, 1:50 and 1:100 P/L ratio, a repeat distance at 7.3 nm and 7.4 nm can be calculated from the s-value corresponding to the intensity summit of each Bragg peak. More blurred peaks are found for the 3 mM samples, set aside the errors, one can calculate repeat distances at 7.8 nm and 7.5 nm, from the 10 µM and 20 µM sample, respectively. All repeat distances calculated from the X-ray diffraction spectra, viewed in Figure 31 are listed in Table 5.

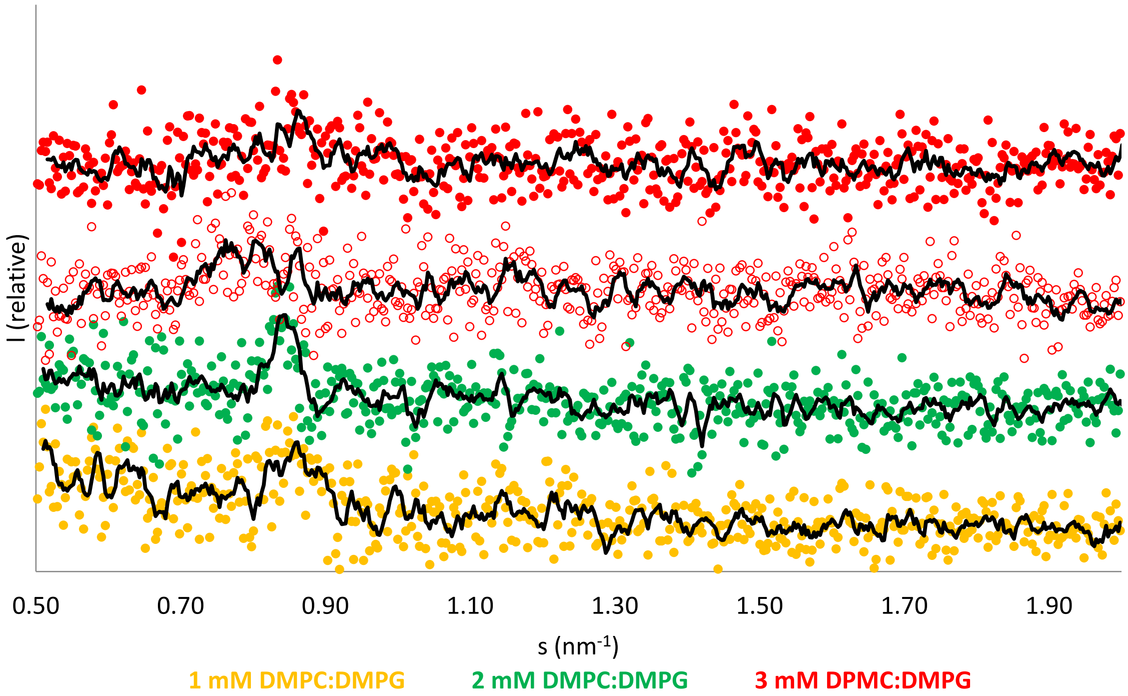

Figure 31: X-ray diffraction spectra of 10 µM and 20 µM MBP with liposomes (DMPC:DMPG (1:1)). Mixing MBP with 1-3 mM gave several Bragg peaks in the X-ray diffraction patterns. 10 µm and 20 µM concentrations of MBP are added as open and filled markers with DMPC:DMPG ratio of the bicelles being 1:1. A moving average, black line, has been plotted over each dataset. For clarity all dataset are offset and are not scaled to each other The synchrotron SAXD data were collected at PETRA III storage ring, DESY, Hamburg, Germany on beamline P12.

Table 5: Calculated repeat distances for MBP with liposomes (DMPC:DMPG (1:1)). Mean repeat distances for induced Braggs peaks of mixing MBP with liposomes with given P/L ratio and concentration of bicelles and protein. The s-values corresponding to the intensity summit of each Bragg peak were used to calculate the repeat distances. Graphs of each P/L ratio is viewed in Figure 31.

P/L ratio	**mM liposomes**	**µM protein**	**Repeat distance (nm)**
1:50	1	20	7.3
1:100	2	20	7.4
1:150	3	20	7.5
1:300	3	10	7.8

4.7.2 P2 wt and F57A induce highly ordered structures

P2wt mixed with liposomes, of either concentration, did not induce any Bragg peaks. Diffraction spectra of P2wt with bicelles gave ordered repetitive structures with all concentration of bicelles with 10 µM and 20 µM protein. 10 µM P2wt gave 1-4 Bragg peaks, with increasing number of peaks with increasing concentration of bicelles (open markers in Figure 32, Table 6). For the 20 µM samples, the two lowest proteins to lipid ratios (P/L ratio) gave two Bragg peaks at between 6-8 nm, in contrast to the 1:150 P/L ratio which induced 6 clear Braggs peaks corresponding to repeat distances from 3.5 to

7.3 nm, listed in Table 6. The first and second peak in each samples corresponded to the same repeat distances, while the last peaks for 1:300 and 1:150 P/L ratio gave a higher ordered structure. The highest concentration of bicelles and P3wt induced the highest order of repetitive structures (red filled markers in Figure 32), listed in Table 6 for 1:150 ratio.

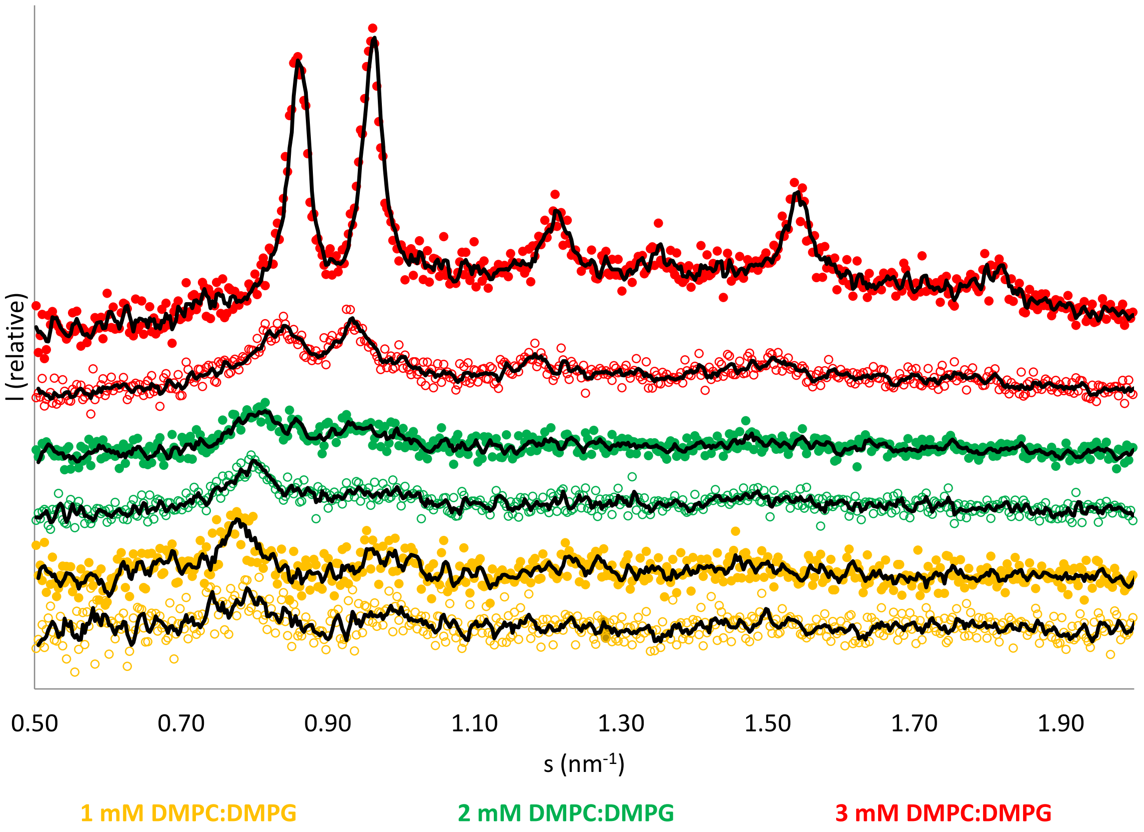

Figure 32: X-ray diffraction spectra of 10 µM and 20 µM P2wt with bicelles (DMPC:DMPG (1:1)). Mixing P2wt with 1-3 mM gave several major Bragg peaks in the X-ray diffraction patterns. 10 µm and 20 µM concentrations of P2wt are added as open and filled markers with DMPC:DMPG ratio of the bicelles being 1:1. The sample with highest concentration of both bicelles and P2wt induced most Bragg peaks and corresponding repeat distances are listed in Table 6.A moving average, black line, has been plotted over each dataset. For clarity all dataset are offset and are not scaled to each other. The synchrotron SAXD data were collected at PETRA III storage ring, DESY, Hamburg, Germany on beamline P12.

Table 6: Calculated repeat distances for P2wt with bicelles (DMPC:DMPG (1:1)). Mean repeat distances for induced Braggs peaks of mixing P2wt with bicelles with given P/L ratio and concentration of bicelles. The s-values corresponding to the intensity summit of each Bragg peak were used to calculate the repeat distances. Graphs of each P/L ratio is viewed in Figure 32.

P/L ratio	**mM bicelles**	**µM protein**	**Repeat distance (nm)**					
1:50	1	20	8.1	6.5				
1:100	1	10	8.0					
1:100	2	20	7.8	6.7				
1:150	3	20	7.3	6.5	5.2	4.6	4.1	3.5
1:200	2	10	7.8	6.7				
1:300	3	10	7.5	6.7	5.3	4.2		

The P2 F57A mutant induced Bragg peaks with bicelles and liposomes, except for the samples containing 2 µM protein with bicelles (not shown), independently of lipid concentration. All samples induced three Bragg peaks, listed in Table 7, except for the 1:50 ratio which only produced two Bragg peaks corresponding to 8.3 nm and 6.6 nm repeat distances (orange filled markers in Figure 33). As seen for the Pwt, also the highest concentration of bicelles mixed with 20 µM proteins (1:150 P/L ratio) gave the highest count of Bragg peaks, total of 6, with the first peak corresponding to a mean repeat distance of 10.4 nm, which was not seen for any of the other protein-lipid composition. The peak is present in Figure 33 at 0.607 nm^{-1} for the red filled markers. Clearer and sharper peaks were seen for the 1:300 and 1:150 P/L ratio contrasted to 1 mM and 2 mM bicelles.

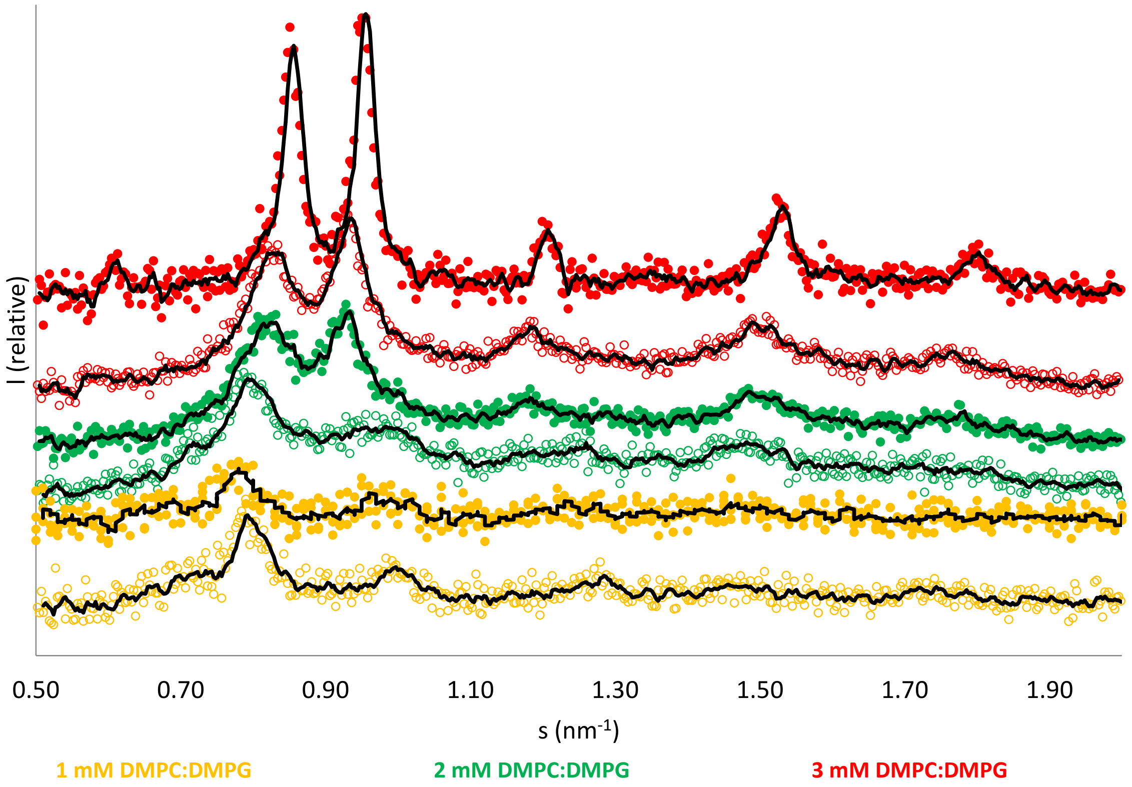

Figure 33: X-ray diffraction spectra of 10 µM and 20 µM P2 F57A with bicelles (DMPC:DMPG (1:1)). Mixing P2 F57A with 1-3 mM gave several major Bragg peaks in the X-ray diffraction patterns. 10 µm and 20 µM concentrations of the mutant are added as open and filled markers with DMPC:DMPG ratio of the bicelles being 1:1. 6 Bragg peaks were induced in the samples containing highest concentration of protein and bicelles (red filled marker). A moving average, black line, has been plotted over each dataset. For clarity all dataset are offset and are not scaled to each other. The synchrotron SAXD data were collected at PETRA III storage ring, DESY, Hamburg, Germany on beamline P12.

Table 7: Calculated repeat distances for P2 F57A with bicelles (DMPC:DMPG (1:1)). Mean repeat distances for induced Bragg peaks of mixing P2 F57a with bicelles with given P/L ratio and concentration of bicelles. The s-values corresponding to the intensity summit of each Bragg peak were used to calculate the repeat distances. Graphs of each P/L ratio is viewed in Figure 33.

P/L ratio	**mM bicelles**	**µM protein**	**Repeat distance (nm)**					
1:50	1	20	8.3	6.6				
1:100	1	10	7.9	6.3	4.9			
1:100	2	20	7.7	6.8	5.3	4.2	3.6	
1:150	3	20	10.4	7.3	6.6	5.2	4.1	3.5
1:200	2	10	7.9	6.6	6.4	4.2		
1:300	3	10	7.6	6.8	5.3	4.3	3.6	

P2 F57A generated at least one Bragg peak in all liposome samples (10 µM and 20 µM shown in Figure 34), even those with only 2 µM protein (graph can be viewed in Appendix 8.6). All samples induced the first Bragg peak corresponding to a repeat distance between 7-9 nm and several with the second one being at 4.4-4.5 nm. The sharpest peaks were induced with the 3 mM bicelles, where the 1:300 P/L ratio gave the most distinct peak (red open markers in Figure 34). The 1:100 P/L ratio (green filled makers) was the only sample that induced only one Bragg peak that corresponded to a mean repeat distance at 7.3 nm. The 1:150 P/L ratio containing 3 mM bicelles (red filled marker) induced two Bragg peaks, with the latter being of second order.

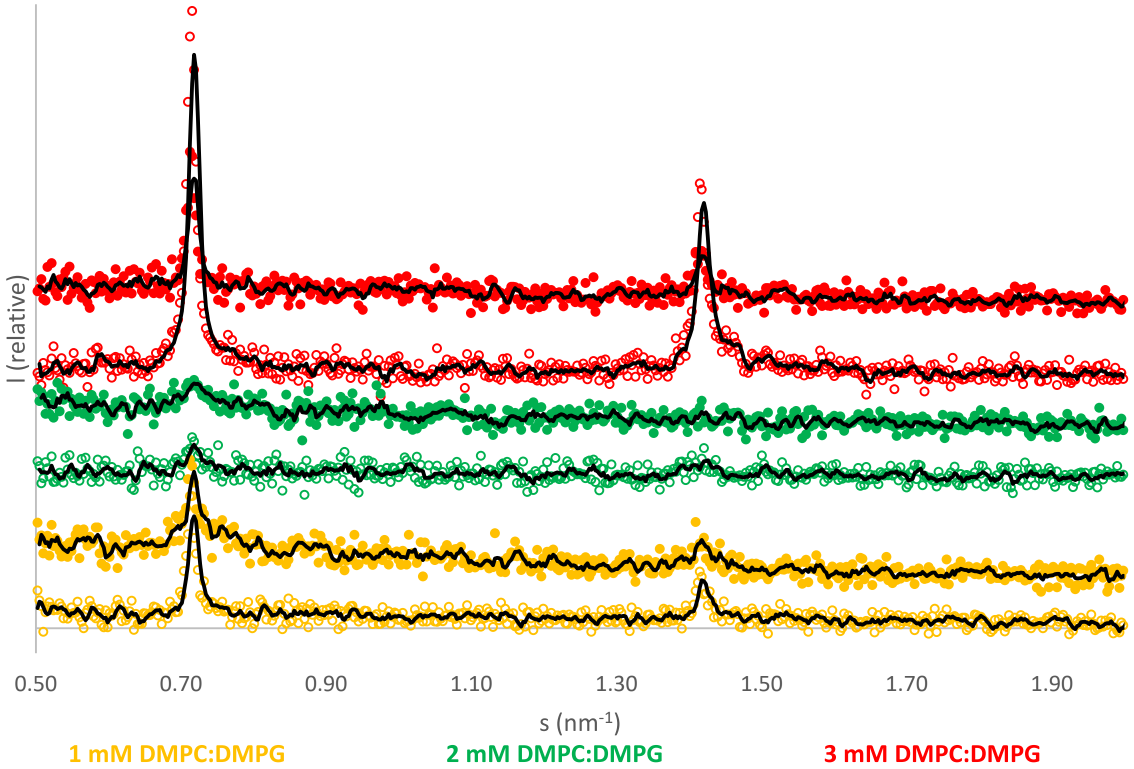

Figure 34: X-ray diffraction spectra of 10 µM and 20 µM P2 F57A with liposomes (DMPC:DMPG (1:1)). Mixing P2 F57A with 1-3 mM gave two Bragg peaks in the X-ray diffraction patterns for most of the P/L ratios. 10 µm and 20 µM concentrations of the mutant are added as open and filled markers with DMPC:DMPG ratio of the liposomes being 1:1. 1:150 P/L ratio (red filled marker) induced a peak of second order. The 1:100 P/L ratio with 20 µM protein (green filled marker) was the only sample inducing only one Bragg peak corresponding to 7.3 nm. A moving average, black line, has been plotted over each dataset. For clarity all dataset are offset and are not scaled to each other. The synchrotron SAXDdata were collected at PETRA III storage ring, DESY, Hamburg, Germany on beamline P12.

Table 8: Calculated repeat distances for P2 F57A with liposomes (DMPC:DMPG (1:1)). Mean repeat distances for induced Bragg peaks of mixing P2 F57A with liposomes with given P/L ratio and concentration of bicelles. The s-values corresponding to the intensity summit of each Bragg peak were used to calculate the repeat distances. Graphs of each P/L ratio (except for 2 µM protein) are viewed in Figure 34.

P/L ratio	**mM liposomes**	**µM protein**	**Repeat distance (nm)**	
1:50	1	20	8.7	4.5
1:100	1	10	8.6	4.4
1:100	2	20	7.3	
1:150	3	20	8.8	
1:200	2	10	8.7	4.4
1:300	3	10	8.7	4.5
1:500	1	2	8.7	4.4
1:1000	2	2	8.7	4.4
1:1500	3	2	7.1	4.4

4.7.3 P0ct induced two Bragg peaks

All samples containing P0ct and bicelles showed no Bragg peaks in the X-ray diffraction profile (not shown), only form factors. 20 µM P0ct induced two bright peaks when mixed with liposomes (Figure 35), corresponding to a protein to lipid ratio of 1:50, 1:100 and 1:150 respectively. The mean repeat distances were calculated for the spectra and are listed in Table 9. All concentration of P0ct showed a repeat distance around 7.5 nm with a second peak around 1.6 nm^{-1}. For the 1:150 P/L ratio the second peak can be of the second order of the first one.

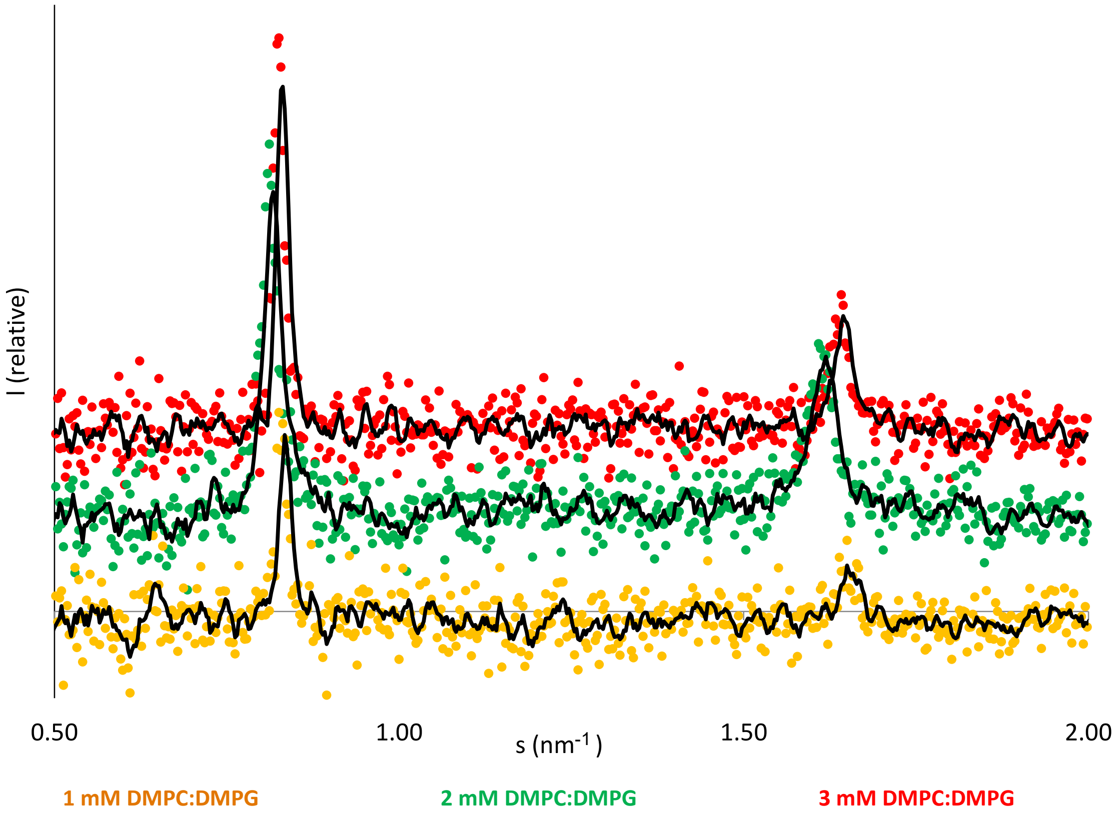

Figure 35: SAXD analysis of 20 µM P0ct mixed with different concentration of liposomes (DMPC:DMPG (1:1)). Mixing 20 µM P0ct with 1-3 mM gave two major Bragg peaks in the X-ray diffraction patterns. First peak corresponds to a repeat distance of 7.6 nm (± 1), while letter is of second order. A moving average, black line, has been plotted over each dataset. For clarity all dataset are offset and are not scaled to each other. The synchrotron SAXD data were collected at PETRA III storage ring, DESY, Hamburg, Germany on beamline P12.

Table 9: Calculated repeat distances for P0ct with liposomes (DMPC:DMPG (1:1)). Mean repeat distance for induced Braggs peaks of mixing P0ct with liposomes with given P/L ratio and concentration of bicelles. The s-values corresponding to the intensity summit of each Bragg peak was used to calculate the repeat distances.

P/L ratio	mM liposomes	µM protein	Repeat distances (nm)	
1:50	1	20	7.5	3.8
1:100	2	20	7.7	3.9
1:150	3	20	7.6	3.8

4.8 Myelin protein shows stacking of lipids

TEM was used to get a further understanding of binding between the proteins (MBP, P2wt and P0ct) to bicelles and liposomes. Proteins were mixed with an old batch (1 month old) or a new batch of bicelles to study the effect of storing lipids in ambient temperatures.

MBP was mixed with either an old batch or a new batch of bicelles (1:22 P/L ratio). Large chunks of sample were seen all over the grid for the old batch, as viewed in Figure 36 (left). A closer look (zoomed image) revealed binding of MBP to the bicelles, making ordered strands of bicelles elongated throughout the lumps indicating possible fusing of the bicelles. Mixing with new bicelles, right image in Figure 36, did not show the same order of binding. Strands of bicelles binding together could not be seen.

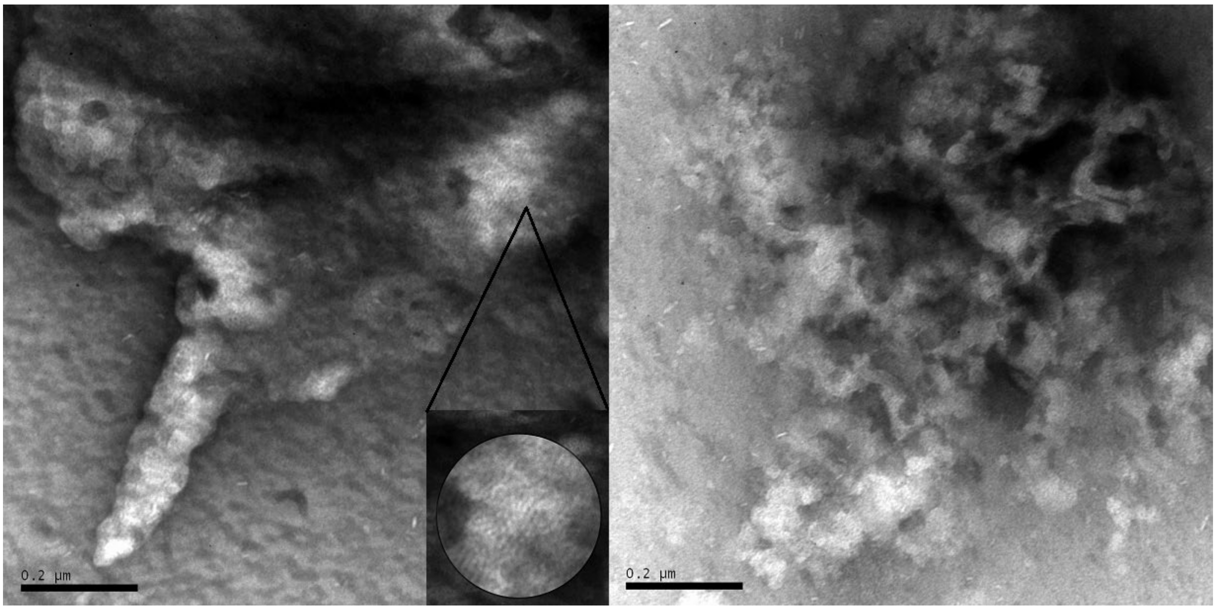

Figure 36: Transmission electron micrograph of MBP with old (left) and new (right) batch of bicelles (1:22 P/L ratio). Protein binding is visible when mixing with the old batch of bicelles (left). The sample was stained with 2% uranyl acetate before imaging. TEM imaging was preformed using a Jeol JEM-1230 (MedWOW) instrument at the molecular imaging center (MIC), Department of Biomedicine, University of Bergen.

TEM imaging of P2wt revealed excessive binding to the bicelles with 1:22 P/L ratio, Figure 37, with P2wt binding to the flat surfaces of the bicelles. Bicelles appears as white strings, which is a strong indication that P2wt binds to the flat surfaces of the bicelles. This was expected since the lipids resides on the surface while the detergent is on the sides. P2wt seemed to induce a more random binding than MBP. When imaging P2wt with liposomes, a 1:100 P/L ratio was used (Figure 38), and the micrographs revealed no elevated binding compared to the bicelle sample. Most liposomes were not bound together, but some attachments were spotted between a few liposomes (Figure 38, right image). It might be because of the P/L ratio, which was highly increased compared to the P/L ratio in the bicelles. P2 sample with old bicelles was not imaged due to broken membrane.

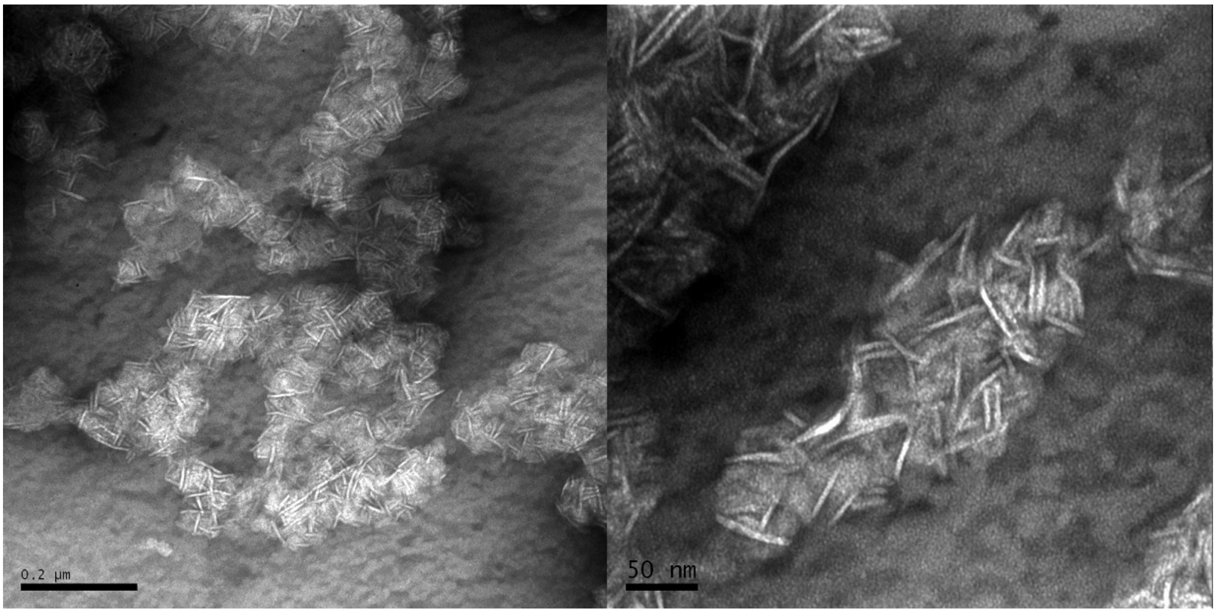

Figure 37: Transmission electron micrograph of P2wt with bicelles (1:22 P/L ratio). Protein binding is evident with the clumps of bicelles all over the glow-discharged grids (white strings). 0.5 mg/mL P2wt was mixed with 0.5 mg/mL bicelles and incubated for 1 hour before imaging. The sample was stained with 2% uranyl acetate before imaging. TEM imaging was preformed using a Jeol JEM-1230 (MedWOW) instrument at the molecular imaging center (MIC), Department of Biomedicine, University of Bergen.

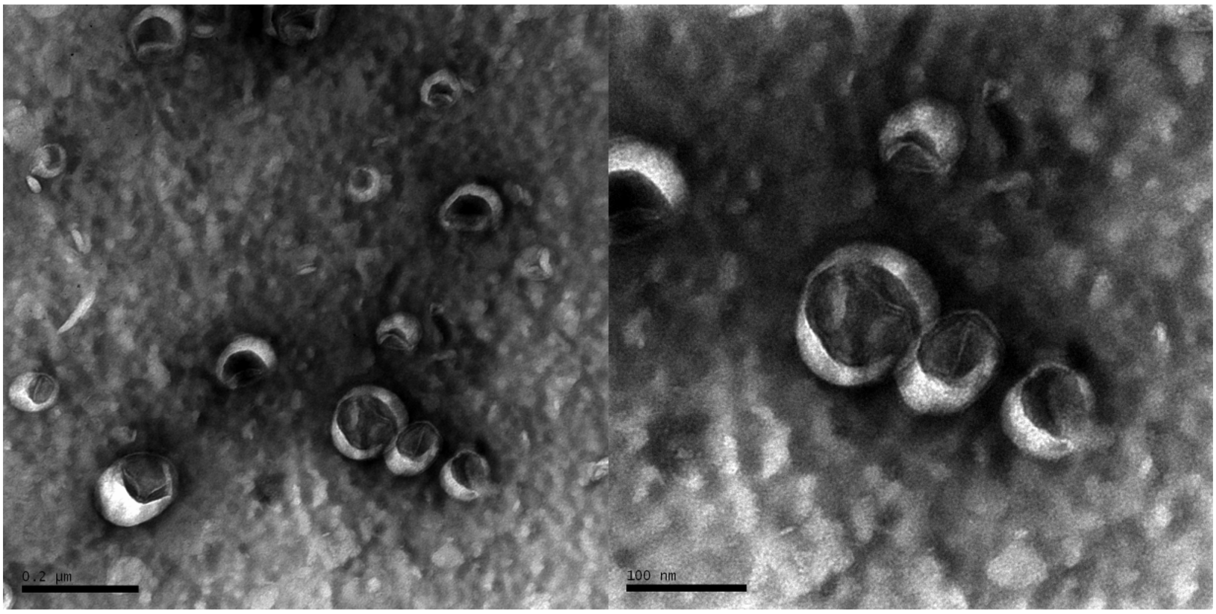

Figure 38: Transmission electron micrograph of P2wt with liposomes (1:100 P/L ratio). Some binding might be seen with the liposomes sticking together. The sample was stained with 2% uranyl acetate before imaging. TEM imaging was preformed using a Jeol JEM-1230 (MedWOW) instrument at the molecular imaging center (MIC), Department of Biomedicine, University of Bergen

Binding of liposomes was seen when mixing them with P0ct (Figure 39). 1:100 P/L ratio was imaged and the micrographs indicates nicely binding of liposomes. Several liposomes could be seen sticking together confirming P0ct binding. P0ct did not induce aggregates in the same manner as MBP and P2wt, but rather elongated binding of the liposomes, revealing that the cytoplasmic tail of P0 have a lipid binding function, but do not aggregate lipid bilyers. Samples containing bicelles had broken grids and no image could be taken from those samples.

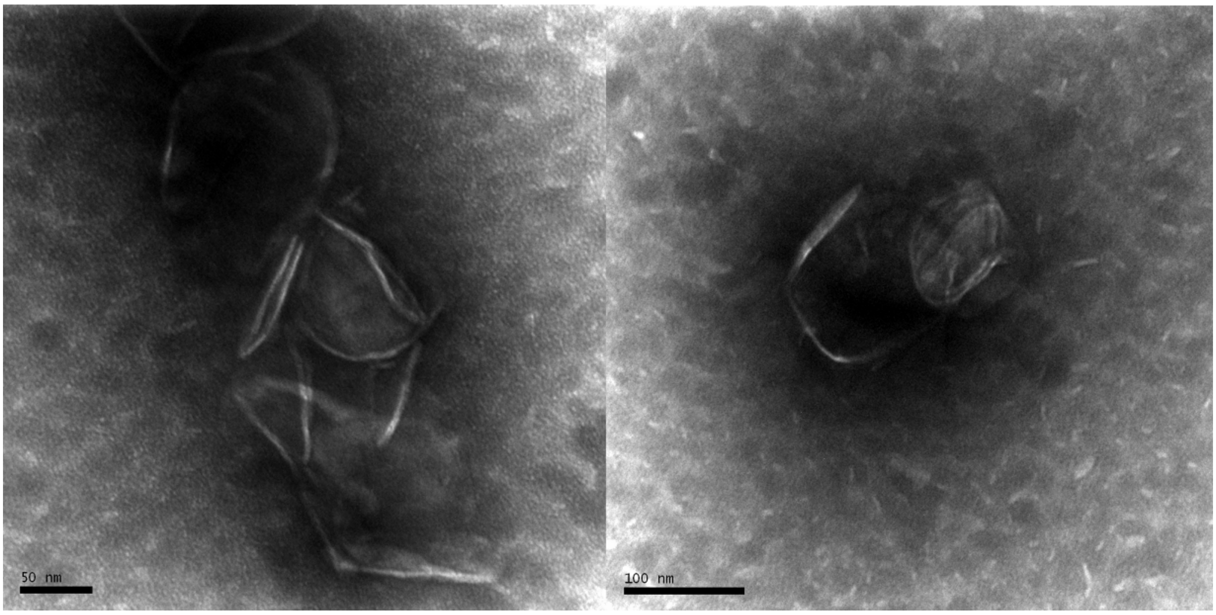

Figure 39: Transmission electron micrograph of P0ct with liposomes (1:100 P/L ratio). Protein binding is evident with the clumps of liposomes. The sample was stained with 2% uranyl acetate before imaging. TEM imaging was preformed using a Jeol JEM-1230 (MedWOW) instrument at the molecular imaging center (MIC), Department of Biomedicine, University of Bergen.

TEM images of only bicelles (1 mM sample) were taken as a control and to investigate how binding to protein changes bicelle appearance. The micrographs (Figure 40) displayed bicelles of varying size which did not stick together. Grids with and without glow-discharge was used to test the difference. The results showed that the glow-discharging was not needed for imaging bicelles. The micrographs were taken with 15k-80k magnification.

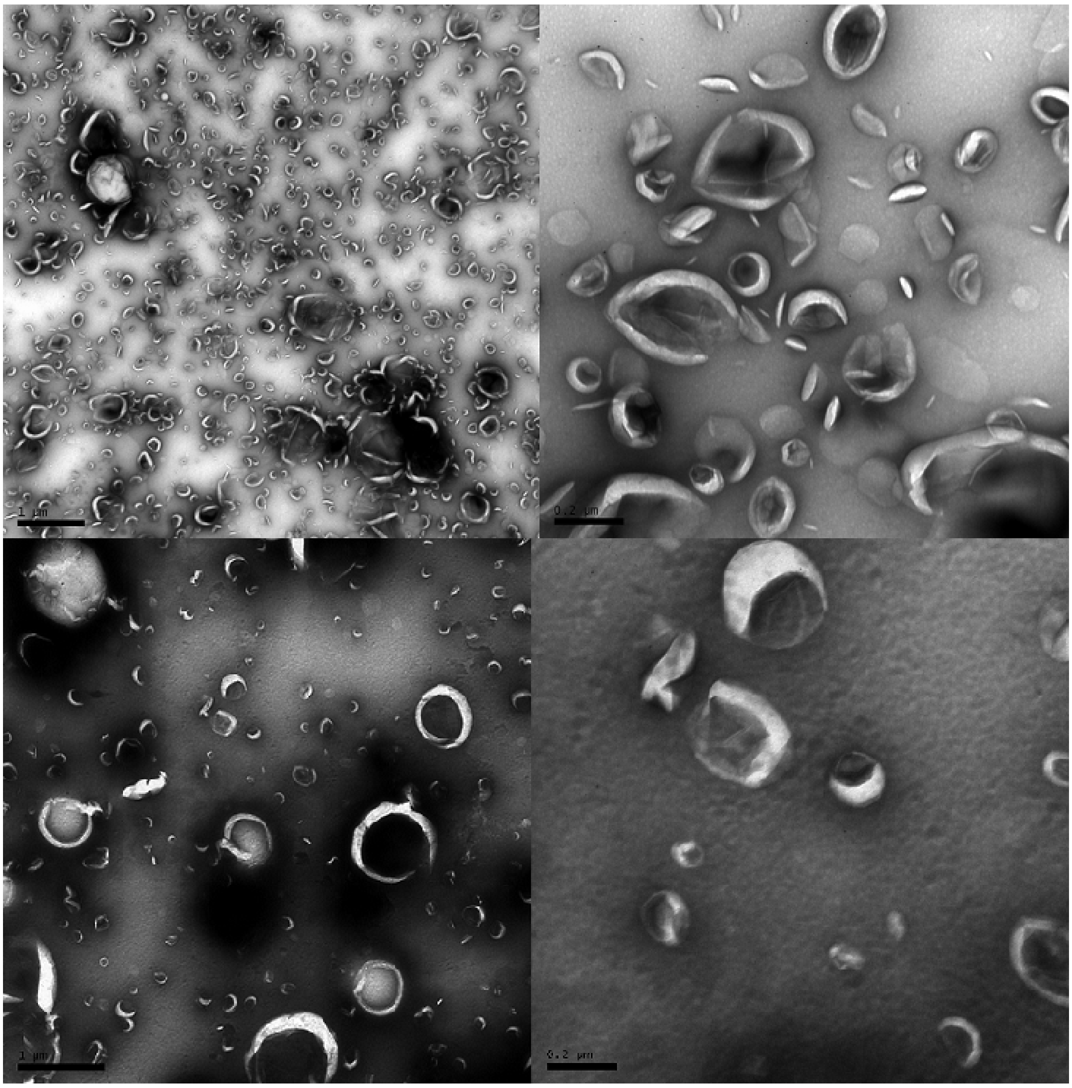

Figure 40: Transmission electron micrograph of only bicelles. Top images are without glow-discharge and the images below are with glow-discharged grids. TEM imaging was preformed using a Jeol JEM-1230 (MedWOW) instrument at the molecular imaging center (MIC), Department of Biomedicine, University of Bergen.

The glow-discharged grids induced a lot of problems. Micrographs of many samples were not possible due to damaged membrane on the grids. It was clear that the glow-discharging step needed more optimization to

5 Discussion

5.1 Successful purification of each protein

Purification of each myelin protein, MBP, P2wt and the cytoplasmic tail of P0 (P0ct), were performed after well-established methods (40, 60, 69). They all include at least one Ni-NTA affinity chromatogrphy which is a widely used method in purification of recombinant proteins with the use of a His-tag (154). When monitoring each step of a purification process the important role of Ni-NTA chromatography and size-exclusion chromatography can be seen. Doing SDS-PAGE analysis from each step during and after the purification process is also a way to observe how the purification is going. The SDS-PAGE analysis of the collected fractions revealed fractions with pure proteins and some fractions with impurities. Each time, SDS-PAGE analysis was done after every affinity chromatography to check the present of the protein before continuing the process. By monitoring each step closely, purification of myelin proteins will end in pure proteins with good yields almost every time. The protocols used are optimized and well established, and the resulting pure proteins with high concentrations are a good identification of the reproducibility. If the yield varies a lot from each time or the protein aggregates during the purification process, then it is a sign of something not optimal.

5.2 Co-sedimentation assay revealed no binding to lipid coated Fe_3O_4 and SiO_2 nanoparticles

The Fe_3O_4 and SiO_2 nanoparticles were coated with DMPA and DPPC through ODS. DMPA has a negatively charge head group while DPPC is zwitterionic with net neutral charge. The proteins MBP, P2wt and P0ct should therefore bind to the DMPA coated nanoparticles, while the DPPC coated ones was used as a negative control. The co-sedimentation analysis of either nanoparticle coated with DMPA with MBP, P2wt and P0ct revealed no or little binding. SDS-PAGE analysis revealed protein content in all samples (Figure 12) and no binding could not be due to lack of protein. In some of the SDS-PAGE analyses for both coated Fe_3O_4 and SiO_2 nanoparticles, weak bands were visible in the pellet fractions with both DMPA and DPPC. This could indicate some binding, but it is probably due to supernatant still present in the pellet samples. When centrifuging protein-lipid mixtures, it is easy to see a pellet in the bottom of the tube hanging quite firmly to the bottom, which means that the supernatant can easily be removed and no band appear in the supernatant fraction. Trying to remove the supernatant from the centrifuged samples containing protein and lipid coated nanoparticles was not easy. The pellets did not stick to the plastic tubes and could simply be mixed with the supernatant again, which made it difficult to remove all supernatant from the pellets. The weak band seen in the supernatant fractions is possibly due to this problem and do not represent a binding between the proteins and nanoparticles. This is also confirmed with weak band appearing in the pellet samples from DPPC coated nanoparticles that should not bind to the proteins. Even so, if the proteins were bound to DMPA there should have been a strong band indicating this in the pellet fractions.

The reason for no protein binding must be the coated nanoparticles themselves and maybe the preparation methods used. Even though the protocol of how the ODS modified nanoparticles were coated with DMPA or DPPC were described, there are no description of how the solid Fe_3O_4 and SiO_2 nanoparticles were modified with ODS, so parameters influencing the modification cannot be checked. The SEM images provided by Professor Chaozhan Wang revealed that both Fe_3O_4@ODS nanoparticles (150 nm) coated with DMPA and DPPC were aggregated and aggregated dried nanoparticles can be also very hard to redisperse as individual nanoparticles. When both Fe_3O_4 and SiO_2 coated nanoparticles were redispersed in buffer before co-sedimentation assay, they did not make a homogenous solution. Sonication by probe and water bath was tested to see if they dispersed homogenously, but the nanoparticles were still aggregated. The finished lipid coated nanoparticles were also dried in vacuum at 50 ºC, which may have damaged the lipid coating somehow. Aggregation of the particles might be due to rapid removal of water when drying them in vacuum, which have been seen before with lipid coated gold nanorods (155) and aggregation can have an effect on protein binding. After the co-sedimentations assays and two attempts to coat Fe_3O_4 with DMPC:DMPG with any improvement of protein binding, the decision was made to go over to gold nanoparticles.

5.3 Color change of the gold nanoparticles indicated a lipid coating and protein binding

There are many protocols for coating of gold nanoparticles (AuNPs) with lipids through thiol functionalization. Three protocols were tested with modification that matched the smaller AuNP volumes (1, 132, 153). Co-sedimentation assay did not indicate binding to the coated AuNPs. The many bands in the supernatant fractions reveal that the protein solution contains many degradation products, which are a result from standing on ice too long, but did not affect the assay since MBP was present in the solution and the controls that the co-sedimantion assay worked, with MBP binding to the DMPC:DMPG (1:1) liposomes and not to the bare AuNPs, which is expected. Since the AuNPs coated with protocol 3 had a strong colour change when MBP was added (Figure 18), further investigation of these nanoparticles was done with UV-vis spectroscopy and TEM.

5.3.1 UV-vis spectra and TEM revealed partial coating of the AuNPs

UV-vis spectroscopy of the lipid coated nanoparticles by protocol 3 (1) was done to investigate any red shift in the spectra, which would be indicative of a lipid coating of the AuNPs modified with 1-octanethiol. A shift to a longer wavelength for the absorption peak indicates nanoparticles of increased size because of changes in the surface plasmon resonance, which is dependent on gold nanoparticle size (156). When the raw data was normalized to peak maxima (Figure 20) a small red shift could be seen. The red shift of 4 nm might indicate the lipid coating of the particles but the spectra also revealed an increased base line at higher wavelength, which signifies aggregated nanoparticles. When gold nanoparticles aggregate the electrons at their surface becomes shared among neighbouring particles. This result in a shift to lower energies for the SPR and absorbance peaks shift to longer wavelengths and the original peak will decrease in intensity (157). There was also a color change when the coating was applied. The bare AuNPs absorbs at 544 nm which is in the green spectrum of the visible light, which make the nanoparticles appear red because red is the complementary colour to green (125). The DMPC:DMPG coated AuNPs absorbs light at higher green wavelengths and to the naked eye appear more burgundy. With increasing size of the nanoparticles the colour will shift from red to purple to blue before progressing to a clear solution. The magenta colour of the lipid coated AuNPs is also a sign of more aggregated solution. The shoulder with absorbance at 360 nm the UV-vis spectra of the coated nanoparticles indicated that the lipids was present in the gold nanoparticle solution. Since the lipid coated AuNPs had an absorption spectra that had the same shoulder as the lipid mixture alone and a red shift with aggregates, which makes the solution more burgundy than red, the spectra indicated a DMPC:DMPG coating of the thiolated AuNPs, which was further confirmed with TEM. Old batch of coated AuNPs (Figure 21) could not be images with high resolution due to damage membrane on the glow-discharged grids. When the electron beam hits the sample the membrane might get damage due to the high temperature. When this happened the samples moved too much to take any high-resolution images. The micrograph of the stained coated AuNPs, revealed some bright rings around the nanoparticles (indicated by black arrows), which might be the DMPC:DMPG (1:1) coating. 20 nm gold nanoparticles have been successfully coated with other types of lipids confirmed with TEM. The lipid coating was determined to be 4-6 nm and caused a red shift in the UV-vis spectra of 13 nm (158). Coating of the 80 nm AuNPs might have been partially completed only forming on some of the AuNPs, which could explain a partially red shift of 4 nm and the lipid coating only visible on some of the nanoparticles in the AuNP clusters. On the other hand, the gold nanoparticles coated by Kim et al. were clustered together by the lipid membranes causing the 20 nm nanoparticles to increase in size to 100 nm clustered aggregations of gold nanoparticles with surrounding lipids that also might explain the red shift of 13 nm. Whereas the coated AuNP, viewed in Figure 22, seems to have a lipid coating that encircles each nanoparticle individually which could cause a smaller red shift corresponding to smaller increased size of each single nanoparticle. When comparing the micrograph of the coated AuNPs to the bare ones (Figure 23) the coated AuNPs indicates more aggregations as they are more clustered together than the bare AuNPs. If coated correctly the negatively charge DMPG lipid should repel each other on adjacent lipid membranes and the AuNPs would not be aggregated. Diameter of the bare AuNPs were measured to be 75 nm and confirmed the size ordered from NanoComposix with some variation in size distribution.

The pilot study with the nanoparticles indicates over all the functionalization of the nanoparticles need optimization together with the coating protocols. Functionalization of gold nanoparticles with thiols should be an easy process in theory due to the high bond strength between sulphur and gold. Since the functionalization is caused by self-assembly it can be hard controlling the resulting size and control the complete replacement of already existing ligand shell (159), confirmed by this study. The coating could in this case only be verified by TEM, which revealed partial coating and not a complete coating. Even though thiol functionalization is common other types of stabilization can also be used to make inorganic nanoparticles more biocompatible. One other option is a coupling reaction using 1-ethyl-3-3-dimethylaminopropyl carbodiimide (EDC) and N-hydroxysulfosuccinimide (Sulfo-NHS), shortened to EDC-NHS covalent coupling. This technique requires carboxylated surface to which for example protins can be covalently coupled to. A stable intermediate, Sulfo-NHS ester reacts with primary amines in the protein and forms a stable amide bond (160). This can be useful if one wants to study with TEM where the protein resides in lipid aggregated. Coupling to gold will give highly detectable samples in TEM since gold have high electron density. Several other methods that could be used are steric stabilization by polymeric ligands that can for instance increase circulation time in the blood, ligand exchange with the used of nitrogen-based ligands or ligand addition by adding a ligand on to an existing shell to introduce desired chemical groups (161).

5.4 P0ct favours DMPC:DMPG over DOPC:DOPS liposomes

Concentration dependency of P0ct to liposomes of DMPC:DMPG or DOPC:DOPS (1:1) was studied to see if there was any minimum level of lipids that was needed for binding of P0ct. Co-sedimentation assay was deduced and the SDS-PAGE was analysed. Most of P0ct resided in the supernatant in lowest ratio of P/L (1:0.5), but more is bound to the DMPC:DMPG liposomes than the DOPC:DOPS liposomes. Further indication of stronger binding to the DMPC:DMPG liposomes can be concluded with the stronger bands in the pellet fraction arised for the 1:1 and 1:2 P/L ratios, whereas for the DOPC:DOPS liposomes stronger bands did not become visible before the highest ratios of P/L is was used.

The main difference between the two lipid compositions are that the DMPC and DMPG lipids have saturated lipid tails consisting of 14 carbons, while the DOPC and DOPS lipids are unsaturated in a *cis* conformation consisting of 18 carbons. The DOPC:DOPS mixture is already in a fluid disordered gel phase, with phase transition temperatures of -11ºC and -17ºC, respectively, while the DMPC:DMGP might be in a gel phase since their phase transition temperatures are higher (24ºC and 23ºC) (101), right above room temperature. This can have an effect on the binding of P0ct. The cytoplasmic tail of P0 resides in the MDL of compact myelin where the cytoplasmic leaflet of the lipid bilayers in concentrated with charged phospholipids (27, 56). For the co-sedimentation assay it seemed like P0ct favoured saturated lipids and binds more strongly to them than the unsaturated lipids. This have been deduced before where P0ct had the same affinity for both lipid mixtures but according to SPR measurements P0ct favoured certain lipids species where DMPC:DMPG accumulated more P0ct than DOPC:DOPS (69). Raasakka et al. also revealed that P0ct decreased the phase transition temperature of DMPC:DMPG mixtures to 22.5 °C, which would mean that the P0ct modulates fluidity of the lipids and this in turn might increase the binding of the cytoplasmic tail. This bias towards the DMPC:DMPG lipid mixture would explain that the saturation levels occurring at lower P/L ratios for the DMPC:DMPG than for the DOPC:DOPS. Why the cytoplasmic tail behaves this way is not fully understood, but further investigation of full P0 protein and its domains might reveal new properties and the proteins full function in the myelin sheath.

5.5 Differences in vesicle aggregation between liposomes and bicelles

To investigate if vesicle aggregation of DMPC:DMPG (1:1) liposomes and bicelles had some differences due to either lipid composition or protein concentration, two types of turbidity assay were conducted; one with different ratios of DMPC:DMPG and one with increasing concentrations of protein.

5.5.1 9:1 ratio of DMPC:DMPG caused delayed vesicle aggregation of bicelles

For MBP and P2wt the biggest difference between bicelles and liposomes was in the 9:1 lipid ratio, where both had a jump in absorbance after 5 min, whereas P0ct did not induce the same jump. Absorbance of all 4:1 lipid ratios did decrease from 0 min indicating that vesicle aggregation occurs rapidly, but P2wt induced an increase in absorbance again after 10 min, which can indicate some delayed binding to the bicelles as this happened for both LUV and SUV bicelles, but it also show that P2wt generates a stability for the aggregates. The delayed aggregation of bicelles with 9:1 ratio can be due to the limited amount of charged lipid content that is needed for MBP and P2 to bind, which suggest that it take some time for the proteins to aggregate bicelles containing low amounts of negatively charged lipids and therefore causes the bicelles to precipitate later than the 4:1 and 1:1 ratios. The overall lower absorbance in the absorbance spectra for MBP and P2wt indicated that MBP have a more immediate interaction to the bicelles and causes a faster precipitation. This is also verified by the fact that bicelle aggregation by MBP also reaches as steady state faster than aggregation by P2wt when comparing the absorbance spectra. P0ct with 9:1 ratios of DMPC:DMPG induced little aggregation with both LUV and SUV bicelles, and highest absorbance for the liposomes indicating some vesicle aggregation. MPB and P0ct did not induce any vesicle aggregation of the 1:0 liposomes indicated by the low absorptions. For the P2 with control, increased absorption could be detected after 10 min for the LUV bicelles. Why this happened in unknown and the measurements should be done again to check the reproducibility. Measurements done with wavelength 660 nm induced similar results for all three proteins, indicating that bicelles and SUV bicelles do not differ much in term of vesicle aggregation.

5.5.2 Stronger vesicle aggregation is seen with increased concentration of myelin proteins

With all of the proteins, MBP, P2wt and P0ct, the highest concentration of protein had the highest absorption level. The delayed aggregation that happened with the 9:1 lipid ratio was further confirmed for MBP with varying the concentration. The delayed aggregation seems to be concentration dependent where only high concentrations of MBP caused this effect. Vesicle aggregation happened after 5 min for the highest concentrations and the vesicle aggregation was stronger for the 10 μM sample, which indicated a fast and strong interactions with the bicelles dependent on concentration. 7.5 μM of MBP also caused this pattern, but with lowered tubidity. P2 did not cause this effect with the 1:1 lipid ratio, revealing that the same aggregation might dependent more on lipid ratios for P2wt than protein concentration. P2wt also seems to prompt more stable aggregation of the bicelles compared to the liposomes, which decreased faster signifying that the liposome aggregates precipitate faster than the bicelles. The 10 μM sample of P0ct indicated some aggregation of the bicelles, but the absorbance is really low and this might be because the protein to lipid ratio is 1:500 in the 10 μM sample and that there is too little protein to cause any big aggregates of bicelles. The best protein to lipid ratio for P0ct seems to be 1:5 or 1:6 as indicated from the co-sedimentation assay. For both MBP and P2wt, the three highest concentrations indicated vesicle aggregation with the liposomes, withMBP induced more turbidity than P2wt, with more stability over time, whereas it is the other way around for the bicelle samples. It might be that MBP causes more stability in liposomes aggregates and P2wt for bicelle aggregates. This could then mean that there are some property differences between the proteins that makes one favour one over the other and vice versa. With both P2wt and P0ct one can observe some difference between the liposomes samples, but the absorbance is pretty low for all concentration so no strong vesicle aggregation was measured. 5 μM of MBP with liposomes decreases more rapidly than the highest concentrations. This might be due to the fact that 5 μM of MBP do not cause as big aggregates as the two higher concentrations because there is not enough protein to do it, and therefore precipitates faster. The three highest concentration of P2wt is quite similar to each other in respect of the absorbance, which might signify that 5 μM P2wt is enough to cause aggregation of liposomes in this analysis. P0ct have some absorption for the liposome samples with the 2.5 μM sample causing highest absorption. This might indicate some vesicle aggregation of the liposomes, but probably is a result of faulty pipetting. The liposome content in the vesicle aggregation measurements are really high compared to P0ct protein concentration and one would except that the highest concentration of P0ct would have highest turbidity as seen for the other proteins and for the P0ct with bicelles.

5.6 Orientation differences of P2wt with bicelles and liposomes

SCRD was done to check for differences in P2wt conformation and orientation when bound to liposomes or bicelles. In water and with DMPC bicelles the conformation and orientation is in agreement with earlier SCRD measurements with a well-defined β-sheet structure (38, 52, 53). The β-sheet structure is consistent with the positive peak at 195 nm and a negative peak at 218 nm (Figure

29). P2wt remains in a β-sheet structure independently of binding to bicelles or liposomes with the different lipid ratios, but the spectra clearly changes when P2wt is bound to lipids. Changes in the SCRD spectra have been seen before and it is thought to stem from a partial unfolding if the α-helical lid, which is known to interact with the charged lipid head groups in lipid bilayers (38, 53). The spectra changes with the different lipid ratios, with the 9:1 ratio in bicelles inducing least change indicating that there is not enough negative charge for P2wt to bind and therefore it did not change the overall structure. Bicelles also resembles a native bilayer more than the liposomes being flat and not spherical. 1:1 lipid ratio of both bicelles and liposomes seems to change the spectra almost similarly and no big difference can be seen between those two. 4:1 lipid ratio of the bicelles lies between the 1:1 and 9: ratio in the SCRD spectra, which could be expected since the amount of negatively charged lipids is the double of the 1:9 ratio. If SCRD measurements could was done other protein-to-lipid ratios for example with ratios with enough 9:1 lipids like 1:500 or 1:1000, it might cause the same change in the structure as low amount of 1:1 lipids. It is clear the both liposomes and bicelles induce an effect on the secondary structure of P2wt and that the effect changes with different lipid ratio, but what really happens is not fully understood. TEM could maybe be used to study the different effects of the model membranes in more detail. TEM samples could be prepared with the same ratios used for the SCRD measurements, and maybe one could get some indication of different aggregation states or the morphology of the aggregates. Atomic force microscopy would probably also be interesting. Gaining information of the surface layers to see if something changes between the lipid compositions and between the P2wt and the mutant could be interesting information together with the SAXD data.

5.7 Bicelles induced highly ordered structures when bound to P2wt and P2 F57A

SAXD measurements were done to investigate if the myelin proteins MBP, P0ct, P2wt and the mutant P2 F57A produced bicelle and liposome aggregates with distinct repeat distances, and if there were any difference in how ordered the structures were between liposomes and bicelles. Bragg peak corresponding to a repeat distance of 7-8 nm was present in the SAXD data from MBP bound to both bicelles and liposomes. This Bragg diffraction has been observed before for the 1:100 P/L ratio (40). There is a lot of error in some of the diffraction spectra, and the reason is the large aggregates MBP forms that do not diffract very well. For correctly confirming Bragg peaks the system needs more optimization and testing several P/L ratio to see if some diffract better without large deviations. Both P2wt and P2 F57A induced bicelle aggregates with several repeat distances, indicating that highly ordered structures were induced for the highest concentration of protein and bicelles, 20 μM and 3 mM respectively (Figure 32 and Figure 33). P2wt and the mutant induced highly orders structures with the bicelles where the ordered increased with increasing concentration. This property might be due to the fact that P2 is folded and well defined, together with the cryo-EM revealing spacing between the proteins in lipid bilayers. MBP on the other hand, makes meshwork of protein in between the lipid bilayers not ordered spacing as with P2 (40), which might be physiologically relevant property where MBP keeps the membrane spacing more constant increasing the stability of the myelin sheath, while P2wt gives fluidity to the membrane and at the same time somewhat stability and compaction.

P0ct induced no aggregation with the bicelles, but induced Bragg peaks with liposomes when the protein concentration was 20 µM, corresponding to a repeat distance of around 7.6 (± 1) nm which have been seen before for the P/L ratios 1:50 and 1:100 (67). The increase in intensity of the peaks together with the shift in momentum transfer (s) is nearly linear to increase in P/L ratio, which indicates a concentration dependency in inducing ordered structures. The strong peaks in the liposomes sample indicate that there are a lot of repetitive structures and something changes with the structure since the peaks changes with P/L ratios. The shorter peak was first thought to be the second order of the first one, but unpublished data (not viewed) might reveal that this is most likely not the case with the second peak since both peaks changes with protein-to-lipid ratio and does not seem to be linked to each other. That the cytoplasmic tail of the P0 protein incudes Bragg peaks confirms that is having a lipid binding property, but exactly what these structures are is not known and needs to be studied more. The fact that P0ct did not bind bicelles might indicate that the cytoplasmic tail of P0 can stack them even if it can bind them. This might mean that bicelles have a curvature that fits poorly with P0ct. They are flat and thin while liposomes are spherical.

When looking at the repeat distances found, several of them corresponds well to repeat distances found using Cryo-EM (Figure 53 in Appendix 8.5). All proteins tested here induced repeat distances between 7-9 nm, with P2 F57A being the only one with the repeat distance up to 9 nm. It is known that P2 forms tight stacking of lipid bilayers and the 7-8 nm corresponds with a repeat distance equal to the size of the a protein bound to a lipid bilayer, which is around 8 nm, viewed in Figure 53. The repeat distance in both MBP and P0ct samples indicate that they also tightly bind lipids in the same fashion with no big difference in the repeat distance. This particular repeat distance of 7-8 nm seems to be overall a few nm shorter for the bicelle aggregates than for the liposomes independent of protein, which might indicate a tighter compaction of the bicelles. The most interesting findings were with P2wt and the mutant, where both induce highly ordered structure when binding to bicelles. The 1:150 P/L ratio both induced 6 Bragg peaks corresponding to almost identical repeat distances. Let's start with P2wt and the known repeat distances from cryo-EM. The 1:150 P/L ratio induced Bragg peaks corresponding to repeat distances from 7.3 nm to 3.5 nm. 7.3 nm is established as the repeat distance corresponding to the length of a protein bound to a bilayer. It is a little shorter than 8 nm, which might reveal that P2wt stacks bicelles tighter than liposomes. The repeat distances of 4.6 nm and 4.1 nm correspond to the distance over a single bilayer and the distance between to proteins, as viewed in Figure 53. The smallest repeat distance found with P2wt was 3.5 nm, which is exactly the diameter of the P2wt protein. The repeat distances of 7.3 nm, 4.1 nm and 3.5 nm was also seen with the mutant with same P/L ratio, so one might assume that they corresponds to the same lengths as they are identical, which probably is the case. Then, for P2wt there were two repeat distances with unknown origin, 6.5 nm and 5.2 nm respectively. These are also seen with the mutant with repeat distance of 6.6 nm and 5.2 nm. These are probably repeat distances in bicelle stacks that do not contain any protein. One of the repeat distances might be the distance over two bicelles aggregated together, but this is not known. The P2 F57A also induced a Bragg peak corresponding to the repeat distance of 10.4 nm, which was not seen in any other sample. This distance might be the distance over bicelles with proteins in between, dimeric species . From the Cryo-EM image one can see that this distance with liposomes is at 12.5 nm. If the 10.4 nm corresponds to this distance it would mean that the bicelle aggregates form tighter stacks than liposomes and decreases the repeat distance with 2.1 nm, which is a good indication of closer packing of bicelles than liposomes. The repeat distance of 7-8 nm was seen in all samples with induced Bragg peaks, but for the P2 F57A mutant this same distance was on average over 8 nm with the largest increase in the liposome samples. Previous studies of the difference between the P2wt and P2 F57A mutant have indicated some difference in vesicle aggregation kinetics and binding kinetics deduced with SPR and vesicle aggregation assays (60). The slight increase in the repeat distance for the mutant might further reveal that the Phe57 mutation causes some effect that affects the proteins interaction with the liposomes. Using TEM here would also be interesting, seeing in the Phe57 mutation maybe confirming some of the same aggregations properties to bicelles as P2wt.

5.8 TEM imaging reveals the stacking of bicelles

The get a clearer understanding of how MBP, P2wt and P0ct bind bicelles compared to liposomes, TEM imaging was done. Samples were made of bicelles and liposomes with and without protein. From the micrographs one could clearly see a difference in how MBP and P2wt binds and stacks the bicelles. MBP seems to induce strings of bicelles with MBP in between (Figure 36), while the micrograph of P2wt with bicelles revealed a more disordered stacking, as viewed in Figure 37. Aggregates of bicelles induced by MBP could only be seen in big lumps, and MBP clearly forms strings of bicelles, which might indicate that MBP fuses the bicelles together forming long strands of relative flat bilayers. Flatting of the curvature have been seen before when doing cryo-EM of MBP with liposomes (40). Together these findings support the theory that MBP forms meshworks inside lipid bilayers. The fusing of bicelles was not seen with P2wt, rather more disordered aggregates (Figure 37). The difference seen between MBP and P2wt in how they aggregate bicelles further confirms that they stack bicelles differently where MBP might have a more important function in myelination since is seems like that the protein can change the morphology of a system. P2 could be more important after myelination is completed providing support to the system only after the myelin structure if formed. The 1:100 P/L ratio of P2wt did not show excessive aggregation of liposomes, where most of the liposomes did not show any indication of protein interactions. This is very different from earlier TEM micrographs done of P2wt with DMPC:DMPG (1:1) liposomes, where there is clear aggregation and stacking of liposomes (38). In that study they used the 1:22 P/L ratio, which increases amount of protein compared to lipids, which might be the reason for not seeing similar aggregations with 1:100 P/L sample, but this ratio should be enough to cause vesicle aggregation so the poor binding seen in micrographs might be due to something else happening for example during sample preparation. Comparing the bicelles samples to the control (Figure 40), both MBP and P2wt changes the bicelle curvature into somewhat ordered protein-membrane structures, with more ordered structures formed by MBP than P2wt. The control also revealed that the bicelles had different sizes, where one bicelle had a diameter of 170 nm (not shown). This might explain the more tangled aggregation to P2wt, making it possible for the bicelles to bind to P2wt in a chaotic manner. P0ct clearly show binding to liposomes (Figure 39), but do not stack or aggregate them in the same manner like MBP and P2 (38, 40). Instead, P0ct seems to form elongated filaments of multiple liposomes without tight compaction. This P0ct behaviour is in agreement with previous studies of the 1:100 P/L ratio (69), causing similar filaments in the micrographs viewed here. It is important to remember that P0ct it only the cytoplasmic tail of the P0 protein, and that P0ct alone do not have the same properties as the protein itself, but the tail causes some form of structured membrane binding with similar properties as MBP. Comparing micrographs of the wild type proteins to point mutation linked to CMT or MS would maybe indicate some disturbed balance which can be a mechanism in the diseases. For MBP would be interesting to compare to the C8 isoform of MBP, which is found to be in increased amount in MS (79). Or point mutations in the cytoplasmic tail of P0 and the P F57A mutant, or other point mutations in P2wt linked to CMT. TEM is a nice tool to use to visualize the things observed in the other methods. T-cells could also be a constituent of the sample and see if that changes the morphology of the MBP induced aggregates.

The grids used for TEM had several problems, which made several samples impossible to investigate with the TEM microscope and photographed. Samples that were damaged were MBP and P2wt with liposomes (1:22 P/L ratio) and P0ct with bicelles. The carbon coated copper-grids had a thin membrane film applied before glow-discharging. One theory for the problems is that the glow-discharging somehow damaged or dried out the membrane, so when the electron beam hit the sample, the membrane was to fragile and cracked causing the grids to become useless. Therefore, the last samples were the control with only bicelles (Figure 40) with and without glow-discharging, to see if TEM microscopy could be conducted without glow-discharging the grids. The top micrographs viewed in Figure 40 were without glow-discharge and clearly indicated that the sample can be investigated. The grid with the liposome control was also damaged. And due to little time no further sample preparations were done.

5.9 Discussion summary

None of the myelin protein studied in this thesis indicated binding to either of the lipid coated Fe_3O_4 and SiO_2 nanoparticles. As thiol functionalization of AuNPs is a common method to further coated them with lipids, three protocols for lipid coating and thiol-functionalization were modified and tested in this thesis. Induced colour changes by MBP together with the UV-vis spectra and TEM indicated partial coating of the nanoparticles, but it was clear from this pilot study that the protocol needs more optimization to get a complete lipid coat of each membrane without aggregation. Future research on this would be to continue the optimization of the thiol-functionalized gold nanoparticles and at the same time try the EDC-NHS protocol, to compare the results and see if one is easier to implement. One could also try to make the gold nanoparticles themselves. Then difference sizes of nanoparticles can be tested to see if a size works better with the specific myelin protein than others and one could try to coat with different lipid composition and ratios to check for variability. Optimization of how to functionalize nanoparticles in the best possible way is needed to get further with using nanoparticles in the study of the myelin sheath.

Further investigation of protein-lipid interactions revealed that P0ct seems to favour saturated lipid mixtures over unsaturated ones with the need of higher lipid concentrations of DOPC:DOPS when testing different protein to lipid ratios. This hypothesis has been deduced before and this experiment was a profound conformation of this assumption (69).

As expressed in the introduction, liposomes have been used for several years as a model mimicking the lipid bilayers in the myelin sheath. Bicelles is becoming more popular as a model and several methods were used to combine exploration of both protein-membrane interactions and to look at possible differences between the two model membranes. Turbidimetry assays provided data about the proteolipid aggregate stability when myelin proteins were mixed with either bicelles or liposomes. The delayed aggregation of bicelles seen with P2 and MBP might be a function of the flat bicelle form. Several turbidity measurements could be conducted to see if these patterns continued to appear. If these revealed similar results, one could study vesicle aggregation from begging to the end, literally. A problem with turbidimetry is that the samples starts to aggregates from the minute the proteins are applied to the lipids, which mean if one have several sample the first sample might be done with the aggregation before the last samples. If bicelles delays this then one could also watch the formation of the vesicle aggregates that might give some new information about how fast the myelin proteins forms aggregates. Turbidity measurements also indicated that P0ct don't bind very well to the bicelles. This can be due to the bicelle form, even though they resembles very well the lipid bilayers found in myelin, the function of the cytoplasmic tail is not yet understood although it is known to have lipid binding properties, which further SAXD and TEM indicates, P0ct bound to the liposomes in SAXD but not to the bicelles. One could postulate that bicelles works very well as model membranes for

MBP and P2wt as confirmed with turbidity and TEM. SAXD revealed that bicelles work especially well for P2wt and the mutant when studying repeat distances in aggregates. 6 peaks were found in both P2wt and P2 F57A where several of the repeat distances do not correspond to any distances found before with cryo-EM, this indicates something special for the bicelle aggregates.

SCRD measurements revealed that the secondary structure of P2wt changes in contact with both bicelles and liposomes. Increased change in the SCRD spectra was seen with decrease in lipid ratio, with 9:1 lipid ratio in bicelles induced least change. Apart from that, no big difference could be seen comparing bicelles to liposomes. TEM could maybe be used to study the different effect of the model membranes. TEM samples could be prepared with the same ratios used for the SCRD measurements, and maybe one could get some indication of different aggregation state or the morphology of the aggregates.

TEM imaging was the last method used during this thesis to visualize the protein-membrane interactions investigated in experiments used. A lot of problems occurred due to the glow-discharging. Control of the bicelles indicated that glow-discharging might not be needed for biological samples. This have to tested with protein-lipid samples to check if the same structures can be seen without glow-discharging. If so, then it will not be necessary to that step and maybe the membranes on the grids are more stable making it easier to investigate the samples.

6 Conclusion and future research

MBP, P2wt and P0 are important proteins with distinct properties to hold and compact the lipid bilayers in the myelin sheath giving it its insulation properties that facilitates rapid signal conduction in the nervous system. Disturbed myelin homeostasis or point mutation can lead to demyelinating diseases like MS and CMT. To understand disease etiology and how to possibly treat these disease one first have to understand the functions of the involved proteins and how they interaction with lipid bilayers by using membrane-mimics.

Protein interactions with the two different lipid membrane-mimics were studied with many different techniques. Turbidity proved to be a simple way of obtaining information about how the protein induced aggregation of the different models indicating lagged aggregation of the bicelles mixed with MBP and P2wt. MBP induced the same pattern with higher concentration, Pwt and P0ct did not. This have to be further studied to confirm the findings from this thesis and to check reproducibility of the samples. Changes in the secondary structure of P2wt were indicated by the SCRD measurements, but no big difference could be seen between the bicelles and liposomes. To further study the interactions one could conduct thermal stability measurements of the proteins when bound to liposomes and bicelles to see if the form of the membrane-mimics induce some unique effect that can be attributed to the difference of the curvature. Collected SAXD data revealed highly ordered structure of the P2wt and mutant, which is very interesting to study in the future with several methods like thermal stability and differential scanning calorimetry to see if the phase transition temperature differ between the membranes, but also if the bicelles increases or decreases the Tm compared to liposomes. Variation size of the bicelles could also be examined to see if there are minimal size required to induce aggregation. TEM confirmed a difference between bicelle aggregates induced by MBP and P2wt, where MBP formed fused ordered structure while P2wt induced random aggregates. This might reveal an important contrast in the properties of the two myelin proteins in how they affect stacking of bilayers. Cryo-EM would be interesting to use in the future to study the differences caused by the two membrane-mimics. Cryo-EM could reveal something about how the proteins resides in the bicelle aggregates and take a closer look on how the aggregates themselves look like, maybe some distances could be deduced that fits the repeat distances found with SAXD. P0ct does not seem to bind bicelles as well as liposomes. This could signify that bicelles are not a good model to use when studying P0ct, but it might work better with the full-length P0.

The pilot study with the nanoparticles revealed that the gold nanoparticles had some form of coating, indicating a partial coating of the nanoparticles. The coating protocols used here needs modifications to work and one could also try EDC-NHS coupling of carboxyl groups instead of thiol functionalization to see if that works better. Maybe different lipid mixture works better than the one used here. MBP protein with a His-tag will bind gold nanoparticles and this can be used in TEM to visualize where MBP resides in lipid aggregates. It would be interesting to examine this in relation to the fused bicelle strings. SPR could also be conducted with bicelles vs. liposomes and eventually with gold nanoparticles if lipid coating works successfully.

Further research is necessary to get a deeper understanding of how these proteins interaction with lipid membranes. A next step could be to examine the proteins together and not separate, since they operate together in native myelin. Bicelles seem to work as an equally good model membrane as liposomes and in some experiments, like SAXD, works better resembling the native lipid bilayers. It would be appealing to test bicelles of other proteins mixture, like adding cholesterol or other lipids found in the myelin. The changes would maybe reveal something new about the protein-membrane interactions induced by the different myelin proteins. The lipid coated gold nanoparticles need more optimization before investigating them together with myelin proteins and lipid bilayers.

7 References

1. Yang JA, Murphy JC. Evidence for patchy lipid layers on gold nanoparticle surfaces. Langmuir. 2012;28(12):5404−16.

2. Organization WH. Atlas: Multiple Sclerosis Resources in the World 2008 2008. p. 14.

3. Kedlaya D. Physical medicine and rehabilitation for Charcot-Marie-Tooth diease 2016 [updated 2016-01-07; cited 2017 10-23]. Available from: https://emedicine.medscape.com/article/315260-overview#a6.

4. Leray E, Moreau T, Fromont A, Edan G. Epidemiology of multiple sclerosis. Revue neurologique. 2016;172(1):3-13.

5. Tullman MJ. Overview of the Epidemiology, Diagnosis, and Disease Progression Associated With Multiple Sclerosis. The american journal of managed care. 2013;19(2):15-20.

6. Milo R, Kahana E. Multiple sclerosis: Geoepidemiology, genetics and the environment. Autoimmunity reviews. 2010;9(5):A387-A94.

7. Morell P, Quarles HR. Basic Neurochemistry: Molecular, Cellular and Medical Aspects: The Myelin Sheath: Myelin facilitates conduction NCBI1999 [cited 2017 09-26]. 6th:[Available from: https://www.ncbi.nlm.nih.gov/books/NBK27954/.

8. Health P, Online IH. How does the nervous system work? [updated August 19, 2016; cited 2017- 09-28]. Available from: https://www.ncbi.nlm.nih.gov/pubmedhealth/PMH0072574/.

9. Purves D, Augustine GJ, Fitzpatrick D, al. e, editors. Neuroscience. 2nd eidition: Sunderland (MA): Sinauer Associates; 2001.

10. Suzuki N, Sekimoto K, Hayashi C, Mabuchi Y, Nakamura T, Akazawa C. Differentiation of Oligodendrocyte Precursor Cells from Sox10-Venus Mice to Oligodendrocytes and Astrocytes. Scientific Reports. 2017;7(1):14133.

11. Susuki K. Myelin: A specialized membran for cell communication Nature Education2010 [cited 2017 10-06]. Available from: https://www.nature.com/scitable/topicpage/myelin-a-specialized-membrane-for-cell-communication-14367205.

12. Knowles L. The evolution of myelin: Theories and application to human disease. Journal of Evolutionary Medicine. 2017;5:23.

13. Squire LR, Bloom FE, Spitzer NC, du Lac S, Gosh A, Berg D. Fundamental Neuroscience, 3rd edition: Elsevier Inc. ; 2008.

14. Salzer JL. Schwann cell myelination2015 08-07 [cited 2017- 09-26]. Available from: https://www.ncbi.nlm.nih.gov/pmc/articles/PMC4526746/.

15. Byrne JH. Ionic mechanisms of action potentials Neuroscience online [cited 2017 10-08]. Available from: http://nba.uth.tmc.edu/neuroscience/m/s1/chapter02.html.

16. Nave K, Werner HB. Myelination of the nervous system: mechanisms and functions. Annual review of cell and developmental biology. 2014;30:503-33.

17. Nave K. Myelination and support of axonal integrity by glia. Nature. 2010;468:244-52.

18. Aggarwal S, Yurlova L, Simons M. Central nervous system myelin: structure, synthesis and assembly. Trends in cell biology. 2011;21(10):585-93.

19. Boiko T, Winckler B. Myelin under construction - teamwork required. The journal of cell biology. 2006;172(6):799-801.

20. Tricaud N, Perrin-Tricaud C, Brusés JL, Rutishauser U. Adherens junctions in myelinating Schwann cells stabilize Schmidt-Lanterman incisures via recruitment of p120 Catening to E-cadherin. Journal of Neuroscience. 2005;25(13):3259-69.

21. Salzer JL. Polarized Domains of Myelinated Axons. Neuron. 2003;40(2):297-318.

22. Vassall KA, Bamm VV, Harauz G. MyelStones: the executive roles of myelin basic protein in myelin assembly and destabilization in multiple sclerosis. Biochemical Journal. 2015(472):17-32.

23. Morell P, Quarles RH. Basic Neurochemistry: Molecular, cellular and medical aspects: Charachteristic composition of myelin, Table 4-1 NCBI1999 [cited 2017 09-26]. Available from: https://www.ncbi.nlm.nih.gov/books/NBK28221/.

24. Podbielska M, Levery SB, Hogan EL. The structural and functional role of myelin fast-migrating cerebrosides: pathological importance in multiple sclerosis 2011 [cited 2017 10-06]. Available from: https://www.ncbi.nlm.nih.gov/pmc/articles/PMC3373471/.

25. Schmitt S, Castelvetri LC, Simons M. Metabolism and functions of lipids in myelin. Biochimica et Biophysica Acta - molecular and cell biology of lipids. 2014;1851(8):999-1005.

26. Wallner S, Schmitz G. Plasmalogens the neglected regulatory and scavenging lipid species. Chemistry and physics of lipids. 2011;164(6):573-89.

27. Kiessling V, Wan C, Tamm LK. Domain coupling in asymmetric lipid bilayers. Biochimica et Biophysica Acta (BBA) - Biomembranes. 2009;1788(1):64-71.

28. Kranenburg M, Smit B. Phase bihavior of model lipid bilayers. Journal of physical chemistry. 2005;109(14):6553-63.

29. Shaharabani R, Ram-On M, Avinery R, Aharoni R, Amon R, Talmon Y, et al. Structural transition in myelin membrane as initiator of multiple sclerosis. Journal of the American Chemical Society. 2016(138):12159-65.

30. Charst R, Saher G, Klaus-Armin N, Verheijen MH. Lipid metabolism in myelinating glial cells: lessons from human inherited disorders and mouse models. Journal of lipid research. 2010;52:419-34.

31. Deber MC, Reynolds JS. Central nervous system myelin: structure, function and pathology. Clinical Biochemistry.24(2):113-34.

32. Barkovich AJ. Concepts of Myelin and Myelination in Neuroradiology2000 [cited 2017 09-29]; (29):[1099-109 pp.]. Available from: http://www.ajnr.org/content/ajnr/21/6/1099.full.pdf.

33. Juurlink BHJ, Devon RM, Doucette JR, Nazarali AJ, Schreyer DJ, Verge VMK. Cell biology and pathology of myelin: Evolving biological concepts and therapeutic approaches: Plenum; 1997.

34. Peschl P, Bradl M, Höftberger R, Berger T, Reindl M. Myelin oligodendrocyte glycoprotein: decipering a target in inflammatory demyelinating diseases. Fronties in immunology. 2017;8(529).

35. Dyer CA, Hickey WF, Geisert EEj. Myelin/oligodendrocyte-specific protein: a novel surface membrane protein that associates with microtubules. Journal of neuroscience research. 1991;28(4):607-13.

36. Uniprot. Myelin protein P0, MYP0_HUMAN [updated 2017-08-30; cited 2017 09-27]. Available from: http://www.uniprot.org/uniprot/P25189.

37. Rossor AM, Polke JM, Houlden H, Reilly MM. Clinical implications of genetic advances in Charcot-Marie-Tooth disease. Nature reviews Neurology. 2013(9):562-671.

38. Ruskamo S, Nieminen T, Kristiansen CK, Vatne GH, Baumann A, Hallin EI, et al. Molecular mechanisms of Charcot-Marie-Tooth neuropathy linked to mutations in human myelin protein P2. Sci Rep. 2017;7(1):6510.

39. Nave KA, Werner HB. Myelination of the nervous system: mechanisms and functions. Annu Rev Cell Dev Biol. 2014;30(1):503-33.

40. Raasakka A, Ruskamo S, Kowal J, Barker R, Baumann A, Martel A, et al. Membrane Association Landscape of Myelin Basic Protein Portrays Formation of the Myelin Major Dense line. nature. 2017.

41. Smith-Slatas C, Barbarese E. Myelin basic protein gene dosage effect in the PNS. Molecular and cellular neuroscience. 1999;15(4):343-54.

42. Pritzker L, Joshi S, Gowan J, Harauz G, Moscarello M. Deimination of myelin basic protein. 1. Effect of deimination of arginyl residues of myelin basic protein on its structure and susceptibility to digestion by cathepsin D. Biochemistry. 2000(39):5374-81.

43. Givogri MI, Bongarzone ER, Schonmann V. Expression and regulation of Golli products of Myelin Basic Protein Gene during in vitro development of Oligodendrocytes. Journal of neuroscience research. 2001;66:679-90.

44. Siu CR, Balsor JL, Jones DG, Murphy KM. Classic and Golli Myelin Basic Protein have disting developmental trajectories in human visual cortex. Fronties in Neuroscience. 2015;9(138).

45. Smith GS, Homchaudhrue L, Boggs JM, Harauz G. Classic 18.5- and 21.5-kDa myelin basic protein isoforms associate with cytoskeletal and SH3-domain proteins in the immortalized N19-oligodendroglial cell line stimulated by phorbol ester and IGF-1. Neurochemical Research. 2012;37(6):1277-95.

46. Atkins CM, Yon M, Groome NP, Sweatt JD. Regulation of myelin basic protein phosphorylation by mitogen-activated protein kinase during increased action potential firing in the hippocampus. Journal of Neurochemistry. 1999;73(3):1090-7.

47. Boggs JM, Rangaraj G, Heng YM, Liu Y, Harauz G. Myelin basic protein binds microtubules to a membrane surface and to actin filaments in vitro: effect of phosphorylation and deimination. Biochimica et Biophysica Acta. 2011;1808(3):761-73.

48. Libich DS, Harauz G. Interactions of the 18.5 kDa isoform of myelin basic protein with Ca2+-calmodulin: in vitro studies using gel shift assays. Molecular and cellular biochemistry. 2002;241(1-2):45-52.

49. Dobrowolski Z, Barylko B, Drabikowski W. Interaction of tropomyosin with myelin basic protein and its effect on the ATPase activity of actomyosin. European journal of cell biology. 1986;41(1):65-71.

50. Aggarwal S, Snaidero N, Pähler G, Frey S, Sánches P, Zweckstetter M, et al. Myelin Membrane Assembly Is Driven by a Phase Transition of Myelin Basic Proteins Into a Cohesive Protein Meshwork. PLoS Biology. 2013;11(6):e1001577.

51. Veerkamp J, Maatman R. Cytoplasmic fatty acid-binding proteins: Their structure and genes. Progress in Lipid Research. 1995(34):17-52.

52. Majava V, Polverini E, Mazzini A, Nanekar R, Knoll W, Peters J, et al. Structural and functional characterization of human peripheral nervous system myelin protein P2. PLoS One. 2010;5(4):e10300.

53. Ruskamo S, Yadav RP, Sharma S, Lehtimäki M, Laulumaa S, al e. Atomic resolution view into the structure-function relationships of the human myelin pheripheral membrane protein P2. Acta Crystallographica Section D Biological crystallpgraphy. 2014(70):165-76.

54. Zenker J, Stettner M, Ruskamo S, Domènech-Estévez E, Baloui H, Médard J, et al. A role of peripheral myelin protein 2 in lipid homeostasis of myelinating Schwann cells,. Glia. 2014;62(9):1502-12.

55. Furuhashi M, Hotamisligil GS. Fatty acid-binding proteins: role in metabolic diseases and potential as drug targets. Nature reviews Drug discovery. 2010;7(6):489-503.

56. Kursula P. Structural properties of proteins specific to the myelin sheath. Amino Acids. 2006;34:175-85.

57. Hong YB, Joo J, Hyun YS, Kwak G, Choi B, Yeo HK, et al. A mutation in PMP2 causes dominant demyelinating Charcot-Marie-Tooth Neuropathy 2016 [cited 2017 10-03]. Available from: https://www.ncbi.nlm.nih.gov/pmc/articles/PMC4735456/.

58. Sheremata W, Colby S, Karkhanis Y, Eylar EH. Cellular hypersensitivity to basic myelin (P2) protein in the Guillain-Barré snydrome. The canadian journal of nerurological sciences 1975;2(2):87-90.

59. Khalili-Shirazi A, Atkinson P, Gregson N, Hughes RAC. Antibody responses to P0 and P2 myelin proteins in Guillain-Barré syndrome and chronic idiopathic demyelinating polyradiculoneuropathy. Journal of Neuroimmunology. 1993;46(1-2):245-51.

60. Laulumaa S, Nieminen T, Raasakka A, Krokengen OC, Safaryan A, Hallin EI, et al. Structure and dynamics of a human myelin protein P2 portal region mutant indicate opening of the β barrel in fatty acid binding protein. BMC Structural biology. 2018;18(1).

61. Simpson MA, Bernhlor DA. analysis of a series of phenylalanine 57 mutants of the adipocyte lipid-binding protein. Biochemistry. 1998;37:10980-6.

62. Fratta P, Ornaghi F, Dati G, Zambroni D, Savari P, Belin S, et al. A nonsense mutation in myelin protein zero causes congential hypomyelination neuropathy through altered P0 membrane targeting and gain abnormal function. BioRxiv. 2018.

63. D'Urso D, Ehrhardt P, Müller HW. Peripheral myelin protein 22 and protein zero: a novel association in peripheral nervous system myelin. Journal of neurosciences. 19999;19(9):3395-403.

64. Garver LS, Xi Z, Dimopoulos G. immunoglobulin superfamily members play an important role in the mosquito immune system. Developmental & Comarative immunology. 2008;32(5):519-51.

65. Williams AF, Barclay AN. The immunoglobulin superfamily - domains for cell surface recognition. Annual review of immunology. 1988;6:381-405.

66. Zhang K, Filbin MT. Formation of a disulfide bond in the immunoglobulin domain of the myelin P0 protein is essential for its adhesion. Journal of Neurochemistry. 1994;63(1):367-70.

67. Raasakka A, Ruskamo S, Kowal J, Han H, Baumann A, Myllykoski M, et al. Molecular structure and function of myelin protein P0 in membrane stacking. BioRxiv. 2018.

68. Shapiro L, Doyle JP, Hensley P, Colman DR, Hendrickson WA. Crystal structure of the extracellular domain from P0, the major structural protein of peripheral nerve myelin. Neuron. 1996;17(3):435-49.

69. Raasakka A, Ruskamo S, Kowal J, Han H, Baumann A, Myllykoski M, et al. Molecular structure and function of myelin protein P0 in membrane stacking. BioRxiv. 2018.

70. Wong M-H, Filbin MT. The cytoplasmic domain of the myelin P0 protein influences the adhesive interaction of its extracellular domain. journal of Cell biology. 1994;126(4):1089-97.

71. Levin MC. Overview of demyelinating disorders MERCK MANUAL [updated 2017-08; cited 2017 09-29]. Available from: http://www.merckmanuals.com/professional/neurologic-disorders/demyelinating-disorders/overview-of-demyelinating-disorders.

72. Steinman L. Antigen-specific therapy of multiple sclerosis: The long-sought magic bullet. Neurotherapeutics 2007;4(4):661-5.

73. Shivane AG, Chakrabarty A. Multiple sclerosis and demyelination. Current Diagnostic Pathology. 2007;13(3):193-202.

74. Nielsen NM, Westergaard T, Rostgaard K, Frisch M, Hjalgrim H, Wohlfahrt J, et al. Familial risk of multiple sclerosis: a nationwide cohort study 2005 [cited 2017 10-01]. Available from: https://www.ncbi.nlm.nih.gov/pubmed/16120694.

75. Spain R. Determination of multiple sclerosis subtypes U.S department of veterans affairs2018 [updated 2018-08-03. Available from: https://www.va.gov/MS/Professionals/Diagnosis/Determination_of_MS_Subtypes.asp.

76. Brück W, Porada P, Poser S, Rieckmann P, Hanefeld F, Kretzschmar HA, et al. Monocyte/macrophage differentiation in early multiple sclerosis lesions. Annals of neurology. 1995;38(5):788-96.

77. Chu F, Shi M, Zheng C, Shen D, Zhu J, Zheng X, et al. The roles of macrophages and microglia in multiple sclerosis and experimental autoimmune encephalomyelitis. Journal of Neuroimmunology. 2018;318:1-7.

78. Rawji KS, Yong VW. The benefits and detriments of macrophages/microglia in models of multiple sclerosis. Clinical & developmental immunology. 2013;2013.

79. Tranquill LR, Cao L, Ling NC, Kalbacher H, Martin RM, Whiteaker JN. Enhanced T cell responsiveness to citrulline-containing myelin basic protein in multiple sclerosis patients. Multiple sclerosis journal. 2000;6:220-5.

80. Wang C, Neugebauer U, Bürck J, Myllykoski M, Baumgärtel P, Popp J, et al. Charge isomers of myelin basic protein: structure and interactions with membranes, nucleotide analogues, and calmodulin. PLoS One. 2011;6(5).

81. Moscarello MA, Wood DD, Ackerley C, Boulias C. Myelin in multiple sclerosis is developmentally immature. Journal of clinical investigation. 1994;94(1):146-54.

82. Niemann A, Berger P, Suter U. Pathomechanisms of Mutant Proteins in Charcot-Marie-Tooth Disease. NeuroMolecular Medicine. 2006;8.

83. Ruskamo S, Nieminen T, Kristiansen CK, Vatne GH, Baumann A, Hallin EI, et al. Molecular mechanisms of Charcot-Marie-Tooth neuropathy linked to mutations in human myelin protein P2 2017 [updated 2017-07-26; cited 2017 10-01]. Available from: https://www.ncbi.nlm.nih.gov/pmc/articles/PMC5529448/.

84. Senderek J, Hermanns B, Lehmann U, Bergmann C, Marx G, Kabus C, et al. Charcot-Marie-Tooth Neuropathy Type 2 and P0 Point Mutations: Two Novel Amino Acid Substitutions (Asp61Gly; Tyr119Cys) and a Possible “Hotspot” on Thr124Met. Brain Pathology. 2006;10(2).

85. Warner LE, Hilz MJ, Appel SH, Killian JM, Kolodny EH, Karpati G, et al. Clinical Phenotypes of Different MPZ (P0) Mutations May Include Charcot–Marie–Tooth Type 1B, Dejerine–Sottas, and Congenital Hypomyelination. Neuron. 1996;17(3):451-60.

86. Shy M, Jáni A, Krajewski K, Grandis M, Lewis RA, Shy RR, et al. Phenotypic clustering in MPZ mutations. Brain. 2004;127(2):371-84.

87. Giese KP, Martini R, Lemke G, Soriano P, Schachner M. Mouse PO Gene Disruption Leads to Hypomyelination, Abnormal Expression of Recognition Molecules, and Degeneration of Myelin and Axonss. Cell. 1992;71(4):565-76.

88. Wilson R, Tocher DR. Lipid and fatty acid composition is altered in plaque tissue from multiple sclerosis brain compared with normal brain white matter. Lipids. 1991;26(1):9-15.

89. Fledrich R, Abdelaal T, Rasch L, Bansal V, Schütza V, Brügger B, et al. Targeting myelin lipid metabolism as a potential therapeutic strategy in a model of CMT1A neuropathy. Nature Communications. 2018;9.

90. Yao JK, Dyck PJ. Lipid abnormalities in hereditary neuropathy. Journal of the neurological sciences. 1981;52(2-3):179-90.

91. Handy J. How big is a nanometer? Forbes.com2011 [updated Dec 14, 2011; cited 2018 08.31]. Available from: https://www.forbes.com/sites/jimhandy/2011/12/14/how-big-is-a-nanometer/#5621f6ed6fb0.

92. Erickson HP. Size and Shape of Protein Molecules at the Nanometer Level Determined by Sedimentation, Gel Filtration, and Electron Microscopy. Biological procedures online. 2009;11:32-51.

93. Khan I, Saeed K, Khan I. Nanoparticles: Properties, applications and toxicities. Arabian journal of chemistry. 2017.

94. model system. Medical dictionary.

95. Akbarzadeh A, Rezaei-Sadabady R, Davaran S, Joo SW, Zarghami N, al. e. Liposome: classification, preparation and application. Nanoscale research letters. 2013;8(1):102.

96. Sharma A, Sharma US. Liposomes in drug delivery: progress and limitations. International journal of pharmaceutics. 1997;154.

97. Sanders CR, Prosser RS. bicelles: a model membran system for all seasons? Structure. 1998;6(10):1227-34.

98. Dürr UHN, Gildenberg M, Ramamoorthy A. The magic of bicelles light of membrane protein structure. Chemical reviews. 2012;112(11):6054-74.

99. Piai A, Fu Q, Dev J, Chou JJ. Optimal bicelle q for solution NMR studies of protein transmembrane partition. Chemistry. 2017;23(6):1361-7.

100. Chen Q, Zhuant T, Vishnivetskiy SA, Cho M. The Rhodopsin-Arrestin-1 interaction in bicelles. Methods in molecular biology. 2015;1271:77-95.

101. lipids AP. Phase transition temperature for glycerophospholipis Avanti polar lipids [Available from: https://avantilipids.com/tech-support/physical-properties/phase-transition-temps/.

102. Suri SS, Fenniri H, Sing B. Nanotechnology-based drug delivery systems. Journal of occupational medicine and toxicology. 2007;2:16.

103. Lin MM, Kim H, Kim H, Muhammed M, Kim D. Iron oxide-based nanomagnets in nanomedicine: fabrication and applications. Nano reviews. 2010;1(10).

104. Mikhaylova M, Kim DK, Bobrysheva N, Osmolowsky M, Semenov V, Tsakalakos T, et al. Superparamagnetism of Magnetite Nanoparticles: Dependence on Surface Modification. Langmuir. 2004;20(6):2472-7.

105. Binns C. Introduction to nanoscience and nanotechnology: Wiley; 2010.

106. Wahajuddin, Arora S. Superparamagnetic iron oxide nanoparticles: magnetic nanoplatforms as drug carriers. International journal of nanomedicine. 2012;7:3445-71.

107. Wang YJ. Superparamagnetic iron oxide based MRI contrast agents: Current status of clinical application. Quantitative imaging in medicine and surgery. 2011;1(1):35-40.

108. Hussain SM, Hess KL, Gearhart JM, Geiss KT, Schlager JJ. In vitro toxicity of nanoparticles in BRL 3A rat liver cells. Toxicology in vitro. 2005;19(7):975-83.

109. Karlsson HL, Gustafsson J, Cronholm P, Möller L. Size-dependent toxicity of metal oxide particles--a comparison between nano- and micrometer size. Toxicology letters. 2009;188(2):112-8.

110. Cromer SMB, Kshitiz, Wang CJ, Orukari I, Levenchenko A, Bulte JW, et al. Cell motility of neural stem cells is reduced after SPIO-labeling, which is mitigated after exocytosis. Magnetic resonance in medicine. 2013;69(1):255-62.

111. Liu Y, Xia Q, Liu Y, Zhang S, Cheng F, Zhong Z, et al. Genotoxicity assessment of magnetic iron oxide nanoparticles with different particle sizes and surface coatings. Nanotechnology. 2014;25(42).

112. Soenen SJH, Himmelreich U, Nuytten N, Cuyper MD. Cytotoxic effects of iron oxide nanoparticles and implications for safety in cell labelling. Biomaterials. 2011;32(1):195-205.

113. Martin KR. The chemistry of silica and its potential health benefits. The journal of nutrition, health & aging. 2007;11(2):94-7.

114. Tallury P, Payton K, Santra S. Silica-based multimodal/multifunctional nanoparticles for bioimaging and biosensing applications. Nanomedicine. 2008;3(4):579-92.

115. Vivero-Escoto JL, Slowing II, Trewyn BG, Lin VSY. Mesoporous silica nanoparticles for intracellular controlled drug delivery. Small. 2010;6(18).

116. Chu Z, Huang Y, Tao Q, Li Q. Cellular uptake, evolution, and excretion of silica nanoparticles in human cells. Nanoscale. 2011;3:3291-9.

117. Sun D, Gong L, Xie J, Gu X, Li Y, Cao Q, et al. Toxicity of silicon dioxide nanoparticles with varying sizes on the cornea and protein corona as a strategy for therapy. Science bulletin. 2018;63(14):907-16.

118. Murugadoss S, Lison D, Godderis L, Van Den Brule S, Mast J, Brassienne F, et al. Toxicology of silica nanoparticles: an update. Archives of toxicology. 2017;91(9):2967-3010.

119. Cartwright M. Gold in antiquity. Gold in antiquity. Ancient history encyclopedia2014.

120. Dykman LA, Khlebtsov NG. Gold Nanoparticles in Biology and Medicine: Recent Advances and Prospects ActaNaturae. 2011;3(2):34-55.

121. Gerber A, Bundschuh M, Klingelhofer D, Groneberg D. Gold nanoparticles: recent aspects for human toxicology. Journal of occupational medicine and toxicology. 2013;8(32).

122. Amendola V, Meneghtti M, Stener M, Guo Y, Chen S, Crespo P, et al. Physico-Chemical Characteristics of Gold Nanoparticles. Gold Nanoparticles in analytical chemistry: Elsevier B. V; 2014.

123. Amendola V, Pilot R, Frasconi M, Maragò OM, Latì MA. Surface plasmon resonance in gold nanoparticles: a review. Journal of physics: condensed matter. 2017;29(20).

124. He YQ, Liu SP, Kong L, Liu ZF. A study on the sizes and concentrations of gold nanoparticles by spectra of absorption, resonance, Rayleigh scattering and resonance non-linear scattering. Spectrochimica Acta. 2005;61(13-14):2861-6.

125. Reusch W. Visible and Ultraviolet Spectroscopy IOCD2013 [updated 2013-05-05; cited 2018-11-10]. Available from: https://www2.chemistry.msu.edu/faculty/reusch/virttxtjml/spectrpy/uv-vis/spectrum.htm.

126. El-Brolossy T, Mohamed MB, Abdallah T, Abdallah S, al. e. Shape and size dependence of the surface plasmon resonance of gold nanoparticles studied by Photoacoustic technique. The European Physical Journal Special Topics. 2008;153:361-4.

127. Nealon GL, Donnio B, Greget R, Kappler J-P, Terazzi E, Gallani J-L. Magnetism in gold nanoparticles. Nanoscale. 2012;4(12):5244-58.

128. Lermé J, Baida H, Bonnet C, Broyer M, Cottancin E, Crut A, et al. Size Dependence of the Surface Plasmon Resonance
Damping in Metal Nanospheres. The journal of physical chemistry letters. 2010;1(19):2922-8.

129. Chen Y, Xianyu Y, Jiang X. Surface modification of gold nanoparticles with small molecules for biochemical analysis. Accounts for chemical research. 2017;50:310-9.

130. Love JC, Estroff LA, Kriebel JK, Nuzzo RG, Whitesides GM. Self-assembled monolayers of thiolates on metals as a form of nanotechnology. Chemical reviews. 2005;105(4):1103-70.

131. Schreiber F. Structure and growth of self-assembling monolayers. Progress in surface science. 2000;65(5-8):151-7.

132. Park J, Shumaker-Parry JS. Strong Resistance of Citrate Anions on Metal Nanoparticles to Desorption under Thiol Functionalization. ACS Nano. 2015;9(2):1665-82.

133. Nam J, Kim Y, Kang A, Kim K, Lee K, Yun WS, et al. Lipid Reconstitution-Enabled Formation of Gold Nanoparticle Clusters for Mimetic Cellular Membrane. journal of nanomaterials. 2016;2016:7.

134. Hamilton DJ, Coffman MD, Knight JD, Reed SM. Lipid-Coated Gold Nanoparticles and FRET Allow Sensitive
Monitoring of Liposome Clustering Mediated by the
Synaptotagmin7 C2A Domain. ACS Publications. 2017;33:9222-30.

135. Chan YM, Boxer SG. Model Membrane Systems and Their Applications. Current opinion in chemical biology. 2008;11(6):581-7.

136. Ignazio SM. Physico-chemical characterization of model biomembranes
and their interaction with potential therapeutic peptides. fedoa.uint.it: University of Naples "Federico II"; 2016.

137. Daneman R, Prat A. The blood-brain barrier. Cold Spring Harbor Perspectives in Biology. 2015;7(1).

138. Zhou Y, Peng Z, Seven ES, Leblanc RM. Crossing the blood-brain barrier with nanoparticles. Journal of controlled release. 2018;270:290-303.

139. Rajeshkumar S, Naik P. Synthesis and biomedical applications of Cerium oxide nanoparticles – A Review. Biotechnology reports. 2018;17:1-5.

140. Heckman KL, DeCoteau W, Estevez A, Reed KJ, Costanzo W, Sandford D, et al. Custom cerium oxide nanoparticles protect against a free radical mediated autoimmune degenerative disease in the brain. ACS Nano. 2013;7(12):10582-96.

141. Lasagna-Reeves C, Gonzalez-Romero D, Barria MA, Olmedo I, Clos A, Sadagopa VMR, et al. Bioaccumulation and toxicity of gold nanoparticles after repeated administration in mice. Biochemical and biophysical research communications. 2010;393(4):649-55.

142. Gao N, Sun H, Dong K, Ren, Qu X. Gold-nanoparticle-based multifunctional amyloid-β inhibitor against Alzheimer's disease. Chemistry. 2015;21(2):829-35.

143. Hong S, Choi I, Lee S, Yang YI, Kang T, Yi J. Sensitive and colorimetric detection of the structural evolution of superoxide dismutase with gold nanoparticles. Analytical chemistry. 2009;81(4):1378-82.

144. Lopes CDF, Gonçalves NP, Gomes CP, Saraiva MJ, Pêgo P. BDNF gene delivery mediated by neuron-targeted nanoparticles is neuroprotective in peripheral nerve injury. Biomaterials. 2017;121:83-96.

145. Lohmüller T, Triffo S, O'Donoghue G, Xu Q, Coyle MP, Groves JT. Supported membranes embedded with fixed arrays of Gold nanopartcles. Nano letters. 2011(11).

146. Wu H-J, Henzie J, Lin W-C, Rhodes C, Li Z, Sartorel E, et al. Membrane-protein binding measured with solution-phase plasmonic nanocube sensors Nature Methods. 2012(9):1189-91.

147. Lohmüller T, Iversen L, Schmidt M, Rhodes C, Tu H-L, Lin W-C, et al. Single Molecule Tracking on supported membranes with arrays of optical nanoantennas. Nano letters. 2012(12):1717-21.

148. Beales PA, Bergstrom CL, Geerts N, Groves JT, Vanderlick TK. Single vesicle observations of the cardiolipin - Cytochrome c interaction: induction of membrane morphology changes. Langmuir. 2011(27):6107-15.

149. Rozovsky S, Forstner MB, Sondermann H, Groves JT. Single molecule kinetics of ENTH binding to lipid membranes. Physical chemistry. 2012(116):5122-31.

150. Laemmli UK. Cleavage of Structural Proteins during the Assembly of the Head of Bacteriophage T4. Nature. 1970;227:680.

151. Park Jong-Won, Jennifer S-PS. Strong Resistance of Citrate Anions on Metal Nanoparticles to Desorption under Thiol Functionalization. ACS Nano. 2015;9(2):1665–82.

152. Franke D, Petoukhow MV, Konarev PV, Panjkovich A, Tuukkanen A, Mertens HDT, et al. ATSAS 2.8: a comprehensive data analysis suite for small-angle scattering from macromolecular solutions. Jounal of Applied Crystallography. 2017;50(4):1212-25.

153. Kluenker M, Mondeshki M, Tahir NM, Tremel W. Monitoring Thiol−Ligand Exchange on Au Nanoparticle Surfaces Langmuir. 2018;34:1700-10.

154. Waugh DS. Making the most of affinity tags. Trends in Biotechnology. 2005;23(6):316320.

155. Kang JH, Ko YK. Lipid-coated gold nanocomposites for enhanced cancer therapy. International journal of nanomedicine. 2015;10:33-45.

156. Zuber A, Purdey M, Schartner E, Forbes C, van der Hoek B, Giles D, et al. Detection of gold nanoparticles with different sizes using absorption and fluorescence based method. Sensors and Actuators B: Chemical. 2016;227:117-27.

157. Gold Nanoparticles: Optical properties NanoComposix [updated 2018; cited 2018- 11-14]. Available from: https://nanocomposix.com/pages/gold-nanoparticles-optical-properties#local-refractive-index.

158. Kim Y, Kim K, Kang A. Lipid reconstitution-enabled formation of gold nanoparticle clusters for mimetic cellular membrane. Journal of nanomaterials. 2016;2016:7.

159. Woehrle GH, Brown LO, Hutchison JE. Thiol-Functionalized, 1.5-nm Gold Nanoparticles through Ligand Exchange Reactions: Scope and Mechanism of Ligand Exchange. JACS articles. 2004;127:2172-83.

160. Millipore M. Microsphere Coupling – Two-step EDC/Sulfo NHS Covalent Coupling Procedure for Estapor® Carboxyl-modified Dyed Microspheres: Merck Millipore; 2015 [2018-11-20]. Available from: AN1260EN00_MM.pdf from merckmillipore.com.

161. Thanh NTK, Green LAW. Functionalisation of nanoparticles for biomedical applications. Nano today. 2010;5:213-30.

162. Widdel F. Theory and Measurement of Bacterial Growth Universität Bremen2010 [2018-11-18]. Available from: https://www.mpi-bremen.de/Binaries/Binary307/Wachstumsversuch.pdf.

163. Gillespie C. How does sonication work? sciencing.com2018 [updated 2018-04-13. Available from: https://sciencing.com/sonication-work-5171302.html.

164. Bornhorst JA, Falke JJF. Purification of proteins using polyhistidine affinity tags. Methods in enzomology. 2010;326:245-54.

165. Introduction to size-exclusion chromatography Bio-Rad laboratories 2018 [cited 2018 11-04]. Available from: http://www.bio-rad.com/en-no/applications-technologies/introduction-size-exclusion-chromatography?ID=MWHAXJKG4.

166. Caprette DR. Introduction to SDS-PAGE Experimental biosciences1996 [updated 2012-11-18; cited 2018 11-04]. Available from: https://www.ruf.rice.edu/~bioslabs/studies/sds-page/gellab2.html.

167. Phase transition temperatures for glycerophospholipids Avanti Polar Lipids [updated 2018; cited 2018- 11-17]. Available from: https://avantilipids.com/tech-support/physical-properties/phase-transition-temps/.

168. Nagle JF, Tristram-Nagle S. Structure of lipid bilayers. Biochimica et Biophysica Acta (BBA) - Reviews on Biomembranes. 2000;1469(3):159-95.

169. Kučerka N, Nieh M, Katsaras J. Fluid phase lipid areas and bilayer thicknesses of commonly used phosphatidylcholines as a function of temperature. Biochimica et Biophysica Acta (BBA) - Biomembranes. 2011;1081(11):2761-71.

170. Hu Y, Doudevski I, Wood D, Moscarello M, Husted C, Genain C, et al. Synergistic interactions of lipids and myelin basic protein. Proceedings of the National Academy of Sciences of the United States of America. 2004;101(37):13466-71.

171. Winey M, Meehl JB, O'Toole ET, Giddings THJ. Conventional transmission electron microscopy. Molecular biology of the cell. 2014;25:319-23.

172. Bradbury S, Ford BJ, Joy DC. Transmission electron microscope. Transmission electron microscope. Encyclopædia britannica2018.

173. Transmission electron microscopy (TEM) Warwick2010 [updated 2010-01-04; cited 2018-11-04]. Available from: https://warwick.ac.uk/fac/sci/physics/current/postgraduate/regs/mpagswarwick/ex5/techniques/structural/tem/.

174. Cabra V, Samsó M. Do's and dont's of Cryo-electron microscopy: A primer on sample preparation and high quality data collection for macromolecular 3D reconstruction. Journal of Visualized experiments. 2015(95).

175. Bozzola JJ, Russell LD. Electron microscopy principles and techniques for biologists, 2nd edition: Jones and Bartlett publishers; 1999.

176. Just W. A practical guide to small angle X-ray scattering (SAXS) of flexible and intrinsically disordered proteins. FEBS Letters. 2015;589(19):2570-7.

177. Croce G. The Small Angle X-ray Scattering Technique:
An Overview Università del Piemonte Orientale [2018-11-18]. Available from: http://people.unipmn.it/gcroce/download/theory.pdf.

178. chemistry UDo. An introduction to circular dichroism spectroscopy UCI Department of chemistry [2018-11-18]. Available from: https://www.chem.uci.edu/~dmitryf/manuals/Fundamentals/CD%20spectroscopy.pdf.

8 Appendix

8.1 Expression and purification of P2 F57A

As stated in results paragraph 3.1.3 P2wt and P2 F57A the mutant type of P2 was not purified during this master project but in the course BMED325 Cellular biochemistry and nanobiochemistry and Arne Raasakka purified the protein used in this project.

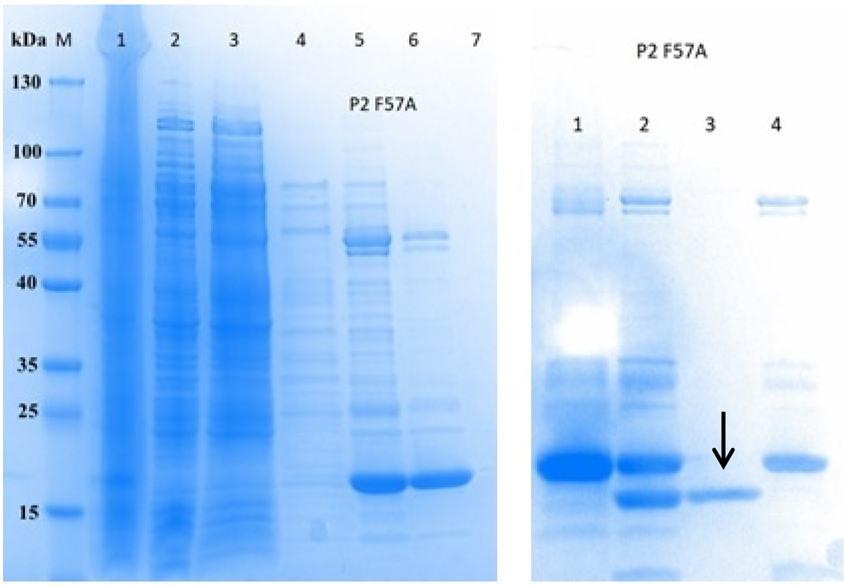

Figure 41: SDS-PAGE analysis of P2 F57A Ni-NTA affinity chromatogram. 1st (right) and 2nd (left) Ni-NTA affinity chromatographs are shown. Sample legend: 1st Ni-NTA: M; Marker, 1; Soluble fraction, 2; Unbound fraction, 3-4; Wash fractions, 5-7; elution fractions. 2nd Ni-NTA: 1; elution fraction from 1st Ni-NTA with TEV protease, 2; TEV protease treated elution fraction (overnight dialysis), 3; pooled unbound and wash fraction and 4; elution fraction. The known molecular weight (kDa) of the marker is specified in the figure. (Pictures reprinted and modified with approval from Arne Raasakka).

Purification of P2 F57A have the same steps as for P2wt and Figure 41(right image indicated with an arrow) shows that after overnight TEV protease digestion the protein got cleaved of from the His_6-tag and left a quite pure protein in the collected unbound and washing fractions. These fractions were pooled and concentrated before running size exclusion chromatography (SEC) using a HiLoad 16/60 Superdex 75 gel filtration column coupled to an Äkta Purifier system with a 2 mL loop. 1 mL fractions were collected around 68-82 mL where the peak is expected with a buffer containing 20 mM HEPES (pH 7.5) and 150 mM NaCl.

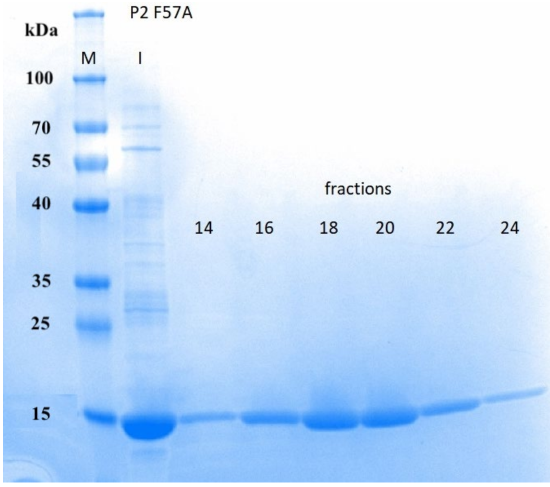

Figure 42: SDS-PAGE analysis from size exclusion chromatography of mutant P2 F57A. 1 mL fractions were collected at approximately 68-82 mL and samples were analysed on SDS-PAGE to check the purity before concentration were calculated using NanoDrop 2000 spectrophotometer and know extinction coefficients found using ProtPara. Sample legend: M; Marker, I; concentrated protein (before SEC), 14-24; fractions collected at expected peak in SEC. The known molecular weight (kDa) of the marker is specified in the figure. (Pictures reprinted and modified with approval from Arne Raasakka).

The purity of the protein was good as viewed in Figure 42. The bands correlates with the know molecular weight of P2 F57A which is 14.9 kDa. Fractions were pooled and concentrated (Amicon 3k MWCO centrifugal filter) to reach a high yield of protein (3.29 mg/mL). Concentration of the protein were calculated using know extinction coefficients (ProtParam) and NanoDrop 2000 spectrophotometer. Yield and concentration are listed in Table 1.

Table 10: Extinction coefficients and yield for P2 F57A. P2 F57A was expressed in *E. coli* (Rosetta(DE3)) and purified using Ni-NTA affinity chromatography and size exclusion chromatography (SEC). Concentration and yield of the protein was calculated using NanoDrop 2000 spectrophotometer and extinction coefficients found on ProtParam. The yields of the P2 F57A are shown together with known extinction coefficients and molecular weight.

	mg/mL	**Concentration (µM)**	**Abs 0.1% (A.U)**	**ε ($M^{-1}cm^{-1}$)**	**Molecular weight (MW) (Da)**
P2 F57A	3.29	221	0.939	13980	14890.34

8.2 SEM images of iron(II,III)oxide and silicon dioxide nanospheres from collaborator

Chaozhan Wang (Ph.D. Professor of Chemistry) provided scanning emission electron (SEM) images of the nanoparticles before they were sent to us. Below are the images from the different nanoparticles listed in Table 1 in Methods and materials 2.4.2 Iron(II,III)oxide and silicon dioxide. Fe3O4@SiO2-ODS-DMPA and Fe3O4@SiO2-ODS-DPPC with 10 nm size cannot be viewed clearly with SEM as the particle size is too small and the transmission scanning electron facility at College of Chemistry and Materials Science, Northwest University, is not allowed to be used for magnetic samples, so no further images were taken of these particles.

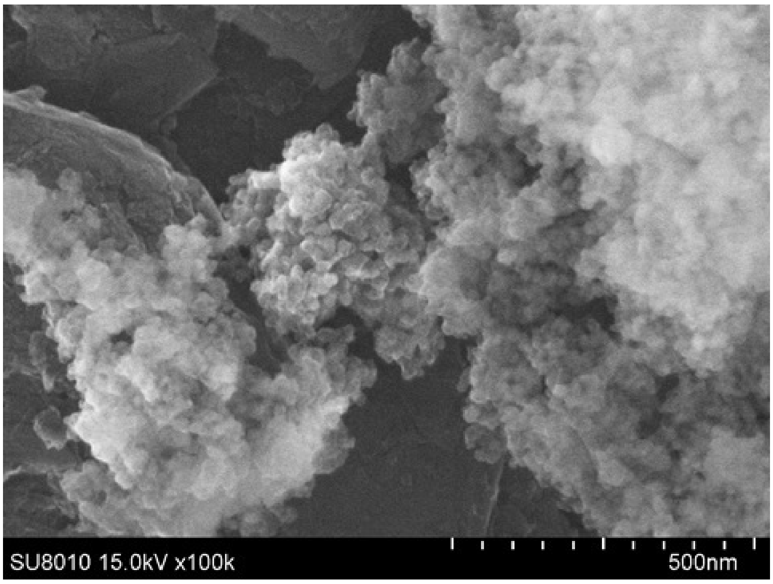

Figure 43: Scanning electron micrograph of Fe_3O_4@ODS-DMPA nanoparticles with size 10 nm. The nanoparticles cannot be clearly viewed as the size is too small for good SEM images. Figure reprinted from Chaozhan Wang (Ph.D. Professor of Chemistry, College of Chemistry and Materials Science, Northwest University, Xi'an, China.

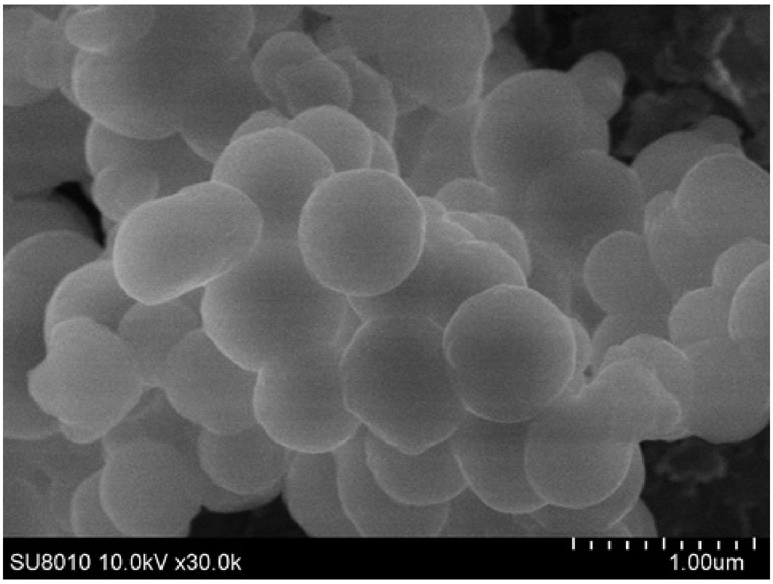

Figure 44: Scanning electron micrograph of Fe_3O_4@ODS-DMPA nanoparticles with size 150 nm. Figure reprinted from Chaozhan Wang (Ph.D. Professor of Chemistry, College of Chemistry and Materials Science, Northwest University, Xi'an, China.

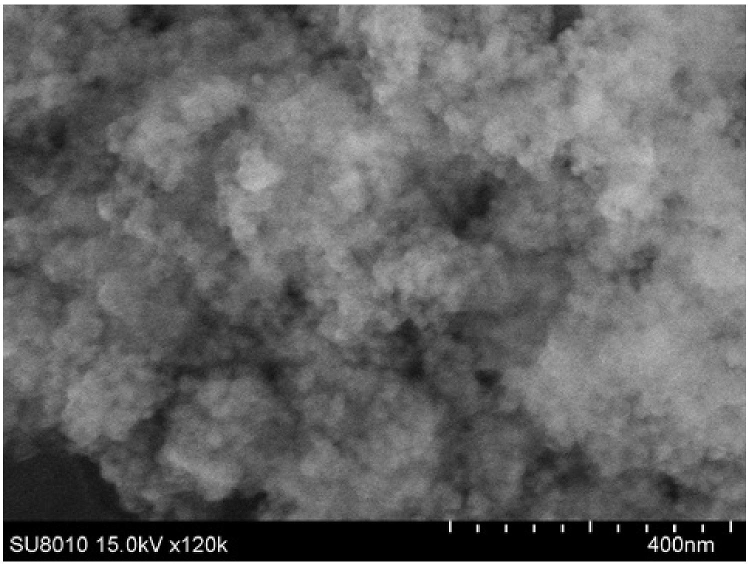

Figure 45: Scanning electron micrograph of Fe_3O_4@ODS-DPPC nanoparticles with size 10 nm. The nanoparticles cannot be clearly viewed as the size is too small for good SEM images. Figure reprinted from Chaozhan Wang (Ph.D. Professor of Chemistry, College of Chemistry and Materials Science, Northwest University, Xi'an, China.

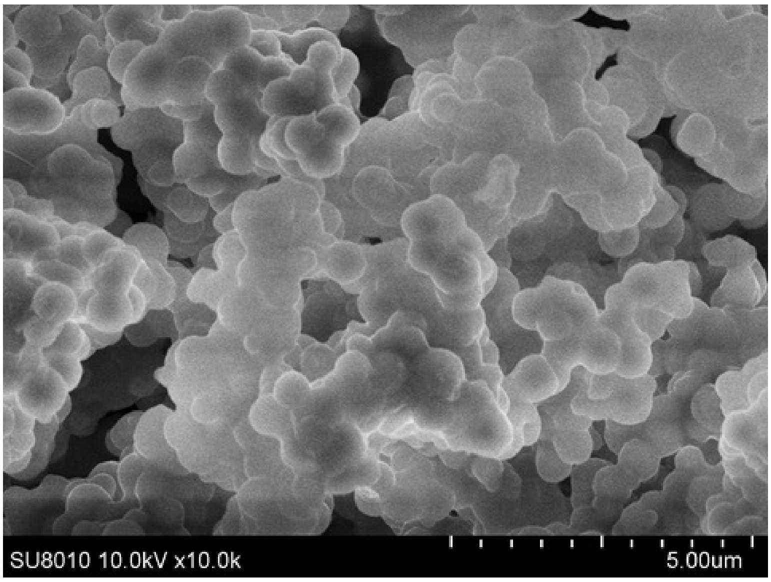

Figure 46: Scanning electron micrograph of Fe_3O_4@ODS-DPPC nanoparticles with size 150 nm. Figure reprinted from Chaozhan Wang (Ph.D. Professor of Chemistry, College of Chemistry and Materials Science, Northwest University, Xi'an, China.

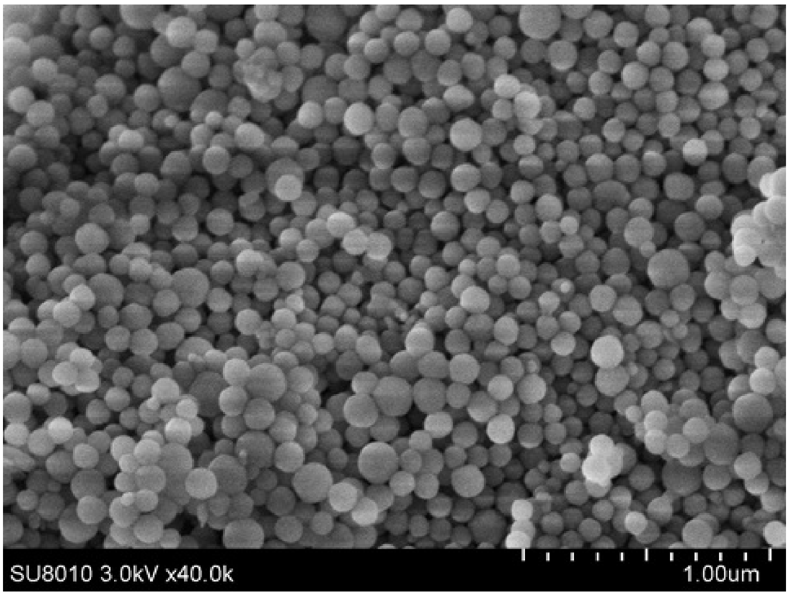

Figure 47: Scanning electron micrograph of SiO_2@ODS-DMPA nanoparticles. Figure reprinted from Chaozhan Wang (Ph.D. Professor of Chemistry, College of Chemistry and Materials Science, Northwest University, Xi'an, China.

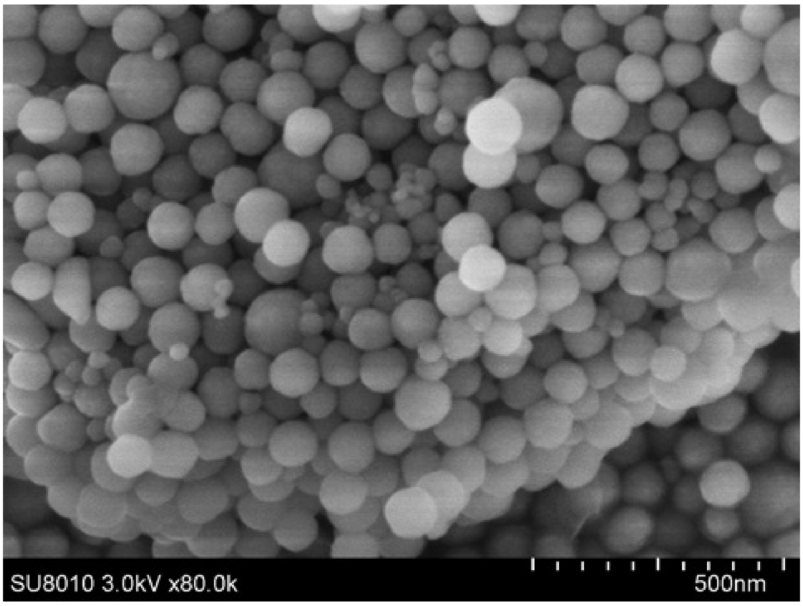

Figure 48: Scanning electron micrograph of SiO_2@ODS-DPPC nanoparticles. Figure reprinted from Chaozhan Wang (Ph.D. Professor of Chemistry, College of Chemistry and Materials Science, Northwest University, Xi'an, China.

8.3 UV-VIS spectra of 80 nm gold nanoparticles normalized to 300 nm

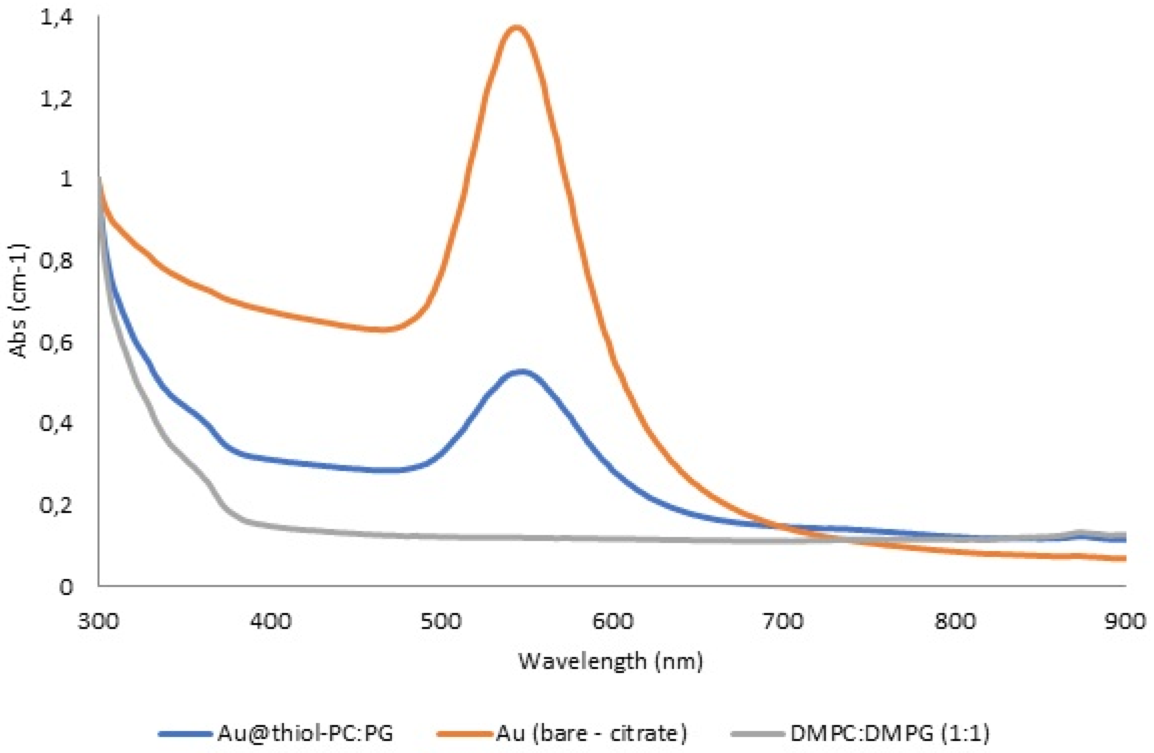

Figure 49 UV-VIS spectra of bare AuNPs and coated AuNP (Au@thiol-PC:PG) normalized to 300 nm. To check a possible coating of the coated AuNPs the UV-VIS spectra was measured with a wavelength ranging from 300 nm to 900 nm, with step size = 2 and number of flashes was 25. DMPC:DMPG (1:1) was used as a control. The AuNPs are coated with 1-octanethiol and DMPC:DMPG (1:1) The data is normalized to 300 nm. A bump at 360 nm can be seen in the spectra. The coated gold nanoparticles have lower absorbance, red shift of 4 nm and elevated base line indicated increased size and aggregates in the solution.

8.4 Vesicle aggregation 660 nm

Vesicle aggregation between myelin proteins (MBP, P2wt and P0ct) with varying ratios of bicelles and liposomes were measured at both 450 nm and 660 nm. The results for the 450 nm wavelength are shown in Results 3.5. The data from measuring at 660 nm is shown here. In short: vesicle aggregation were tested with constant concentration of protein (0.5 mg/mL) mixed with different ratios of DMPC:DMPG, bicelles and liposomes, 9:1, 4:1, 1:1 and 1:0 respectively, where 1:0 ratios were used at a negative control. The assay was done over 30 min with a temperature being 30 ºC.

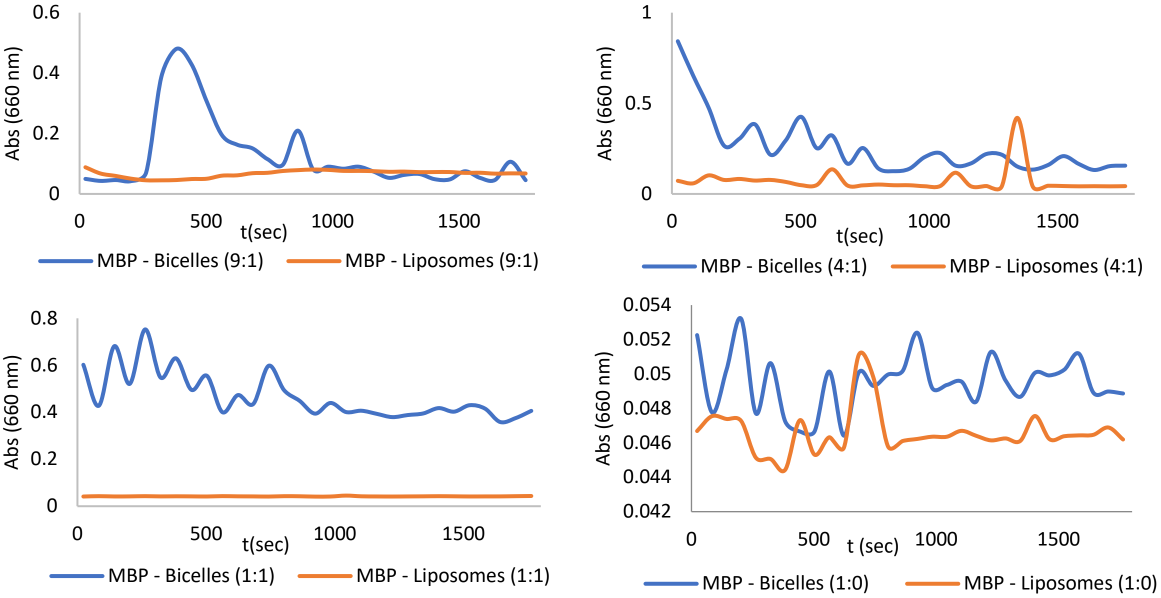

Figure 50: Vesicle aggregation with different ratios of DMPC:DMPG with MBP. Measured absorbance over 30 minutes with constant concentration of P2wt and different ratios of DMPC:DMPG in liposomes and bicelles. A) 9:1 ratio, B) 4:1 ratio, C) 1:1 ratio and D) 1:0 ratio as negative control. Absorbance measured at wavelength 660 nm at 30ºC.

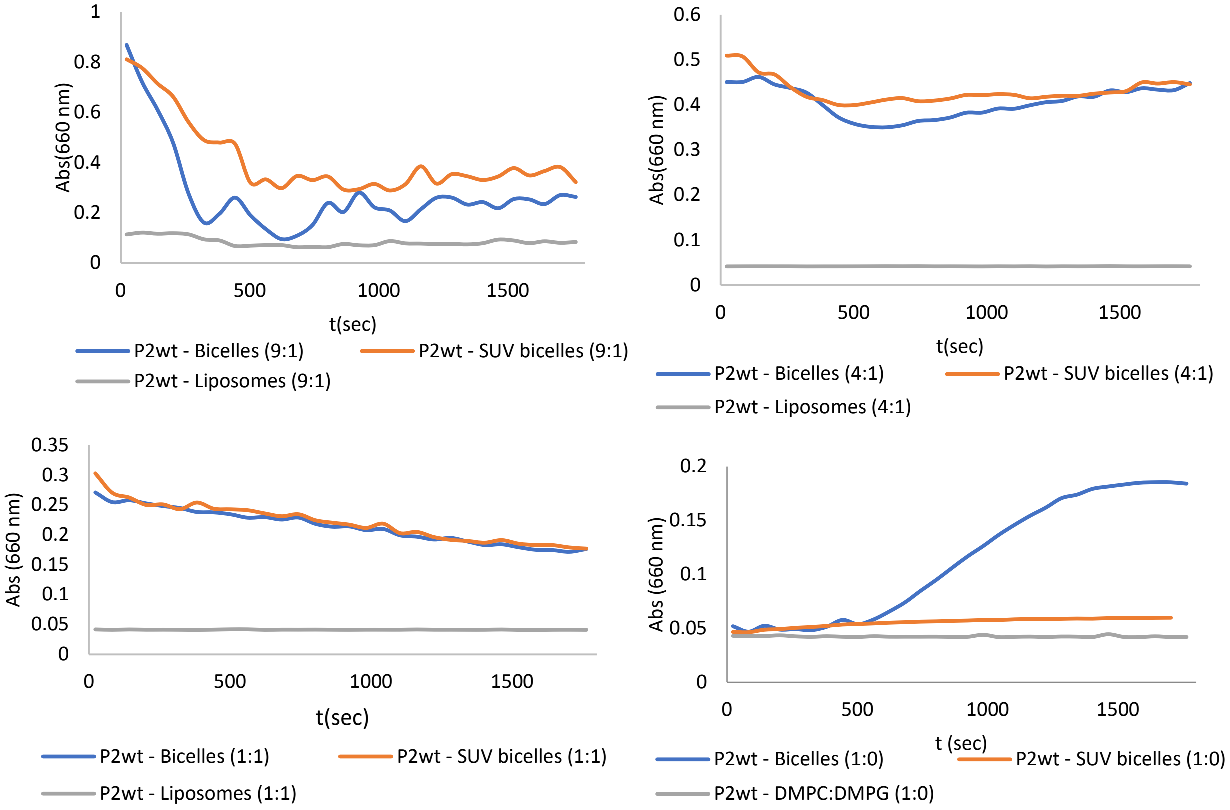

Figure 51: Vesicle aggregation with different ratios of DMPC:DMPG with P2wt. Measurement of absorbance over 30 min with constant concentration of P2wt with bicelles, SUV bicelles and liposomes with different ratios of DMPC:DMPG. A) 9:1 ratio, B) 4:1 ratio, C) 1:1 ratio and D) 1:0 ratio as negative control. Absorbance measured at wavelength 660 nm at 30ºC.

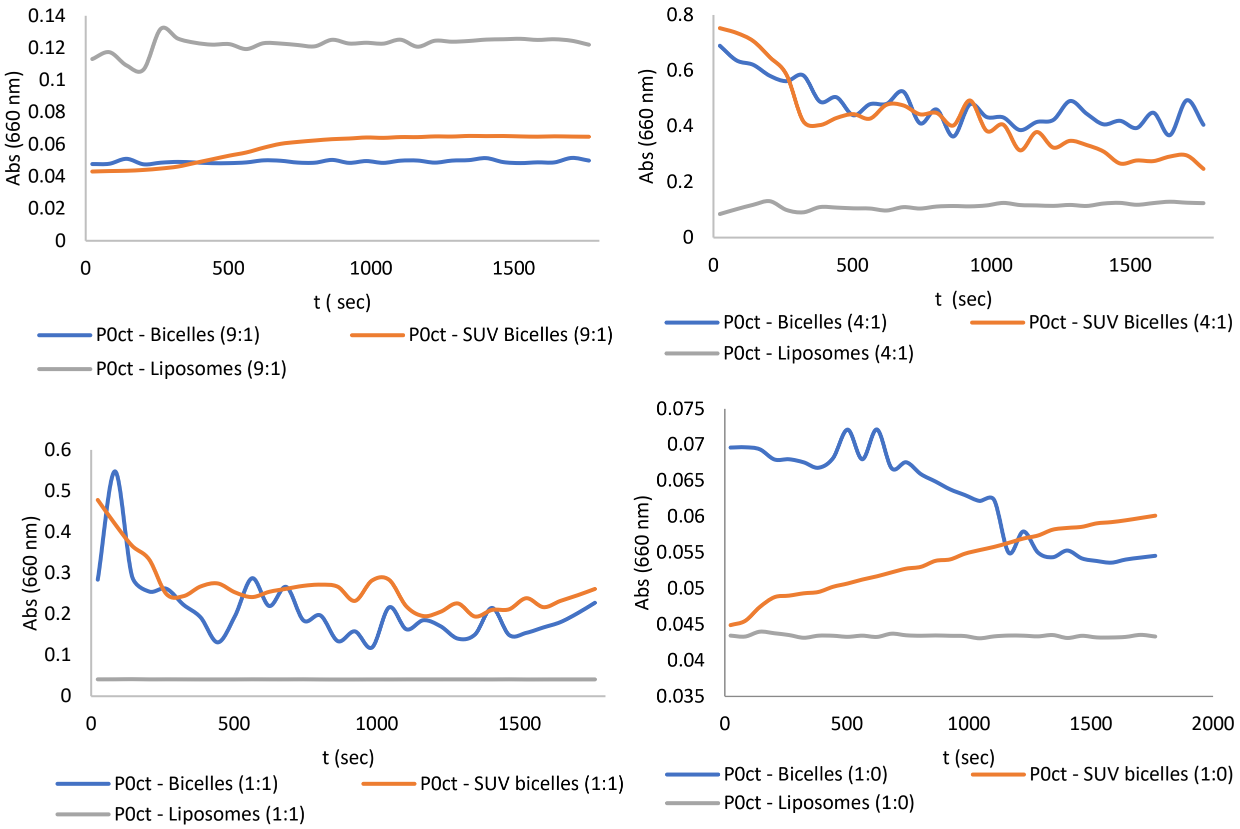

Figure 52: Vesicle aggregation with different ratios of DMPC:DMPG with P0ct. Absorbance measured over 30 minutes with constant concentration of P0ct (0.5 mg/mL) with different ratios of DMPC:DMPG in bicelles, SUV bicelles and liposomes. A) 9:1 ratio, B) 4:1 ratio, C) 1:1 ratio and D) 1:0 ratio as negative control. Absorbance measured at wavelength 660 nm at 30 ºC.

8.5 Cryo-EM images of P2wt in bilayers

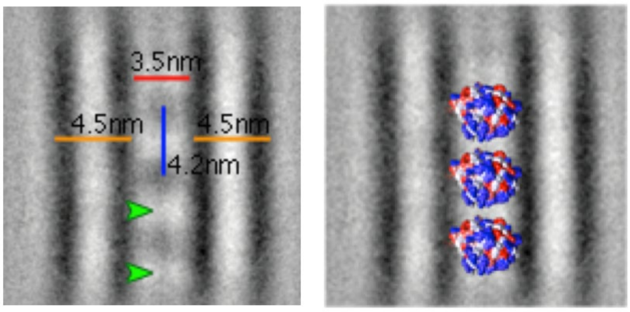

Figure 53: Cryo-EM images of P2wt bound to lipid bilayers. Cryo-EM images of P2wt bound to lipid bilayers with selected repeat distances viewed. Reprinted from unpublished data from Salla Ruskamo

8.6 SAXD measurements

All samples with 2 µM P2 F57A mixed with 1-3 mM liposome induced two Bragg peaks, as seen in Figure 55. For the samples with 1 mM and 2 mM the peaks corresponds to mean repeat distances of 8.7 nm and 4.4 nm. The 3 mM samples (1:1500 P/L ratio) had peaks corresponding to repeat distances of 7.1 nm and 4.4, respectively.

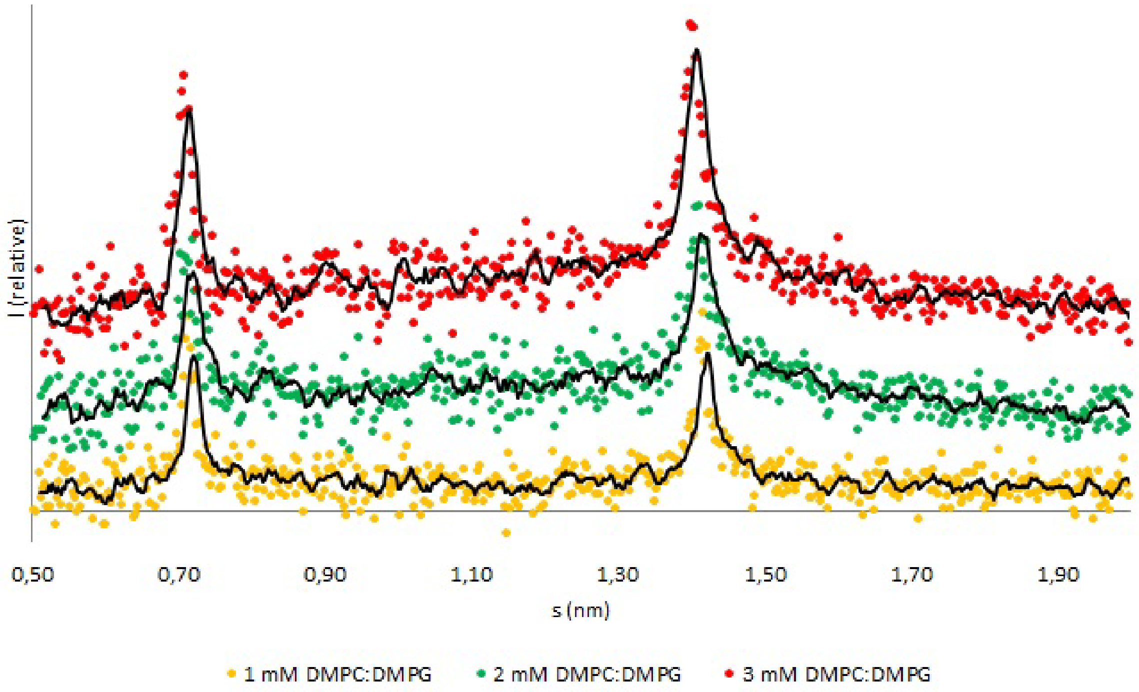

Figure 54: X-ray diffraction spectra of 2 µM P2 F57A with liposomes. Mixing P2 F57A with 1-3 mM gave several major Bragg peaks in the X-ray diffraction patterns. 2 µM concentrations of the mutant are viewed as filled markers with DMPC:DMPG ratio of the bicelles being 1:1. A moving average, black line, has been plotted over each dataset. For clarity all dataset is offset and is not scaled to each other. The synchrotron SAXD data were collected at PETRA III storage ring, DESY, Hamburg, Germany on beamline P12.

8.7 Basic theory behind the different techniques

8.7.1 Protein purification

8.7.1.1 Optical density

When a bacteria cell culture grows, it grows by cells dividing into to daughter cells. When this happens over time, the growth medium goes from being clear to very turbid as a result of increasing cell concentration. Bacterial growths have different phases; lag phase, log phase, stationary phase and a death phase. The lag phase is where the cells adapt to the medium, matures and don't divide. Log phase is characterized by cell doubling. Bacteria divide into two daughter cells, and doubling of existing population will continue until the media runs out of nutrients. When the waste is the media is increasing with decreasing nutrients, cell both divide and die at the same rate. It is called the stationary phase and it is a small period before death phase. The last phase is characterized by bacteria death, no cell division happens. When bacterial cells are cultured, optical density is measured to get information about when the cell culture is in the log phase, they only divide and there is no cell death. By using optical density one can monitor the growth phases and stop bacterial expression before death phase (162)

8.7.1.2 Ni-NTA

When purifying proteins mentioned in this thesis, Ni-NTA affinity chromatography is used to separate wanted protein from all the other proteins in the lysate. It is done so by peptide affinity tags, which is this case is a hexahistidine tag (His_6-tag). In the expression vector the polyhistine tag is added onto the target gene, the gene coding for the protein. After expression of the protein is done, the cell culture gets lysed. The cell membran is broken down by high sound waves with frequencies of 20 kHz or higher, called sonication (163). The lysate contain all of the insides of the cells with the wanted protein being among them. Ni-NTA affinity chromatography is out of several chromatographs collectively called immobilized metal-affinity chromatography (IMAC) that is based on the interaction between a metal ion (Co^{2+}, Ni^{2+}, Cu^{2+}, Zn^{2+}) immobilized on a matrix and a specific amino acid side chain. The Ni-NTA is coupled to a solid resin which coordinates Ni^{2+} through for coordination sites and leaves two sites exposed which can bind to the His_6-tags (164). When the lysate runs through the matrix the hexahistidine tags binds to the free coordination site on the nickel ion while most of the untagged proteins runs through, some might bind weakly. The lysate fraction is re-added several times to get as much of the wanted protein to bind to the metal ions. The target protein is then retrieved by an elutant, often imidazole which also binds to the Ni^{2+} and therefore competes with the hexahistidine tags. When added as a elutant, a high concentration of imidazole will bind to the metal ions and the His_6-tagged protein will run through the matrix (16). Ni-NTA affinity chromatography gives easily a high yield of pure protein.

8.7.1.3 Size-exclusion chromatography

Even though Ni-NTA achieves a relative pure protein, some other proteins from the lysate might still be in the protein solution. To get the protein as pure as possible size-exclusion chromatography (SEC) is the last step in the purification process of the proteins mentioned in this thesis. As the name states, this method separates molecules based on their size – or hydrodynamic volume, to be excat. The SEC column contains spherical beads that have pores of a specific size distribution, depending on the protein of interest (165). When the protein solution collected from Ni-NTA affinity chromatography is added to the column, molecules larger than the pores in the beads will pass through the column faster than smaller molecules which will diffuse into the pores, thus, using longer time flowing through the column. Molecules are separated based on their molecular weight (MW), their size, with larger molecules eluting first. SEC is a good tool if one wants to separate contaminants from your protein or separate soluble aggregates from your protein. It can also be used to analyse and increase the monodispersity of your protein or do a buffer exchange if you want to remove for example NaCl from your protein buffer.

8.7.1.4 SDS-PAGE

SDS-PAGE is an analytical method that, like SEC, separates proteins on their molecular size by applying an electrical field where the molecules travels towards an electrode with opposite charge. The gel matrix consists of a meshwork of polyacrylamide where smaller proteins travel faster due to less resistance from the gel matrix. Proteins may have different charge and to get every sample to travel towards the same electrode, SDS is used. SDS has a negative charge and binds to, denatures and solubilizes all proteins. A reducing agent is used to cleave disulphide bonds in the protein that are important for proper folding. With added SDS, increasing the temperature to 95 °C, proteins denature to linear chains with a net negative charge, because SDS has high affinity to hydrophobic patches of unfolded proteins (166). When running them with gel electrophoresis, all proteins will travel towards the anode with different speed depending on size. A molecular marker with known molecular weight is added as a reference. After the gel electrophoresis is done, the gel is stained so the separated protein bands becomes visible. A usual setup for running SDS-PAGE is shown in Figure 55.

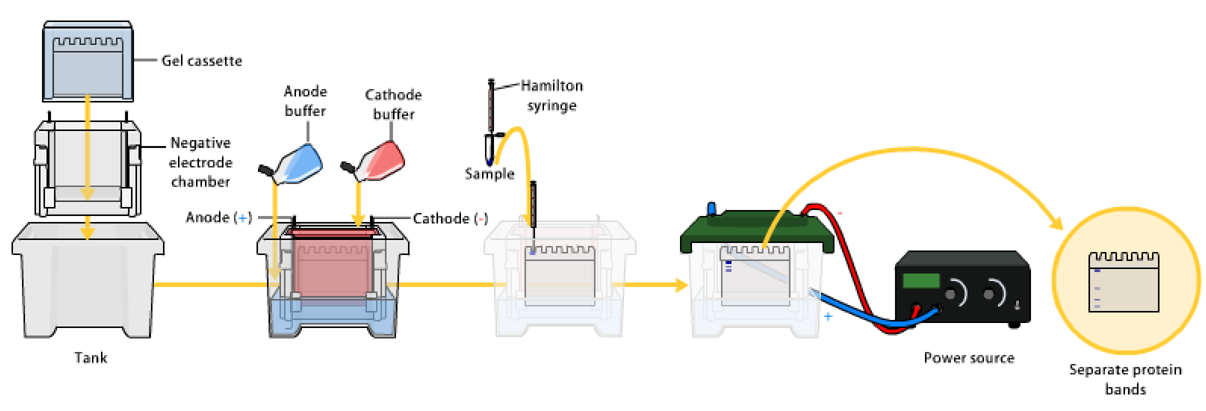

Figure 55: Illustration of a setup for doing SDS-PAGE. The polyacrylamide gel is placed in a holder inside the electrophoresis chamber before the desired buffered is poured into the chamber. By the use of a Hamilton syringe or a pipette the samples can be loaded into the wells of the gel. A voltage is applied over a certain amount of time to separate the proteins in the gel. After staining the gel with staining one can visualize the protein bands. Reprinted from Bensaccount at English Wikipedia [CC BY 3.0 (https://creativecommons.org/licenses/by/3.0)], from Wikimedia Commons]

SDS-PAGE is an easy analytical tool to use when checking protein purity or protein-binding (co-sedimentation assays).

8.7.2 Selection of lipids

As explained in the introduction, both mixtures of DMPC:DMPG and DOPC:DOPS makes the liposomes and bicelles having a net negatively charged surface, which are consistent with charges occurring in the native myelin sheath (18). The choice of using these lipids is based on several reasons. First of all, the lipid composition in myelin is broad. Several different lipids contribute to its stability: cholesterol, galactosylceramide, ethanolamine-containing plasmalogens, lechtins, sphingolipids and many others (23, 24). To use so many different lipids in a model system would be very challenging so simple lipid composition makes it easier to make and the lipid chosen are highly stable and can be used in several different analytical methods. Second, the phase transition temperature of the lipids plays a crucial part. DOPC and DOPS have phase transition temperatures, when they shift from solid phase to gel phase, below zero (-17°C and -11°C), which means that they will always be in a liquid disordered phase during our experiments. DMPC and DMPC have phase transition temperatures (Tm) of 24°C and 23°C (167), so when analytical methods are used from 25°C to 30°C, they will also be in a disordered phase. The Tm for DMPC and DMPC are quite low for saturated tails. DM's have a carbon chain length of 14 while DO's have length of 18 you would imagine that the bilayers they make would have different thickness. But since both DOPC and DOPS have a double bond between to carbons in the tail, they are unsaturated in cis conformation, making the bilayers thinner than expected. Thus, the thickness of DM and DO bilayers is actually very similar, around 3.7 nm (168, 169). When comparing lipid compositions like DMPC:DMPG and DOPS:DOPC, they both have to be in the same phase. It is effective to run methods above 25°C, which makes them both be in liquid disordered phase, without affecting protein stability or structure or the physical behaviour of the lipids due to phase-differences.

The reason we do not use lipids like DPPC or DSPC is because both DP and DS lipids have higher Tm (above 50°C) and the bilayers would be much thicker (167). The experiments would have had to be done at very high temperatures, which are over physiological temperature and would have affected protein stability.

The use of DOPS instead of DOPG is because the predominant negatively charge component in eukaryotic membranes (also in myelin) is PS, so it more comparable to native myelin than DOPG (170). DMPS would in theory been a better choice than DMPG, but DMPS have a Tm at 35°C and it is expensive compared to DMPG.

8.7.3 UV-vis spectroscopy

UV-vis spectroscopy measures the light that passes through a sample, which can be measured using a single wavelength or over a range of wavelengths, and uses transition of electrons in the sample to get an absorption spectra. When a molecule absorbs ultraviolet or visible light the electrons in the molecule gets excited from a low level to a high level of energy. The energy level that is nearest the positively charge core have the lowest amount of energy and electrons deposited farther away from the core have higher energy. The molecule will absorbed some of that light and the electron gets excited to a higher energy level. The absorption gets recorded by measuring the difference in light transmission, resulting in an absorption spectra (125).

8.7.4 Transmission electron microscopy

TEM is a microscope that uses an electron beam to form an image. Because electrons have a wavelength that is much smaller than that light, the resolution is much higher than from light microscope. When the electron beam hits the sample the electrons get absorbed and the scattered producing an image (171). TEM consist of three main parts: first, an electron gun and a condenser system. The gun produces the electron beam and the beam is focused onto the sample by the condenser system. The second part is a system that produces an image containing an objective lens, movable sample stage and lenses. Third, the image-recording system makes an image that can be viewed and analysed (172). The image that is produced is monochromatic, composed of one color, where the darker areas if the image means that fewer electrons are transmitted through and lighter areas denotes more transmittance of electrons (173).

Before imaging, the samples have to be loaded onto grids that fit in the sample holder. Carbon-coated copper grids are usually used. The grids are made out of copper and a thin layer of carbon is coated onto the grid. The film is very thin, transparent to electron and do not interfere with the sample while at the same time stabilizes and has good conductivity. The grids are also often glow-discharged right before sample preparation. The carbon-coating layer is naturally hydrophobic (repelled from water) which many biological samples contain, and with glow-discharging the grids the carbon coating turns hydrophilic which help samples distribute evenly over the grid (174). After samples have incubated for 1 minute on the grid, they get negatively stained. Negative staining stains the background and not really the sample itself, making the sample more visible. Commonly used negative stains heavy atom salts such as uranium, molybdenum and tungsten. Uranyl acetate was used in this thesis (175). Negatively staining a sample is relatively easy using drop method: after the sample has incubated for some time a drop of stain is placed onto it and left for incubating for 12 sec before a new drop is added. Excess liquid is removed either by air-drying or by a filter paper.

8.7.5 Turbidity

Turbidity assays measure the optical properties of a sample and is used in this project to study vesicle aggregation. Depending of what the samples is one can apply many different setting as temperature, kinetice cycles, shaking and wavelength or a range of wavelength. Light is directed onto the sample and the light that passes through the sample gets measured. When proteins induce aggregates the samples gets turbid (cloudy) and causes the light to get scattered. If the aggregates precipitate more light will hit the detector. In the case of vesicle aggregation one can study differences in absorbance due to concentrations or different ratios in the sample over time.

8.7.6 Small-angle X-ray diffraction

Small-angle x-ray diffraction is based on the same principles as for small-angle X-ray scattering and is used to obtain structural information about a sample. It can provide information size, shape and internal structure of systems. A Monochromatic X-rays beam hits a sample and a detector registers diffraction angles, where the scattering signal is derived from the difference between the average electron density of the buffer and the sample. The scattering/diffraction pattern of the sample is isotropic; it has the same value in all directions because the particles in your sample have random orientations (176). The scattering of X-rays is recorded at very low angles (0.1 - 10°) and at this angular range one can get information about distances in ordered materials. For example in the case of lipid aggregations they can cause ordered structures that will give constructive interference similar to lattice structures in solid crystals, giving Bragg peaks (177). From these peaks one can calculate repeat distances residing in the aggregates by using momentum transfer, s, where s is:

$$s = \frac{4\pi\sin(\theta)}{\lambda}$$

S can be found by finding looking closely at each peak and then repeat distance (d) can be calculated by using this equation.

$$d = \frac{2\pi}{s}$$

8.7.7 Synchrotron radiation circular dichroism spectroscopy

SRCD is circular dichroism (CD) with the use of synchrotron radiation as light source. CD uses left-handed and right-handed polarized light and measures the difference in absorbance between them when a molecule absorbs them. CD can be measured if the polarized light interacts with chiral molecules (mirror-image isomers). The majority of biological molecules are chiral and one can use this property to study secondary structures like α-helices, β-sheets and unfolded state, or to study changes in structure (178). The different regular secondary structures have distinct CD spectra, and one can easily see what the main secondary structure content the protein has.